Towards an Improved Microwave Tomography System

by
Colin Gilmore

Ph.D. Thesis
Submitted in Partial Fulfillment
of the Requirements for the Degree of
Doctor of Philosophy in Electrical Engineering

Department of Electrical and Computer Engineering
University of Manitoba
Winnipeg, Manitoba, Canada

ABSTRACT

This dissertation outlines work taken towards the understanding, implementation, and improvements to the process of creating of quantitative images of the bulk-electrical parameters of the interior of unknown objects via the use of electromagnetic scattering data. Improvements are considered to both theory and experiments using low-power radiation in the microwave frequency range, known as Microwave Tomography (MWT).

A detailed derivation of the Multiplicative-Regularized Contrast-Source Inversion (MR-CSI) method is given, and we compare the performance of MR-CSI with the other leading inversion technique used in MWT: the Gauss Newton/Distorted Born Iterative Method. The inversion results of the two algorithms are very similar, and thus most of the differences between them are in the relative ease of implementation and computational resource use.

We further introduce a new version of the CSI algorithm, based on the Finite-Difference method. Using this algorithm, we show that when accurate information about a scatterer is known before the inversion process, this information is best utilized as an artificial computational background, as opposed to an initial guess of the scatterer.

The MWT problem is also formulated inside of a conductive enclosure, which significantly changes the physics, and resultant Green's function, of the MWT problem. The implications and possible advantages of this type of MWT are discussed, and synthetic inversion results for a circular enclosed system are presented. These results show that the enclosure is capable of improving the inversion in some regions, although more research is required to realize the full potential of conductive-enclosure MWT.

In the final section, experimental results from both open-region and conductor-enclosed type MWT systems developed at the University of Manitoba are shown. For the open-region system, we show that antenna coupling is a major factor affecting the data collection, and provide a simple method for avoiding the frequencies where this coupling is too strong to prevent effective imaging. For the conductor-enclosed type system, we have found the system to be extremely sensitive to presence of antennas in the chamber, and show that effective MWT imaging is possible in this type of system by taking the antenna elements into account in the inverse solver.

CONTRIBUTIONS

This dissertation outlines several noteworthy contributions to the art of Microwave Tomography. Many of these contributions were accomplished with significant help from other colleagues, noted herein. These contributions include:

- Achieving an understanding of, and clarifying, the non-linear inverse problem and completing a comparison of state-of-the-art inversion techniques (completed with Puyan Mojabi).
- Implementing a novel differential-based inverse solver and showing that a-priori information is better utilized as a background to the scattering problem.
- Formulation of the Microwave Tomography problem for conducting enclosures, performing initial synthetic inversions for such systems, and elucidating the possible advantages of these systems compared to open-region systems.
- The design, construction and testing of a wide-band experimental open-region Microwave Tomography system, and the development of a novel frequency selection algorithm for this system (completed with Puyan Mojabi, Cam Kaye, Amer Zakaria, and Majid Ostadrahimi).
- The design, construction and preliminary testing of an enclosed-region Microwave Tomography prototype (completed with Amer Zakaria, Cam Kaye, and Puyan Mojabi).

ACKNOWLEDGMENTS

First and foremost, I thank Dr. Joe LoVetri for his support, direction, and encouragement of my education and research efforts for nearly a decade. Without his example and advice, I never would have entered graduate school.

I also recognize the direction and support given by my co-advisor, Dr. Vladimir Okhmatovski.

I would like to acknowledge the many colleagues without whom this research would not have been possible. More than is usually recognized, academic research is a group effort. Ian Jeffrey, Puyan Mojabi, Amer Zakaria, Cameron Kaye, and Majid Ostadrahimi have all significantly enriched my education.

For the great opportunity and continued enlightening discussions, I would also like to thank my supervisor and colleagues at Schlumberger-Doll Research: Aria Abubakar, Maokun Li and Wenyi Hu.

For their work in guiding my research throughout my PhD, I also recognize the efforts of my committee: Dr. Thomas Berry and Dr. Sima Noghanian.

Finally, I would like to thank the various agencies and individuals that have provided me (and many other researchers) with the funding necessary to live the academic life. Specifically, the National Sciences and Engineering Research Council of Canada, Western Economic Diversification Canada, Mathematics of Information Technology and Complex Systems Canada, Stephen Pistorius at CancerCare Manitoba, and the Manitoba Health Research Council have all contributed to this research. Without this support, this research would have simply not been possible.

TABLE OF CONTENTS

LIST OF TABLES

LIST OF FIGURES

1. INTRODUCTION

The road to wisdom?
Well, it's plain and simple to express:
Err and err and err again
but less and less and less.

Piet Hein

This dissertation presents research into the use of radiated electromagnetic waves to create images of objects which are obscured or hidden from normal human perception. Frequencies utilized for this problem range from 1 Hz [1] all the way to optical frequencies (THz) [2], and the image pixel size may vary from hundreds's of meters to micro-meters. While we focus on its use in the microwave frequency range where these techniques are known as Microwave Tomography (MWT), the use of electromagnetic fields to probe the interior of objects is known by many different names: non-destructive testing, diffraction tomography, remote-sensing, and ground-penetrating radar, to name a few.

The use of electromagnetic fields for the purpose of quantitatively determining the inner structure of objects leads to inverse mathematical problems. In general, inverse problems arise when one is attempting to determine some quantity, e.g.,

source or material parameter, which is not directly observable, and can be contrasted with the forward (or direct) problem, where both sources of energy and material parameters are usually known. The forward and inverse problems obey the same fundamental differential equations, but the known and unknown quantities appearing in the equations are different. Typically, forward problem offers a unique solution which may be calculated in a stable way, while the solution of the an inverse problem is non-unique, and attempted solutions experience difficulties with stability (i.e., the solution of the problem does not depend continuously on the input).

As a simple example of how inverse and forward problems may differ, consider measuring the gravitational pull of an unknown object, and from this measurement attempting to determine its density and shape (volume). If the density and shape of this object are known, it is straight-forward to calculate its gravitational pull on another object (forward problem). However, if we only know the gravitational pull of the object on some gravity sensor, and desire to know the shape and density of the object (the inverse problem), it is immediately clear that a unique solution is impossible to find. Consider a homogeneous sphere of a particular volume and density, then consider another sphere with twice the volume, but with half of the density of the original. From some distance away, each sphere will exert the same gravitational pull, and thus a unique solution cannot be found from knowledge of the gravitational pull of the unknown object. Further, if we were to add some rapid variation to the outside shape of our sphere, which caused gravitational variations below the detectable level of

the gravity sensor used for the measurement, these variations would be undetectable. Thus, in the inverse problem, we could add as many of these small variations as desired to the 'solution' of the sphere's shape without altering the measurement. As every sensor has its practical detection limits, this issue leads to unstable solutions of inverse problems. We note that this example is not identical to that of electromagnetic waves used throughout this work, it does however provide an exmaple of how forward and inverse problems may differ.

1.1 Microwave Tomography

This thesis focuses on the use of electromagnetic (EM) waves in the microwave frequency range of a few hundred MHz to approximately 10 GHz. This type of electromagnetic wave-field imaging is known as *Microwave Tomography* (MWT). The etymology of the word 'tomography' implies imaging a 3D target through the use of many 2D 'cuts' or slices through the scatterer, and MWT is often used this way (e.g., [3–6]). However, the electromagnetic inversion community has extended this term to include full 3D quantitative imaging, e.g., [7], and we also utilize this nomenclature. Other terms used for MWT include 'microwave inversion', 'microwave imaging', or the more general 'electromagnetic inversion'. This work is focused on the *quantitative* imaging of penetrable objects, i.e., the generation of images which have a quantitative pixel intensity which relates to some physical parameter of interest. In this thesis, these physical parameters are the the electrical permittivity and effective conductivity

of the imaged object (which may be combined into the complex electrical permittivity). The long-term goal of this work is the use of microwave radiation to image biomedical tissues for medical purposes.

Biomedical microwave tomography provides a promising alternative or complementary biomedical diagnostic technique for conventional soft-tissue imaging modalities. Current or predicted advantages of microwave tomography include (1) its low cost and portability, especially relative to Magnetic Resonance Imaging (MRI); (2) its use of safe non-ionizing radiation (unlike x-ray tomography); (3) its ability to image bulk-electrical properties as a feature of tissue that is not imaged by most other modalities; and (4) its ability to quantitatively reconstruct frequency dependent permittivity and conductivity profiles of living tissue as a way of identifying physiological conditions of those tissues.

Perhaps the most studied application of biomedical MWT is its use for the detection and monitoring of breast cancer. Motivated by (i) the seriousness of the disease: it ranks as one of the top causes of death for women in the industrialized world [8], and (ii) by problems with comfort, specificity, and sensitivity of the current gold-standard of breast-mammography (mammography is uncomfortable for the patient, misses about 15% of all cancers present, and around 3/4 of regions which are biopsied based on mammography results turn out to be benign [9]), and (iii) early studies which showed significant differences in electrical permittivity and effective conductivity between normal and malignant breast tissues at microwave frequencies [10, 11], there has been

significant interest in the use of microwaves for breast cancer detection [3, 9, 12–22]. More recent studies of ex-vivo breast tissue have moderated the early enthusiasm for the technology [23, 24][1]. However, regardless of these measurements, at least one group [26, 27] has shown that MWT can successfully differentiate malignant breast tumors from other non-malignant tissues in-vivo (on a series of mammography-screened patients). There are also some initial reports of another group succesfully determining the presence of breast cancer in-vivo as well [28, 29].

Further applications for MWT might eventually be found in the frequent monitoring of tissues and disease when a 'watch and wait' approach is indicated. For example, there is recent evidence to suggest that up to 22% of breast cancers detected by repeated mammograhpic screening naturally regress [30], and the ability to monitor these cancers with non-ionizing radiation would be very useful.

Besides systems specifically designed for breast imaging, significant progress in MWT has been made in the last decade, with experimental prototypes having been used for the imaging of excised pigs' legs [7], human limbs [31] and a canine heart, [32].

1.2 Outline of the Thesis

Although there has been much progress in Microwave Tomography (MWT) for biomedical imaging applications, ranging from advances in inverse algorithms to better data collection technology that has lead to preliminary clinical results, state-of-the-art

[1] However, research into this question continues: it has now been shown that in-vivo permittivity measurements are quite different from ex-vivo permittivities [25]

MWT systems are still at a pre-clinical or early clinical stage (e.g., [26, 27]). We are optimistic that with sufficient research, MWT will become competitive and a widely used clinical medical imaging modality. However, before this occurs, the state-of-the-art must be improved.

Working towards the goal of the creation of such an improved MWT system, the research outlined in this dissertation may be broadly divided into three categories. (I) The understanding, implementation and comparison of differing inversion techniques [33], (II) attempts to improve the MWT in terms of image reconstruction quality [34–36], and (III) the construction, calibration and testing of prototype MWT systems [6, 37].

Part I: Understanding, Implementation and Comparison of differing inversion techniques

In chapter 2, we cover the mathematical background of the inverse problem, a necessary step for quantitative inverse imaging. In chapter 3, we cover, in detail, the derivation of the Multiplicative Regularized Contrast Source Inversion (MR-CSI) method, which is utilized as the inversion method of choice throughout this thesis. These first two chapters comprise the overview/literature review of the inverse problem, and provide the nomenclature and basis for the rest of the thesis.

In chapter 4, we outline a study between the two major classes of (quantitative) inversion techniques currently in use.

Part II: Improvements on MWT: Theoretical and Synthetic Results

In chapter 5, we outline a new version of the Contrast Source Inversion (CSI) method: the Finite-Difference CSI method. With the use of a difference-based (as opposed to integral-based) inverse solver, we are able to utilize arbitrary background media, which is a method of computationally reducing the contrast. We show that this leads to improved inversion when accurate information about the scatterer is available.

In chapter 6, we outline a method of MWT wherein the scatterer in enclosed in a highly-conductive metallic boundary. This entails significant changes to the Green's function of the inverse problem, and these changes are outlined. Synthetic results are presented for the inversion inside of conducting enclosures. While the full implications of this class of MWT are not yet fully understood, some of the possible advantages of this type of imaging are listed and discussed.

Part III: Experimental MWT Prototypes

Chapter 7 provides an overview and shows inversion results from two different MWT prototypes developed at the University of Manitoba. The first system is an open-region, ultra-wideband system which currently operates with an air background, with eventual plans for a liquid matching medium. Preliminary inversion results are shown with data collected with 24 co-resident antennas. The second MWT prototype is an enclosed metallic chamber, also with an air-filled background. As the nature of scattering inside the enclosed chamber is significantly more complicated than for open-region systems,

an exposition on the calibration process is given for the enclosed experimental system. Preliminary images from this system are also shown.

We finish the document with a conclusion, and an outline of the future work which we feel should be performed.

2. MATHEMATICAL FORMULATION OF THE INVERSE ELECTROMAGNETIC PROBLEM

The work of James Clerk Maxwell changed the world forever.
Albert Einstein

This thesis focuses on imaging with the scalar Helmholtz equation, and in this chapter, the derivation of the Helmholtz equation from Maxwell's equation is outlined, and the assumptions required in order to model the full-wave electromagnetic problem with the scalar Helmholtz equation are given. We further give the definitions for the inverse source and inverse scattering problem, and provide an overview of regularization methods.

2.1 Maxwell's equations to the Helmholtz Equation

Electromagnetic phenomena in macroscopic media are described by Maxwell's equations, expressed here in their time-domain differential form:

$$\nabla \times \mathcal{E} = -\frac{\partial \mathcal{B}}{\partial t} \tag{2.1}$$

$$\nabla \times \mathcal{H} = \frac{\partial \mathcal{D}}{\partial t} + \mathcal{J} \tag{2.2}$$

$$\nabla \cdot \mathcal{B} = 0 \tag{2.3}$$

$$\nabla \cdot \mathcal{D} = \rho_t, \tag{2.4}$$

where the vector fields are the electric field intensity, $\mathcal{E}$ [volts/meter] , the magnetic field intensity, $\mathcal{H}$ [amperes/meter], the magnetic flux density $\mathcal{B}$ [teslas], the electric flux density $\mathcal{D}$ [coloumbs/square meter], and the electric current density $\mathcal{J}$ [amperes/square meter]. The charge density ρ_t [coloumbs/cubic meter] is a scalar field, the curl operator is represented by $\nabla\times$ and the divergence operator is represented by $\nabla\cdot$. Additionally, boundary conditions must be specified for the particular electromagnetic problem at hand. The constitutive relations

$$\mathcal{D} = \epsilon_r \epsilon_0 \mathcal{E} \tag{2.5}$$

$$\mathcal{B} = \mu_r \mu_0 \mathcal{H} \tag{2.6}$$

$$\mathcal{J} = \sigma \mathcal{E} \tag{2.7}$$

are used in the presence of material. Here ϵ_0 [farads/meter] is the permittivity of free-space, ϵ_r [unitless] is the relative permittivity, or dielectric constant, μ_0 [henry/meter]

is the permeability of free-space, μ_r [unitless] is the relative permeability and σ [siemens/meter] is the electrical conductivity. In general, ϵ_r, μ_r and σ are tensors of rank-2, but in this work, we consider only isotropic materials, i.e. ϵ_r, μ_r and σ are taken to be scalar quantities. Although the constitutive parameters can be functions of field strength (e.g., μ is often a function of $\mathcal{H}$), we consider only linear materials.

Under the assumption of a time-harmonic dependency of the form $e^{j\omega t}$, where $j = \sqrt{-1}$ is the imaginary unit, and $\omega = 2\pi f$ [rad Hz] is the radial frequency, we may write the time-harmonic Maxwell's equations [38] as

$$\nabla \times \boldsymbol{E} = -j\omega \boldsymbol{B} \tag{2.8}$$

$$\nabla \times \boldsymbol{H} = j\omega \boldsymbol{D} + \boldsymbol{J} \tag{2.9}$$

$$\nabla \cdot \boldsymbol{B} = 0 \tag{2.10}$$

$$\nabla \cdot \boldsymbol{D} = \rho, \tag{2.11}$$

where the time-harmonic forms of the vector fields are represented with bold-face letters, and are related to their time-domain counterparts, e.g., by the formula

$$\mathcal{E} = \sqrt{2} Re\left(\boldsymbol{E} e^{j\omega t}\right). \tag{2.12}$$

Finally, we note that the constitutive relations (2.5 - 2.7) apply to the time-harmonic problem, with the field variables replaced with their time-harmonic representations. In addition, the constitutive parameters will now be complex variables.

2.2 The Helmholtz Equation

While it is possible to utilize the full-vector Maxwell's equations for the inverse problem, we consider only the *scalar* inverse problem, represented by the Helmholtz equation. To understand what approximations are required for this, we begin by assuming that the permeability of all materials is that of free-space, i.e., $\mu_r = 1$. Next, we combine the permittivity and conductivity by defining the *relative complex permittivity*, as

$$\epsilon_r = \epsilon_r' + j\epsilon_r''. \tag{2.13}$$

If we ignore dielectric polarization loss and consider only conductive losses, then

$$\epsilon_r'' = -\frac{\sigma}{\omega}. \tag{2.14}$$

Using (2.13), equations (2.8) and (2.9) may be written as

$$\nabla \times \boldsymbol{E} = -j\omega\mu_0 \boldsymbol{H} \tag{2.15}$$

$$\nabla \times \boldsymbol{H} = j\omega\epsilon_r\epsilon_0 \boldsymbol{E} + \boldsymbol{J}_i. \tag{2.16}$$

where we have added an impressed current (source term) $\boldsymbol{J}_i$. Dividing (2.15) by $-j\omega\mu_0$ and inserting the result into (2.16), we arrive at

$$\frac{1}{-j\omega\mu_0}\nabla\times\nabla\times\boldsymbol{E}-j\omega\epsilon_r\epsilon_0\boldsymbol{E}=\boldsymbol{J}_i. \tag{2.17}$$

This equation may be simplified to [39]

$$\nabla^2\boldsymbol{E}+k^2\boldsymbol{E}+\nabla\left[\boldsymbol{E}\cdot\nabla ln\left(\epsilon\right)\right]=j\omega\mu_0\boldsymbol{J}_i, \tag{2.18}$$

where the wave-number, $k=\omega\sqrt{\epsilon_r\epsilon_0\mu_0}$, and in a rectangular coordinate system

$$\nabla^2=\frac{\partial^2}{\partial x^2}\hat{x}+\frac{\partial^2}{\partial y^2}\hat{y}+\frac{\partial^2}{\partial z^2}\hat{z}, \tag{2.19}$$

where $\hat{x},\hat{y},\hat{z}$ are unit vectors in the three coordinate directions, and $\nabla ln(\epsilon)$ is the gradient of the natural logarithm of the complex permittivity.

The third term in (2.18) couples the different components of the electric field. In order to utilize a scalar model for the MWT problem, we must find a way to eliminate this term from our model. There are several ways in which it either is zero, or may be approximated as zero:

1. If the material parameter ϵ does not vary, then this term is zero. However, this is not a practical situation, a non-varying ϵ would mean there was no scatterer to image.

2. If the material parameter ϵ and the field $\boldsymbol{E}$, do not vary along a particular dimension, e.g., the $\hat{z}$ direction, then the field component in that direction may be modeled by the 2D scalar Helmholtz equation because the third term of (2.18) is zero. This is what occurs in the Transverse Magnetic (TM) problem [38]. This assumption is often used for 2D MWT (e.g., [3–6, 40]).

3. If the complex permittivity varies so slowly with respect to position that it is effectively a constant over distances on the order of a wavelength [39], then the third term may be safely ignored, and the scalar problem applied. This is equivalent to ignoring the charges which build up anywhere there is a change in the permittivity.

4. The third term can just be ignored. This is not as bad an approximation as it may seem: successful 3D experimental imaging of complex targets with significant dielectric variation has been reported while using it [7], and the authors of [7] note that the use of a full-wave model did not improve the imaging results.

Throughout this work, we assume that second condition applies, and further assume that the scalar quantity of interest is the E_z component of the field. For simplicity, we represent the E_z component of the field with the symbol u, and the governing equation of the system becomes the scalar Helmholtz equation:

$$\nabla^2 u + k^2 u = 0, \tag{2.20}$$

Appropriate boundary conditions for the problem must also be applied.

2.3 The Inverse Problem with the Helmholtz Equation

When considering the inverse problem, it is convenient to write the Helmholtz equation with a source term, and explicitly showing the spatial and frequency dependence of the fields/materials:

$$\nabla^2 u(\mathbf{r}, \omega) + k^2(\mathbf{r}, \omega) u(\mathbf{r}, \omega) = -q(\mathbf{r}, \omega), \tag{2.21}$$

where $\mathbf{r} = (x, y, z)$ is a position vector, and we have utilized $q = -j\omega\mu_0 J_{z,i}$ to simplify the source term.

The typical forward problem for the Helmholtz equation involves knowledge of the sources, $q(\mathbf{r}, \omega)$, and the material parameters, $k(\mathbf{r}, \omega)$. The goal is then to determine the fields, $u(\mathbf{r}, \omega)$, for a given set of boundary conditions. This problem results in a unique, stable solution.

When considering the inverse problem for the Helmholtz equation, we must consider two different types of inverse problems: the inverse source and inverse scattering problems. In the inverse source problem, the goal is to calculate the sources, $q(\mathbf{r}, \omega)$, from (often partial, sometimes full) knowledge of the material properties, $k(\mathbf{r}, \omega)$ and

(always) partial knowledge of the field u. In the inverse scattering problem, the source $q(\mathbf{r}, \omega)$ field is typically known (in fact, under our control), as is the field, u for some set of points outside the scatterer. In the inverse scattering problem the material parameters are unknown.

Before we get into the details of these two inverse problems, it is important to ask several fundamental questions about them (this discussion is based on [41]):

1. Does a solution exist?

   From an engineering perspective, the answer to this question is a definitive 'yes', for both the forward and inverse problems. We know that given a particular set of fields, something physical must have created those fields.

   It should be noted that there is a possibility that if the mathematical model used is not a good approximation of the actual physics, the engineering intuition that there must be a solution could conceivably break down.

2. Is the solution unique?

   It is here that the inverse and forward problems begin to differ. In the case of the forward problem, the solution (i.e., the field u) is unique for a given source and scatterer. However, in both the inverse source and inverse scattering problem, there are multiple solutions. In the inverse source problems, there exist non-radiating sources which emit no fields outside a certain region, and thus are not detectable [42, 43]. The sources exist even in the case of perfect measurement

of external fields. In addition to non-radiating sources, there are multiple sources which may give rise to the same field outside of a region[1]. The inverse scattering problem may be unique if one has knowledge of the field for all positions and all frequencies outside of the scatterer [41], but for practical problems the collected information is always of over a limited extent both spatially and in frequency, and the inverse scattering problem is always non-unique for practical problems.

3. Is the solution stable?

   Here, we loosely define stability as the continuity of the output (solution) with respect to the input. That is, a solution is stable if the input changes 'slightly', then the output also changes 'slightly'. In this sense, the forward problem is stable. However, inverse problems are unstable: a small arbitrary change in the input (e.g., the known fields) may result in an arbitrarily large change in the output (e.g., the material parameters). This, combined with non-uniqueness, makes the inverse problem an ill-posed problem in the sense of Hadamard [44]. As the measured fields are unavoidably corrupted with noise in both the inverse source and inverse scattering problems, this lack of stability is probably the largest difficulty to overcome when attempting to solve inverse problems.

   This lack of stability combined with the lack of uniqueness in the inverse problem means that solutions must be regularized: any algorithm attempting to solve an

[1] Consider two spherically shaped sources of different radii radiating at the same frequency, such that the phase of the radiated field is the also the same to an observer. At some distance, the two sources are indistinguishable.

inverse problem must both (a) pick a single solution from the (infinite) number available, and (b) stabilize the solution [45].

4. Does an Algorithm exist to compute the solution?

   Forward problem solutions, both analytic and computational, have been available for many decades. It is only fairly recently (within the last 30 years) that effective methods for solving inverse problems have been discovered/invented for linearized problems, and it is only more recently (≈15 years) that non-linear algorithms have become available. For any reasonably sized problem, these methods are all computational (analytic solutions do exist for some 1-D problems [46], but do not exist for higher dimensional problems). The algorithms currently in use still have many unanswered questions associated with them. For example, iterative algorithms often converge to 'reasonable' solutions from an engineering perspective, but from a mathematical perspective, the exact convergence properties are still poorly understood.

2.3.1 Inverse Source Problem

For MWT, we are ultimately interested in solving the inverse scattering problem. However, the inverse source problem is a special case of the inverse scattering problem, and is easier to solve due to the fact that it is a linear (as opposed to non-linear) ill-posed problem. Thus, it is important to understand the inverse source problem before proceeding to the inverse scattering problem.

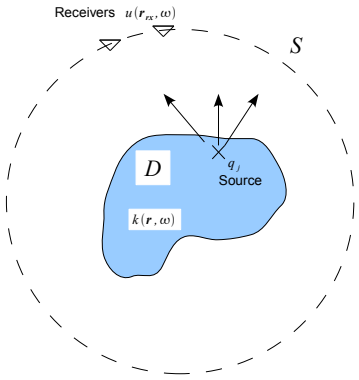

Fig. 2.1: The schematic for the inverse source problem. A source $q(\mathbf{r},\omega)$, located inside the domain D, radiates to a set of receivers at positions $\mathbf{r}_{rx}$, which are located at the measurement domain S (outside of D). The goal is to determine q, from knowledge of $u(\mathbf{r}_{rx},\omega)$, and $k(\mathbf{r},\omega)$

The Helmholtz equation (2.21) provides the starting point for the discussion of the inverse source problem.

Given the governing Helmholtz equation:

$$\nabla^2 u(\mathbf{r},\omega) + k^2 u(\mathbf{r},\omega) = -q(\mathbf{r},\omega) \tag{2.22}$$

with appropriate boundary conditions (ABC's), recover $q(\mathbf{r},\omega)$, $\mathbf{r} \in D$, from knowledge material parameters, $k(\mathbf{r},\omega)$, and limited knowledge of the fields, $u(\mathbf{r}_{rx},\omega)$, $\mathbf{r}_{rx} \in S$. The diagram associated with the inverse source problem is given in Fig. 2.1.

The inverse source problem may be represented in a more convenient format by utilizing operator notation. By writing the solution of the Helmholtz equation (with

the boundary conditions of the problem implicitly understood) as

$$u = \mathcal{G}(q), \tag{2.23}$$

where $\mathcal{G}$ is an operator for the solution of the Helmholtz equation. For example, if we are utilizing an integral form of the operator, (2.23) becomes

$$u = -\int G(\mathbf{r}, \mathbf{r}')q(\mathbf{r}')d\mathbf{r}'. \tag{2.24}$$

The operator G could also be the inverse of a differential operator matrix, as in the Finite-Difference method (see Chapter 5)

With this notation, we formally write the inverse source problem as [41]:

> The Inverse Source Problem:
> Given the inverse Helmholtz operator (the Green's function) G and measurements $u(\mathbf{r}_{rx}, \omega)$, determine $q(\mathbf{r}, \omega)$, $\mathbf{r} \in D$, from
>
> $$u(\mathbf{r}_{rx}, \omega) = -\mathcal{G}_{\mathcal{S}}[q(\mathbf{r}', \omega)] \qquad \mathbf{r}' \in D, \qquad \mathbf{r}_{rx} \in S. \tag{2.25}$$
>
> where we have introduced $\mathcal{G}_{\mathcal{S}}$ to emphasize the restriction of the $\mathcal{G}_{\mathcal{S}}$ operator to the measurement domain S.

Equations of the type shown in (2.25) are known as a linear Fredholm integral equation of the first kind. Due to the fact that $\mathbf{r}_{rx} \notin D$, and the Green's function is smooth (i.e., does not have a singularity associated when $\mathbf{r} \neq \mathbf{r}'$), this problem is ill-posed (i.e., non-unique and unstable [47]) and requires regularization. Note that the forward problem is governed by the same equation as (2.25), except that $\mathbf{r} \in D, S$

and $\mathbf{r}' \in D$. In this case, the Green's function singularity does occur withing the domain D which results in a well-posed (stable and unique) problem. There exists a large literature on how to solve problems of this type. We recommend the book by Hansen [47] and the references therein.

2.3.2 The Inverse Scattering Problem

The inverse scattering problem is more complicated than the inverse source problem due to the fact that there are two unknowns: both the field inside the scattering domain, and the material properties of the scatterer. To complicate matters further, these two unknowns are multiplied together, making the problem nonlinear. A schematic of the inverse scattering problem is shown in Fig. 2.2. To derive the inverse scattering problem, we begin with the Helmholtz equation (repeated here)

$$\nabla^2 u(\mathbf{r},\omega) + k^2(\mathbf{r},\omega)u(\mathbf{r},\omega) = -q(\mathbf{r},\omega), \tag{2.26}$$

again with appropriate boundary conditions. The goal of the inverse scattering problem is to determine $k(\mathbf{r})$ from knowledge of the field u at a set of receiver points and knowledge of the source, q.

With the goal of obtaining a convenient integral representation of the inverse scattering problem, we split the total field, u, into incident and scattered field components:

$$u(\mathbf{r},\omega) = u^{\text{sct}}(\mathbf{r},\omega) + u^{\text{inc}}(\mathbf{r},\omega) \tag{2.27}$$

where u^{inc} is defined as the field when no scatterers are present, u^{sct} is defined as the field caused by the presence of the scatterer, that is

$$\nabla^2 u^{\text{inc}}(\mathbf{r},\omega) + k_b^2(\mathbf{r},\omega)u^{\text{inc}}(\mathbf{r},\omega) = -q(\mathbf{r},\omega), \tag{2.28}$$

where $k_b^2(\mathbf{r},\omega)$ is the known wave number for the background medium (often, but not always a constant). We may subtract (2.28) from (2.26) which results in the equation

$$\nabla^2 u^{\text{sct}}(\mathbf{r},\omega) + k^2(\mathbf{r},\omega)u(\mathbf{r},\omega) - k_b^2(\mathbf{r},\omega)u^{\text{inc}}(\mathbf{r},\omega) = 0. \tag{2.29}$$

Rewritng the third term of (2.29) in terms of the total and scattered parts,

$$\nabla^2 u^{\text{sct}}(\mathbf{r},\omega) + k^2(\mathbf{r},\omega)u(\mathbf{r},\omega) - k_b^2(\mathbf{r},\omega)u(\mathbf{r},\omega) + k_b^2(\mathbf{r},\omega)u^{\text{sct}}(\mathbf{r},\omega) = 0, \tag{2.30}$$

and re-arranging terms, we arrive at

$$\nabla^2 u^{\text{sct}}(\mathbf{r},\omega) + k_b^2(\mathbf{r},\omega)u^{\text{sct}}(\mathbf{r},\omega) = -k_b^2(\mathbf{r},\omega)\left(\frac{k^2(\mathbf{r},\omega)}{k_b^2(\mathbf{r},\omega)} - 1\right)u(\mathbf{r},\omega). \tag{2.31}$$

which is the Helmholtz-equation for the scattered field u^{sct} with the wave-number given by the *known* background medium properties, k_b. The source term on the right

hand side, here represented as s_c, is given by

$$s_c = k_b^2(\mathbf{r},\omega)\left(\frac{k^2(\mathbf{r},\omega)}{k_b^2(\mathbf{r},\omega)} - 1\right) u(\mathbf{r},\omega). \tag{2.32}$$

The source term for the inverse scattering problem is zero outside the scatterer. That is, when $k = k_b$, the source term is zero. All of the unknowns of the inverse scattering problem are now combined into the source term of (2.31), which is why an understanding of the inverse source problem is a necessary pre-cursor to understanding the inverse scattering problem.

Next, we define the *contrast*, χ, as

$$\chi(\mathbf{r},\omega) = \frac{k^2(\mathbf{r},\omega)}{k_b^2(\mathbf{r},\omega)} - 1 = \frac{\epsilon(\mathbf{r},\omega) - \epsilon_b(\mathbf{r},\omega)}{\epsilon_b(\mathbf{r},\omega)} = \frac{\epsilon_r(\mathbf{r},\omega) - \epsilon_{r,b}(\mathbf{r},\omega)}{\epsilon_{r,b}(\mathbf{r},\omega)} \tag{2.33}$$

where $\epsilon_{r,b}$ and ϵ_b are the relative and actual permittivity of the background. All information of the material parameters of the scatterer are contained inside the contrast.

We further define the *contrast sources*, $w(\mathbf{r},\omega)$, as

$$w(\mathbf{r},\omega) = \chi(\mathbf{r},\omega)u(\mathbf{r},\omega). \tag{2.34}$$

Utilizing these contrast sources, we can see that the inverse scattering problem is 'equivalent' to the inverse source problem with the sources given by $k_b^2 w$, and the

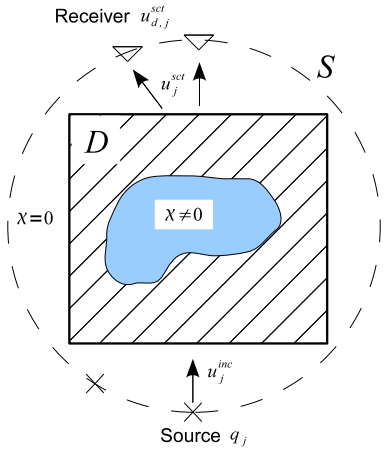

Fig. 2.2: The schematic for the inverse scattering problem. A source $q_j(\mathbf{r},\omega)$, located outside the domain D, radiates an unknown scatterer χ (or k). The scattered field is recorded at positions $\mathbf{r}_{rx}$, which are on the measurement domain S. The goal is to determine χ, from knowledge of $\tilde{u}^{\text{sct}}_j(\mathbf{r}_{rx},\omega)$, and $q_j(\mathbf{r},\omega)$. Importantly, $u_j(\mathbf{r}\in D,\omega)$ is also unknown. Note that the source is does not need to be on the measurement domain S, and multiple sources are possible.

collected fields being the scattered fields u^{sct}.

Having knowledge of the background wave-number means that we may find the inverse Helmholtz operator associated with (2.31) and write

$$u^{\text{sct}}(\mathbf{r},\omega) = \mathcal{G}_S[\chi(\mathbf{r}',\omega)u(\mathbf{r}',\omega)] \qquad \mathbf{r}\in S. \tag{2.35}$$

This is not the final story, however. There are a few more things to emphasize. (i) In the inverse scattering problem, we may create multiple sets of scattered fields by changing our original source, which results in multiple sets of fields, while the contrast, χ, usually remains constant. (ii) We also write the measured fields as $\tilde{u}^{\text{sct}}$ to emphasize that the data are unavoidably corrupted by noise. (iii) We also have an additional

constraint on the total field inside the imaging domain, which may be represented as another equation. These three considerations may be taken into account by formally writing the inverse scattering problem as:

> The Inverse Scattering Problem:
> Determine the material parameters of an unknown scatterer χ, by utilizing the *Data* equation:
>
> $$\tilde{u}_j^{\text{sct}}(\mathbf{r}_{rx}, \omega) = \mathcal{G}_{\mathcal{S}}[\chi(\mathbf{r}', \omega) u_j(\mathbf{r}', \omega)] \qquad \mathbf{r}_{rx} \in S, \mathbf{r}' \in D \tag{2.36}$$
>
> where the fields inside the domain D satisfy the *Domain* or *Object* equation:
>
> $$u_j(\mathbf{r}, \omega) = u_j^{\text{inc}}(\mathbf{r}, \omega) - \mathcal{G}_{\mathcal{D}}[\chi(\mathbf{r}', \omega) u_j(\mathbf{r}', \omega)] \qquad \mathbf{r}, \mathbf{r}' \in D. \tag{2.37}$$

The operator $\mathcal{G}_{\mathcal{D}}$ has been introduced to indicate the solution of the Helmholtz equation inside of the inversion domain D, and the fields have been labeled with an index j which corresponds to a source q_j. In total, there are $j = 1 \ldots J$ sources.

The data (2.36) and domain (2.37) equations form an ill-posed, non-linear system of equations for the two unknowns of χ and u.

2.4 Regularization

The most common way to solve the inverse source (and eventually scattering) problem is to formulate it as a minimization problem of a cost functional. In this case, any inversion method must attempt to minimize the data-equation error:

$$F_{data}(w) = \left\| \tilde{u}^{\text{sct}} - \mathcal{G}_{\mathcal{S}}(w) \right\|_S^2 \tag{2.38}$$

where $\mathcal{G}_{\mathcal{S}}$ is the Green's function operator for the data equation (e.g., $G(\mathbf{r}_{rx} \in S, \mathbf{r}' \in D)$), and $\|v\|_S^2$ is the L_2-norm over the measurement surface S, defined as

$$\|b\|_S^2 = \langle b, b \rangle_S \tag{2.39}$$

where

$$\langle a, b \rangle_S = \int_S a(\mathbf{r}')\overline{b(\mathbf{r}')}d\mathbf{r}' \tag{2.40}$$

is the inner product on the measurement surface S and the overbar denotes the complex conjugate. Almost all inversion algorithms attempt to minimize this functional, which is just another way of stating that we are attempting to find a set of contrast sources which generate the same scattered fields as the measured data. However, because of the fact that the inverse source/scattering problems are ill-posed, a naive attempt to minimize this cost function will result in a non-physical result (i.e., the image will appear very 'noisy', and in general, does not resemble the physical sources/scatterers). From an optimization perspective, non-uniqueness means that there are an infinite number of global minima of (2.38), and the instability means that the starting point of the optimization algorithm is critical. This leads to the need for regularization.

Throughout this work, we define *regularization* as the process of (i) selecting a single solution from the infinite number of possible solutions, and (ii) stabilizing the solution method so that noise in the data does not lead to huge differences in the final solution. One of the major differences between the classes of non-linear inversion

techniques is the chosen method of regularizing the problem.

There are many ways to regularize an ill-posed optimization problem, and by utilizing the minimization of the data equation in its inverse source problem format, we give a brief overview of the basic techniques here. Many of the implementation details when these techniques are used in different inverse solvers are left out, in order to provide a high-level description of regularization.

2.4.1 Truncated Singular Value Decomposition

One of the easiest ways to gain insight into the inverse problem is through the singular value decomposition of the operator and its solution. Assuming that we are solving the inverse source problem for the contrast sources, the functional to be minimized becomes

$$F_{data}(w) = \left\| \tilde{u}^{\text{sct}} - \mathcal{G}_{\mathcal{S}}(w) \right\|_S^2 . \tag{2.41}$$

The Singular Value Decomposition (SVD) of $\mathcal{G}_{\mathcal{S}}$ results in the representation [47–49],

$$\mathcal{G}_{\mathcal{S}}(w) = \sum_{n=1}^{\infty} \lambda_n \langle w, v_n \rangle y_n \tag{2.42}$$

where the λ_n are the singular values, v_n are the right-hand singular functions, and y_n are the left-hand singular functions [47].

In this representation, a solution for the data equation may be represented as [47,48]

$$w = \sum_{n=1}^{\infty} \frac{1}{\lambda_n} \left\langle \tilde{u}^{\text{sct}}, y_n \right\rangle v_n. \tag{2.43}$$

In other words, the solution is obtained by projecting the data onto the left-singular functions, then multiplying the result by the right-singular functions weighted by the inverse of the singular values.

There are three points to make about (2.43):

1. It is the nature of the $\mathcal{G}_{\mathcal{S}}$ operator that the singular values λ_n rapidly approach zero as n increases.

2. The projection of the exact scattered field data onto the left-singular functions $\langle u^{\text{sct}}, y_n \rangle$ will only have significant values for some small number of singular vectors, y_n. In general, the projection gets smaller as n increases.

3. The measured data are unavoidably corrupted with noise, i.e., $\tilde{u}^{\text{sct}} = u^{\text{sct}}(\mathbf{r}) + N(\mathbf{r})$, and the projection of this noise onto the left singular functions $\langle N, y_n \rangle$ will have significant values for almost all values of n. This projection does not tend to get smaller as n increases.

The result of these three points is that the use of an SVD solution for w will always be overwhelmed by the contribution of the noise. In an intuitive way, if $\langle N, y_n \rangle >> \langle u^{\text{sct}}, y_n \rangle$ for some n, then multiplication by $1/\lambda_n$, (which is very large value for large n)

will greatly amplify the contribution from the noise. Even in the case of near-perfect measurements, the discretization errors of machine precision are enough noise to cause instability [48].

One simple method to avoid this instability is to utilize the solution of (2.43), but simply truncate the sum before the noise overwhelms the contribution of the data. This works because the projection of the actual scattered field onto the left-singular function is larger for smaller values of n. This method is known as Truncated Singular Value Decomposition (TSVD). In this method the series trunctation point must be chosen in some way. One possible way is through the *Morozov discrepancy principle* [50], which simply states that the minimum value of the function $F_{data}(w)$ should never be allowed to go lower than the measurement noise. Details of this method are left to the references [47, 48].

It is important to note that any member of the null-space of the operator $\mathcal{G}_{\mathcal{S}}$ may also be added to the solution (2.43) and maintain the equality. In general, the TSVD method assumes that the contributions of any member of the null-space is zero, which makes the solution unique.

2.4.2 Tikhonov Regularization

Tikhonov regularization is the most widely used regularization method in the literature, and examples abound, see [33, 47, 51–57] for just a few. Tikhonov regularization adds a penalty term to the functional:

$$F_{data}^{tikh}(w) = \left\| \tilde{u}^{\text{sct}} - \mathcal{G}_{\mathcal{S}}(w) \right\|_S^2 + \alpha \left\| \mathcal{A}_{\mathcal{T}} \chi \right\|_S^2 \tag{2.44}$$

where $\mathcal{A}_{\mathcal{T}}$ is a 'Tikhonov' operator (usually an identity matrix or the Laplacian operator, ∇^2), and α is a positive real number, known as the *regularization parameter* which is used to balance the weighting between the data equation and the penalty term. Tikhonov regularization will provide a unique solution to the minimization of (2.44), and will also stabilize the mathematical solution as well [48]. It does not, however, guarantee that the solution will be close the the physical contrast sources.

If the Tikhonov operator is the identity operator, then we may again use the singular value decomposition to analyze the solution. In this case, the solution is represented by [48]

$$w_{tikh,\alpha} = \sum_{n}^{\infty} \frac{\lambda_n}{\lambda_n^2 + \alpha} \left\langle \tilde{u}^{\text{sct}}, y_n \right\rangle v_n. \tag{2.45}$$

Thus, the addition of the Tikhonov functional has changed the multiplication of $(1/\lambda_n)$ in the basic SVD solution (2.43) to multiplication by $\lambda_n/(\lambda_n^2 + \alpha)$. The denominator of the latter term will never equal zero (as $\alpha > 0$), and reduce the projection of any noise in the measured data onto the final solution.

The main issue with Tikhonov regularization is the selection of the parameter α. The solution, $w_{tikh,\alpha}$ is extremely sensitive to the value of parameter, and there is no guarantee that $w_{tikh,\alpha}$ will accurately represent the physical contrast sources. There are a large number of choices for Tikhonov regularization parameter selection.

Options include 'considerable numerical experimentation', [7, 58] [19], the discrepancy principle [50], the Normalized Cumulative Periodogram [56], the L-curve [59, 60] and Generalized Cross Validation (GCV) [61]. As Tikhonov regularization is not generally used in this work, the details are left to the references.

2.4.3 Projection Methods

Another possible regularization technique for the inverse source problem is through the use of a projection method. Many iterative optimization methods, e.g., the Conjugate Gradient Least Squares (CGLS) method [19, 62] may be viewed as projecting the solution onto a subspace of some the larger solution space (in the case of CGLS method, the Krylov subspace [63]) at each iteration. By knowing the properties of each dimension of the subspace onto which the solution is projected, one can simply stop the iterative method when enough projections have been made. In practice, this simply means applying the iterative (e.g., CGLS) method and stopping it after a number of iterations.

Again, similar to the TSVD, one must determine some stopping number for the iterations of the iterative method, which requires a similar criterion to TSVD or Tikhonov regularization. As these methods are not used in this thesis, they are not discussed further.

2.4.4 Physical, or Maxwell Regularization

Yet another option for regularization is to use the constraint provided by the domain equation (2.37) and add it to the minimization. This will regularize the problem, often well enough that other forms of regularization are unnecessary. In the literature, this is known as the Maxwell regularizer [64–66], but may also be called the physical regularizer. It is physical in the sense that instead of stabilizing the problem simply through the use of a mathematical stabilizer we are stabilizing the problem through the use of additional *physics*-based information of the problem at hand. In this case, the objective function to be minimized is switched to some variant of the equation

$$F(w) = \left\|\tilde{u}^{\text{sct}} - \mathcal{G}_{\mathcal{S}}(w)\right\|_S^2 + \left\|u^{\text{inc}} - \mathcal{G}_{\mathcal{D}}(w) - u\right\|_D^2 \tag{2.46}$$

where the second term $\left\|u^{\text{inc}} - \mathcal{G}_{\mathcal{D}}(w) - u\right\|_D^2$ is a functional which represents the error in the domain equation, and $\mathcal{G}_{\mathcal{D}}$ is the domain operator, e.g., $G(\mathbf{r} \in D, \mathbf{r}' \in D)$.

As physical regularization is the primary form of regularization used in the inverse scattering method treated in detail in the next chapter, the Contrast Source Inversion (CSI) technique, further discussion is held off for the next chapter.

2.4.5 Multiplicative-Regularization

Another form of regularization is Multiplicative-Regularization (MR). MR involves multiplying the cost functional by a regularization term, and it usually used in

conjunction with other forms of regularization. MR is motivated by image-deblurring techniques, and it may be argued that MR is an image deblurring algorithm applied on top of other forms of regularization. As MR is generally used throughout this work, the details of MR are left to the next chapter.

2.5 Inverse Crimes

Throughout the inverse scattering literature, there is often mention of the *inverse crime* (e.g., [34, 41, 48]). Inverse crimes occur when synthetic data is being utilized to test an inversion algorithm, and that synthetic data is created with a numerical solver which is too similar to the numerical method used in the inverse solver. Effectively, this produces overly optimistic estimations of the power of the inversion algorithm. In particular, inverse crimes occur when both the following conditions are satisfied [48]:

1. The model (e.g. 2D scalar Transverse Magnetic problem) used to produce the forward data is the same as for the inverse model, and

2. The discretization and technique used for the numerical solution (e.g. Method of Moments) for the forward solver are identical to that of the inverse solver.

In practice, these two 'crimes' can be avoided by (i) adding noise to the generated forward data, and (ii) using a different discretization for the forward and inverse solvers (e.g., using 100×100 discretization cells in the forward solver, and 105×105 discretization cells in the inverse solver). This is done with any synthetic data

used throughout this work. The inverse crime is automatically avoided when using experimental data, and in general it is preferred to test inversion algorithms on experimental data.

3. INVERSION METHODS: THE MR-CSI METHOD

> *What I mean is that if you really want to understand something, the best way is to try and explain it to someone else. That forces you to sort it out in your mind. And the more slow and dim-witted your pupil, the more you have to break things down into more and more simple ideas. And that's really the essence of programming. By the time you've sorted out a complicated idea into little steps that even a stupid machine can deal with, you've learned something about it yourself.*
> The character Richard, from *Dirk Gently's Holistic Detective Agency* by Douglas Adams

The data (2.36) and domain (2.37) equations provide us with the fundamental equations that we attempt to solve in the rest of this thesis. There are many different ways to solve these equations, and they may be separated into two major groups: linearized inverse problems, and non-linear inverse problems.

Linearized inverse problems make significant assumptions regarding the wave-propagation within the scatterer, and when applied to realistic problems do not offer enough accuracy to provide quantitative imaging (although they may be very useful for non-quantitative imaging and are widely used, see, e.g. [9, 14, 15, 29, 67, 68]). These linear techniques may also be called Fourier-based imaging techniques, and often called radar-based techniques. While these techniques may often seem to be distinct from

the non-linear scattering problem, and are often listed as a separate solution method, e.g. [9], we have shown that they are, at their core, a linearized solution of the inverse scattering problem [69]. Due to the fact that linear methods are not further discussed in this dissertation, the details of an example Fourier imaging algorithm have been left to the Appendix A.

The non-linear inversion techniques discussed in the previous chapter are able to provide successful quantitative reconstructions of biological materials from experimentally collected data at limited (even single) frequencies. The main advantage of these 'full' inversion techniques, as opposed to the linearized techniques, is that a quantitative inversion of such material parameters as conductivity and permittivity goes a lot further toward solving the clinical identification problem, e.g. tumour or no tumour, and makes the technique much more useful for biomedical applications.

To date, the only effective way to perform quantitative inversion is through iterative methods based on minimizing some type of cost functional. The non-linear inversion techniques offer a quantitative reconstruction of the contrast but are mathematically more complicated than the linearized techniques, and usually take significantly more computational resources to solve. Broadly speaking, there are two different approaches that have been successfully used to solve the inverse scattering problem [70]. The two approaches are distinguished by their method used to regularize the ill-posed problem, their use (or lack of use) of a forward solver, as well as the selection of the objective function that is minimized. The first approach, known as the conventional

type, formulates the objective function based solely on the scattered data outside the scatterer or Object of Interest (OI) and uses repeated calls to a forward solver during the iterative minimization. Examples of this technique include the Distorted-Born Iterative Method (DBIM) [53] and global optimization techniques (e.g. [71]). The DBIM is equivalent to the Gauss-Newton (GN) method. The second class of approaches, which are distinguished by the absence of a forward solver and the use of an objective function based on both scattered fields outside the OI and total fields inside the OI, is known as the modified gradient type. The two examples of this class of inversion technique are the Modified Gradient Method (MGM) [66] and the Contrast Source Inversion (CSI) method [31, 64].

3.1 Conventional Class Inverse Scattering Algorithms

The conventional type inverse scattering algorithms primarily utilize the data misfit equation of (2.38). However, for the inverse scattering problem the data equation must also be enforced. Thus, conventional non-linear inversion techniques formulate the inverse scattering problem as:

$$\begin{aligned} \chi &= \arg\min_{\chi} \sum_{j=1}^{J} \left\| \tilde{u}^{\mathrm{sct}} - \mathcal{G}_{\mathcal{S}} \left\{ \chi u_j \right\} \right\|_S^2 \\ \text{subject to} : u_j^{\mathrm{inc}}(\mathbf{r}) &= u_j(\mathbf{r}) - \mathcal{G}_{\mathcal{D}} \left\{ \chi u_j \right\} \qquad \mathbf{r} \in D \end{aligned} \tag{3.1}$$

where again, the number of transmitters (sources) is $j = 1 \dots J$. For the conventional type algorithms, e.g., DBIM, which only use the data misfit cost-functional, there is a choice as to when the regularization is applied. The data misfit cost-functional may be regularized before the optimization process, e.g., [70, 72], or the cost-functional may be regularized at each step of the optimization process (once the problem has been linearized) [19, 53].

No matter which method of regularization is selected, the conventional techniques (i) require the selection of some regularization parameter and (ii) require the use of a forward solver. These techniques proceed by creating an estimate of the contrast, χ_n, then enforcing domain equation (2.37) and calculating the new estimate of the scattered fields through the use of a forward solver. Optimization techniques used to determine the update of the contrast include the Gauss-Newton method [19, 70, 72] and genetic algorithms [71].

As the implementation of the GN/DBIM method was the responsibility of another co-author of [33] we provide only a brief description of DBIM algorithm. The details are left to the reference [33].

3.2 Distorted Born Iterative Method

The Distorted Born Iterative Method, originally proposed by Chew and Wang [53], tries to solve the nonlinear minimization problem given in (3.1) through an iterative procedure by alternately updating the guesses of the contrast, χ, and the field, u,

inside the imaging domain D. Briefly, the DBIM may be summarized as follows:

1. (*Initialization*) Born approximation: assume that the total field in D is the incident field, $u_j(\mathbf{r} \in D) \approx u_j^{\text{inc}}$.

2. (*Initialization*) Solve for the contrast, χ, by minimizing the data equation (2.36). This step requires regularization.

3. Use the new estimate of the contrast as the input to a forward solver and generate a new estimate of the total field, u_n.

4. Check convergence of the algorithm, based on the relative data equation error. That is, if the term

$$F^S = \frac{\sum_j \left\| \tilde{u}_j^{\text{sct}} - u_j^{\text{sct}}(\chi_n, u_{j,n}) \right\|_S^2}{\sum_j \left\| \tilde{u}_j^{\text{sct}} \right\|_S^2} \tag{3.2}$$

   is below a set threshold, the algorithm is stopped. Here, χ_n is the predicted contrast at the nth iteration of the algorithm, and $u_{j,n}$ is the estimate of the total field inside of D at the same iteration.

5. The distorted Green's function operator is written as

$$\mathcal{G}_{\mathcal{S}n}\{\psi\} = \int k_{b,n}^2(\mathbf{r}') G_n(\mathbf{r}, \mathbf{r}') \psi(\mathbf{r}') d\mathbf{r}', \tag{3.3}$$

   where $\mathbf{r} \in S$, $k_{b,n}$ is the wavenumber of the inhomogeneous background with

respect to χ_n, and G_n is the distorted Green's function of the inhomogeneous background χ_n. In order to compute G_n we use the forward solver once for each receiver location [53].

6. Utilizing the Distorted Green's operator, and the fields from step 3, update the contrast in the form of $\chi_{n+1} = \chi_n + \delta\chi_n$ where $\delta\chi_n$ is obtained by solving the minimization problem:

$$\delta\chi_n = \arg\min_{\delta\chi} \sum_j \left\| \tilde{u}_j^{\text{sct}} - u_j^{\text{sct}}(\chi_n, u_{j,n}) - \mathcal{G}_{\mathcal{S}_n}\{\delta\chi u_{m,n}\} \right\|_S^2 . \tag{3.4}$$

7. Go back to step 3.

Note that (3.4) is similar to the initial minimization of the data equation, but is different in the critical respects that it is solving for a relative change in the permittivity and that the operator $\mathcal{G}_{\mathcal{S}_n}$ is the distorted operator. To enhance the convergence of DBIM, we employ a line search algorithm similar to [72]: if the error in the data equation due to the correction $\delta\chi_n$ increases, the contrast is updated in the form of $\chi_{n+1} = \chi_n + \upsilon_n\delta\chi_n$ where υ_n is the appropriate step size. The details of the utilized line search algorithm are not presented here but are available in [72].

For the regularization in step two, we utilize Tikhonov regularization, and the regularization parameter is chosen via an efficient form of the L-curve method [33].

3.3 Modified Gradient Class Inversion Algorithms and Contrast Source Inversion

The key difference between modified gradient type and conventional type inversion algorithms is that the modified gradient type use the physical, or Maxwell regularizer discussed in section 2.4.4. Because of this, they typically do not require the use of a forward solver at each step of the minimization process in order to enforce the object/domain equation. At present, there are only two examples of this class of algorithm, the Modified Gradient Method [66] and the Contrast Source Inversion (CSI) technique [58, 64, 65, 73, 74].

Due to several important factors with regards to the modified-gradient type inversion algorithms, namely:

1. they are computationally efficient, do not require the use of a forward solver at each iteration, and use computational resources comparable to two forward solver calls, and

2. they may be formulated in such a way that all regularization is completed automatically,

we have decided, for this work, to implement the leading modified-gradient type method, the CSI technique. Details of the CSI technique are provided below.

3.4 Derivation of the MR-CSI Algorithm

The CSI method begins by using the contrast sources, $w_j = \chi u_j$ and re-writing the domain equation (2.37) as

$$\chi u_j^{\text{inc}} = w_j - \chi \mathcal{G}_{\mathcal{D}} \{w_j\} . \tag{3.5}$$

The CSI is formulated as an iterative optimization algorithm but with the objective function written with respect to the contrast and the contrast sources:

$$\begin{aligned} F(w_j, \chi) &= F^S(w_j) + F^D(\chi, w_j) = \\ &\frac{\sum_j \left\| \tilde{u}_j^{\text{sct}} - \mathcal{G}_{\mathcal{S}} \{w_j\} \right\|_S^2}{\sum_j \left\| \tilde{u}_j^{\text{sct}} \right\|_S^2} + \frac{\sum_j \left\| \chi u_j^{\text{inc}} - w_j + \chi \mathcal{G}_{\mathcal{D}} \{w_j\} \right\|_D^2}{\sum_j \left\| \chi u_j^{\text{inc}} \right\|_D^2} \end{aligned} \tag{3.6}$$

The normalization terms in the denominators are used to balance between the data and domain equation errors.

In the basic CSI method the objective function (3.6), is minimized via the formation of two interlaced sequences of the unknowns: a sequence of estimates of the contrast, $\{\chi_n\}$ which is interlaced with a sequence of estimates of the contrast sources $\{w_n\}$ where n represents the iteration number. For every step of the basic CSI method, the contrast source sequence is updated via a single step of the Conjugate-Gradient [75] minimization algorithm while assuming that the contrast is constant. After this, the contrast is updated by minimizing the domain equation functional. The iterative

process is continued until a desired minimum of the objective function is reached.

In order to derive the details of the CSI method, we first introduce the data error at the n^{th} step of the CSI algorithm, $\rho_{j,n}$, as

$$\rho_{j,n} = \tilde{u}_j^{\text{sct}} - \mathcal{G}_{\mathcal{S}}(w_{j,n}), \tag{3.7}$$

and the domain or object error at the n^{th} iteration as

$$r_{j,n} = \chi_n u_{j,n} - w_{j,n}. \tag{3.8}$$

The estimate of the total field at iteration n is given by

$$u_{j,n} = u_j^{\text{inc}} + \mathcal{G}_{\mathcal{D}}(w_{j,n}). \tag{3.9}$$

3.4.1 Update of the Contrast Sources

Assuming that the CSI algorithm has been initialized, and $w_{j,n-1}$ and χ_{n-1} are known, we update the contrast sources with the following formula:

$$w_{j,n} = w_{j,n-1} + \alpha_{j,n}^w v_{j,n}, \tag{3.10}$$

where $v_{j,n}$ are the search directions, and $\alpha_{j,n}^w$ is the search distance for each transmitter.

Search Direction and Distance

The basic search directions for the contrast sources are are given by

$$v_{j,0} = 0, \qquad v_{j,n} = g^w_{j,n} + \gamma^w_{j,n} v_{j,n-1} \tag{3.11}$$

where $g^w_{j,n}$ is the gradient of the cost functional (3.6) with respect to the j^{th} contrast source, $\gamma_{j,n}$ is the search distance. These two parameters are discussed below.

Calculation of gradients with respect to the contrast sources

The calculation of the gradients requires the derivative of the functional $F(w_{j,n}, \chi_n)$ with respect to $w_{j,n}$. Derivatives of this nature are known as Fréchet derivatives, and their definition is given in appendix B.

In particular, we are interested in the gradient of the cost functional with respect to w_j, evaluated at $w_j = w_{j,n-1}$:

$$g^w_{j,n} = \left.\frac{\partial F^S(w_j)}{\partial w_j}\right|_{w_j = w_{j,n-1}} + \left.\frac{\partial F^D(\chi_{n-1}, w_j)}{\partial w_j}\right|_{w_j = w_{j,n-1}}. \tag{3.12}$$

Using the definition of the Fréchet derivative given in appendix B:

$$\begin{aligned}
\frac{\partial F^S(w_j)}{\partial w_j} &= \lim_{\epsilon\to 0}\frac{F^S(w_j+\epsilon g_j)-F^S(w_j)}{\epsilon} \\
&= \lim_{\epsilon\to 0}\frac{\eta^S}{\epsilon}\left[\|\rho(w_j+\epsilon g_j)\|_S^2-\|\rho(w_j)\|_S^2\right] \\
&= \lim_{\epsilon\to 0}\frac{\eta^S}{\epsilon}\left[\|\rho(w_j)-\epsilon\mathcal{G}_{\mathcal{S}}(g_j)\|_S^2-\|\rho(w_j)\|_S^2\right] \\
&= \lim_{\epsilon\to 0}\frac{\eta^S}{\epsilon}\left[-2\epsilon Re\left\langle\rho(w_j),\mathcal{G}_{\mathcal{S}}(g_j)\right\rangle_S+\epsilon^2\left\|\mathcal{G}_{\mathcal{S}}(g_j)\right\|_S^2\right] \\
&= -2\eta^S Re\left\langle\rho(w_j),\mathcal{G}_{\mathcal{S}}(g_j)\right\rangle_S \\
&= Re\left\langle-2\eta^S\mathcal{G}_{\mathcal{S}}^*\left[\rho(w_j)\right],g_j\right\rangle_D, \qquad (3.13)
\end{aligned}$$

In (3.13), ρ is given in eq. (3.7), η^S is given by

$$\eta^S=\left[\sum_j\left\|\tilde{u}^{\text{sct}}\right\|_S^2\right]^{-1}, \qquad (3.14)$$

and $\mathcal{G}_{\mathcal{S}}^*$ is the adjoint operator of $\mathcal{G}_{\mathcal{S}}$, defined as the operator which satisfies the equation

$$\left\langle a,\mathcal{G}_{\mathcal{S}}(b)\right\rangle_S=\left\langle\mathcal{G}_{\mathcal{S}}^*(a),b\right\rangle_D, \qquad (3.15)$$

where $a\in S$ is a member of the measurement domain, and $b\in D$ is a member of the domain D.

Thus, the gradient (see Appendix B) of the data error, evaluated at $w_j=w_{j,n-1}$ is

given by

$$\left.\frac{\partial F^S(w_j)}{\partial w_j}\right|_{w_j=w_{j,n-1}} = -2\eta^S \mathcal{G}_{\mathcal{S}}^* \left[\rho(w_{j,n-1})\right]. \tag{3.16}$$

The gradient of the domain equation portion is calculated in a similar way. We first define $r(w_j) = \chi_{n-1} u_j^{\text{inc}} - w_j + \chi_{n-1}\mathcal{G}_{\mathcal{D}}(w_j)$ and then:

$$\begin{aligned}
\frac{\partial F_n^D(\chi_{n-1}, w_j)}{\partial w_j} &= \lim_{\epsilon\to 0} \frac{F_n^D\left(\chi_{n-1}, w_j + \epsilon g_j\right) - F_n^D\left(\chi_{n-1}, w_j\right)}{\epsilon} \\
&= \lim_{\epsilon\to 0} \frac{\eta_n^D}{\epsilon} \left\|r(w_j + \epsilon g_j)\right\|_D^2 - \left\|r(w_j)\right\|_D^2 \\
&= \lim_{\epsilon\to 0} \frac{\eta_n^D}{\epsilon} \left\|r(w_j) - \epsilon\left[g_j - \chi_{n-1}\mathcal{G}_{\mathcal{D}}(g_j)\right]\right\|_D^2 - \left\|r(w_j)\right\|_D^2 \\
&= \lim_{\epsilon\to 0} \frac{\eta_n^D}{\epsilon} \left\{-2\epsilon Re\left\langle r(w_j), \left[g_j - \chi_{n-1}\mathcal{G}_{\mathcal{D}}(g_j)\right]\right\rangle_D + \right. \\
&\quad \left. \epsilon^2 \left\|g_j - \chi_{n-1}\mathcal{G}_{\mathcal{D}}(g_j)\right\|_D^2\right\} \\
&= -2\eta_n^D Re\left\langle r(w_j), \left[g_j - \chi_{n-1}\mathcal{G}_{\mathcal{D}}(g_j)\right]\right\rangle_D \\
&= Re\left\langle -2\eta_n^D \left\{r(w_j) - \mathcal{G}_{\mathcal{D}}^*\left[\overline{\chi_{n-1}} r(w_j)\right]\right\}, g_j\right\rangle_D,
\end{aligned} \tag{3.17}$$

where, η_n^D is given by

$$\eta_n^D = \left[\sum_j \left\|\chi_{n-1} u_j^{\text{inc}}\right\|_D^2\right]^{-1}, \tag{3.18}$$

and $\mathcal{G}_{\mathcal{D}}^*$ is the adjoint operator of $\mathcal{G}_{\mathcal{D}}$, which is defined as the operator which satisfies

$$\left\langle a, \mathcal{G}_{\mathcal{D}}(b)\right\rangle_D = \left\langle \mathcal{G}_{\mathcal{D}}^*(a), b\right\rangle_D, \tag{3.19}$$

where $a \in D$ is an element of the space D, and $b \in D$ is a element of the space D.

Thus, the gradient of the domain equation functional is given by

$$\left.\frac{\partial F^D(\chi_{n-1}, w_j)}{\partial w_j}\right|_{w_j=w_{j,n-1}} = -2\eta_n^D \left\{ r_{j,n-1} - \mathcal{G}_{\mathcal{D}}^* \left[\overline{\chi_{n-1}} r_{j,n-1} \right] \right\}. \tag{3.20}$$

Polak-Ribière Search Directions

In the CSI method, the search directions are selected to be the Polak-Ribière search directions [58, 64, 76]. For this case, $\gamma_{j,n}^w$ is given by

$$\gamma_{j,n}^w = \frac{Re \left\langle g_{j,n}^w, g_{j,n}^w - g_{j,n-1}^w \right\rangle_D}{\left\langle g_{j,n-1}^w, g_{j,n-1}^w \right\rangle_D}. \tag{3.21}$$

Finally, the search distance, $\alpha_{j,n}^w$, in (3.10) is found by finding the minimum of the cost functional (3.6) along the search direction $v_{j,n-1}$. Explicitly,

$$\begin{aligned} F_n &= \eta^S \sum_j \left\| \tilde{u}_j^{\text{sct}} - \mathcal{G}_{\mathcal{S}} \left\{ w_{j,n} \right\} \right\|_S^2 + \eta_{n-1}^D \sum_j \left\| \chi u_j^{\text{inc}} - w_{j,n} + \chi_{n-1} \mathcal{G}_{\mathcal{D}} \left\{ w_{j,n} \right\} \right\|_D^2 \\ &= \eta^S \sum_j \left\| \rho_{j,n-1} - \alpha_{j,n}^w \mathcal{G}_{\mathcal{S}} \left\{ v_{j,n} \right\} \right\|_S^2 + \\ &\quad \eta_{n-1}^D \sum_j \left\| r_{j,n-1} - \alpha_{j,n}^w \left(v_{j,n} + \chi_{n-1} \mathcal{G}_{\mathcal{D}} \left\{ v_{j,n} \right\} \right) \right\|_D^2, \end{aligned} \tag{3.22}$$

and by setting $\partial F_n / \partial \alpha_{j,n}^w = 0$, we may obtain

$$\alpha_{j,n}^w = \frac{\left\langle g_{j,n}^w, v_{j,n}^w \right\rangle_D}{\eta^S \left\| \mathcal{G}_{\mathcal{S}}(v_{j,n}) \right\|_S^2 + \eta_{n-1}^D \left\| v_{j,n} - \chi_{n-1} \mathcal{G}_{\mathcal{D}}(v_{j,n}) \right\|_D^2}. \tag{3.23}$$

3.4.2 Update of the Contrast

At each iteration of the CSI method, the contrast χ is updated after the update of the contrast sources w_j. In the basic CSI method, this update is chosen by minimizing the cost functional with respect to the contrast, while assuming the contrast sources are constant. Further, we make the approximation that η_n^D does not depend on χ. As F^S in (3.6) does not depend on χ, this means minimizing

$$\frac{1}{\eta_n^D} F^D(w_{j,n}, \chi_n) = \sum_j \left\| \chi u_j^{\text{inc}} - w_j + \chi \mathcal{G}_{\mathcal{D}} \{w_j\} \right\|_D^2 = \sum_j \left\| \chi u_j - w_j \right\|_D^2 \tag{3.24}$$

with respect to the contrast χ_n. This results in a minimizer

$$\chi_n^a = \frac{\sum_j w_{j,n} \overline{u}_{j,n}}{\sum_j |u_{j,n}|}, \tag{3.25}$$

which is the updated contrast at step n.

3.4.3 CSI Initialization

The CSI method needs a starting point. In practice, this may be a contrast (χ_0), from which the contrast sources may be calculated (which requires a forward solver), or it may be initialized with some guess at the contrast sources, $w_{j,0}$. The standard method [31, 58, 64, 74] is to initialize the contrast sources by minimizing the data equation functional:

$$F^{\text{data}}(w_j) = \left\| \tilde{u}_j^{\text{sct}} - \mathcal{G}_{\mathcal{S}} \{w_j\} \right\|_S^2. \tag{3.26}$$

The details of this minimization may be found in the appendices, section B.2, and the solution is given by

$$w_j^{\text{bp}} = \frac{\left\|\mathcal{G}_{\mathcal{S}}^* \tilde{u}_j^{\text{sct}}\right\|_D^2}{\left\|\mathcal{G}_{\mathcal{S}}\mathcal{G}_{\mathcal{S}}^* \tilde{u}_j^{\text{sct}}\right\|_S^2} \mathcal{G}_{\mathcal{S}}^* \tilde{u}_j^{\text{sct}}. \tag{3.27}$$

Once the contrast sources have been initialized, the initial contrast χ_0 is also initialized through the use of equation (3.25), where

$$u_{j,0} = u_j^{\text{inc}} + \mathcal{G}_{\mathcal{D}} w_j^{\text{bp}}. \tag{3.28}$$

3.4.4 Multiplicative Regularization

While the CSI method alone may provide good inversion results on its own (e.g., [64]), the method may be significantly enhanced through the use of a total-variation based regularizer (see, e.g., [31, 58, 77–80]). In general, a total variation regularizer attempts to penalize contrasts which have a large total variation (intuitively, it penalizes contrasts which look 'noisy', and have significant variation from pixel to pixel). The total-variation of a differentiable function, h, $h \in D$, is defined as

$$TV\left[h(\mathbf{r})\right] = \int_D \left|\nabla h(\mathbf{r})\right| d\mathbf{r}. \tag{3.29}$$

Inspired by the use of total-variation based regularizers for imaging processing [81], several regularizers based on different weightings of total-variations of the contrast have been implemented and tested in the literature [58, 78]. Initially, these regularizers were

tested as an additive regularizer [58], but this requires the choice of a parameter used to balance the effect of the total-variation term and the regular cost functional (3.6). This leads to similar problems as with the selection of the Tikhonov weighting parameter discussed in section 2.4.2. The parameter selection process may be avoided by applying the total-variation based regularizer as a *Multiplicative* Regularizer (MR) [58, 78].

With the MR term, the CSI cost function then becomes

$$F_n(w_j, \chi) = F_n^{MR}(\chi) \left[F^S(w_j) + F^D(\chi, w_j) \right]. \tag{3.30}$$

Multiple testing of different regularizers [58, 78] has lead to a clear leader for the purposes of MWT: the weighted L_2-norm multiplicative regularizer. This regularizer is given by

$$F_n^{MR}(\chi) = \int_D b_n^2(\mathbf{r}) \left(|\nabla \chi(\mathbf{r})|^2 + \delta_n^2 \right) \mathrm{d}\mathbf{r}, \tag{3.31}$$

where

$$b_n^2(\mathbf{r}) = \frac{1}{A \left(|\nabla \chi_{n-1}(\mathbf{r})|^2 + \delta_n^2 \right)}, \tag{3.32}$$

and the term δ_n^2 has been added to ensure the differentiability to the regularizer, and is given by

$$\delta_n^2 = \frac{F_n^D(\chi_{n-1}, w_{j,n-1})}{\Delta} \tag{3.33}$$

where the area of the inversion domain D is $A = \int_D \mathrm{d}\mathbf{r}$, and Δ is the area of an inversion pixel.

The introduction of this regularizer has no effect on the updating of the contrast sources. This is because $F_n^R(\chi)$ does not depend on w_j, and is equal to 1 when $\chi = \chi_{n-1}$. However, the updating of the contrast itself needs to change. In the MR-CSI method this is done by

1. using the basic update of (3.25) as the first guess at each step of the CSI algorithm, then

2. applying a single step of the CG algorithm to update the contrast again. The Polak-Ribière directions are again utilized.

The second contrast update required for the MR-CSI method is given by

$$\chi_n^{MR} = \chi_n^a + \beta_n d_n \tag{3.34}$$

where d_n are again chosen as the Polak-Ribière directions:

$$d_0 = 0 \qquad d_n = g_n^\chi + \frac{Re\left\langle g_n^\chi, g_n^\chi - g_{n-1}^\chi \right\rangle_D}{\left\langle g_{n-1}^\chi, g_{n-1}^\chi \right\rangle_D} d_{n-1}. \tag{3.35}$$

To determine these directions, we need to calculate the gradient of the total

objective function with respect to χ which is given by

$$\begin{aligned} g_n^{\chi} &= \left.\frac{\partial F_n(\chi, w_{j,n})}{\partial \chi}\right|_{\chi=\chi_n^a} \\ &= F_n^{MR}(\chi_n^a)\left.\frac{\partial F_n^D(\chi, w_{j,n})}{\partial \chi}\right|_{\chi=\chi_n^a} + \\ &\quad \left[F^S(w_{j,n}) + F_n^D\left(\chi_n^a, w_{j,n}\right)\right]\left.\frac{\partial F_n^{MR}(\chi)}{\partial \chi}\right|_{\chi=\chi_n^a}, \end{aligned} \tag{3.36}$$

where χ_n^a is the contrast given in (3.25).

Due to the fact that χ_n^a is a minimizer of F_n^D, $\partial F_n^D/\partial\chi$ evaluated at $\chi = \chi_n^a$ is zero. Thus, we only need to calculate [74]

$$\begin{aligned} \frac{\partial F_n^{MR}(\chi)}{\partial \chi} &= \lim_{\epsilon\to 0}\frac{F_n^{MR}(\chi+\epsilon d) + F_n^{MR}(\chi)}{\epsilon} \\ &= \lim_{\epsilon\to 0}\frac{\|b_n\nabla\left(\chi+\epsilon d\right)\|_D^2 - \|b_n\nabla\chi\|_D^2}{\epsilon} \\ &= 2Re\left\langle b_n\nabla\chi, b_n\nabla d\right\rangle_D \\ &= 2Re\int_D b_n^2\nabla\chi(\mathbf{r})\cdot[\nabla d(\mathbf{r})]^H d\mathbf{r} \\ &= 2Re\left(-\int_D\left\{\nabla\cdot\left[b_n^2(\mathbf{r})\nabla\chi(\mathbf{r})\right]\right\}[d(\mathbf{r})]^H d\mathbf{r}\right) \\ &= Re\left\langle -2\nabla\cdot\left(b_n^2\nabla\chi\right), d\right\rangle_D. \end{aligned} \tag{3.37}$$

Thus, under the definition of Fréchet derivative given in appendix B,

$$\frac{\partial F_n^{MR}(\chi)}{\partial \chi} = -2\nabla\cdot\left(b_n^2\nabla\chi\right). \tag{3.38}$$

The final step of the MR update is to determine the step size of the CG step, β_n from (3.34). This is done by solving

$$\beta_n = \text{argmin}_{\text{real}\beta} \left\{ F_n \left(w_{j,n}, \chi_n + \beta d_n \right) \right\}. \tag{3.39}$$

It is possible to determine the parameter β analytically. The cost-functional F_n becomes [31]

$$\begin{aligned} F_n(w_(j,n) \;=\; & \Big[F_n^S(w_j, n) + F_n^D(w_{j,n}, \chi_{n-1}) + \beta^2 \eta_n^D \sum_j \| d_n u_{j,n} \|_D^2 \\ & + 2\beta \eta_n^D Re \sum_j \langle d_n u_{j,n}, \chi_{n-1} u_{j,n} - w_{j,n} \rangle_D \Big] \\ & \times \left[1 + 2\beta Re \left\langle b_{n-1} \nabla \chi_{n-1}, b_{n-1} \nabla d_n \right\rangle_D + \right. \\ & \left. \beta^2 \left\| b_{n-1} \nabla d_{n-1} \right\|_D^2 \right] \end{aligned} \tag{3.40}$$

By setting the derivative of this functional with respect to β to zero, a cubic equation in β results. There are one real and two complex roots of the cubic equation, and the real root is the minimizer of (3.39) [31, 74, 78].

An important aspect of weighted-L_2 MR process is that, when β is taken to be real, it may be proven [78] that the MR term does not add any extra local minima to the overall cost function.

3.5 Implementation of the Data and Domain Operators

Until now, the specifics of the $\mathcal{G}_{\mathcal{S}}$ and $\mathcal{G}_{\mathcal{D}}$ operators has been left intentionally vague. For most cases considered in this thesis (besides those in Chapter 5), these operators are implemented as integral operators of the form:

$$\mathcal{G}_{\mathcal{S}}(h) = -k_b^2 \int_D G(\mathbf{r}, \mathbf{r}')h(\mathbf{r}')d\mathbf{r}' \qquad \mathbf{r} \in S, \mathbf{r}' \in D, \tag{3.41}$$

and

$$\mathcal{G}_{\mathcal{D}}(h) = -k_b^2 \int_D G(\mathbf{r}, \mathbf{r}')h(\mathbf{r}')d\mathbf{r}' \qquad \mathbf{r}, \mathbf{r}' \in D, \tag{3.42}$$

where $G(\mathbf{r}, \mathbf{r}')$ is the Green's function for the Helmholtz equation (2.21) with the appropriate boundary conditions. It is important to note that in the MR-CSI method, these operators are not integral equations, but are rather just integrals (as h is always known in MR-CSI). Thus, their solution at each step is much less computationally intensive than a full integral equation. The inversion domain D is discretized on a regular rectangular grid, and integrals involved with the $\mathcal{G}_{\mathcal{S}}$ and $\mathcal{G}_{\mathcal{D}}$ are solved using Richmond's method [82]. In the open-region case, the operator $\mathcal{G}_{\mathcal{D}}$ is accelerated with the use of Fast-Fourier Transforms (FFT's) [83, 84]. In the case of enclosed-region imaging (see Chapter 6) it is not possible to utilize FFT's, and acceleration is not used.

Tab. 3.1: Computational Cost of MR-CSI Algorithm

For each iteration of main MR-CSI optimization loop: M_{cg}^{CSI}
  For each transmitter: T_x
    Data ($\mathcal{G}_{\mathcal{S}}$,$\mathcal{G}_{\mathcal{S}}^*$) Operators: $\propto 2R_x^{\text{act}}N$
    Domain ($\mathcal{G}_{\mathcal{D}}$,$\mathcal{G}_{\mathcal{D}}^*$) Operators: $\propto 3NlogN$
  end
end

3.5.1 Computational Complexity of MR-CSI

The computational bottle-neck of the MR-CSI method is the $\mathcal{G}_{\mathcal{D}}$ operator. In the usual case, the $\mathcal{G}_{\mathcal{D}}$ operator scales with $O(NlogN)$ computational time, where N is the number of unknowns in the discretization. A detailed computational cost of the algorithm is given in pseudo-code in Table 3.5.1, where the following conventions are used: the number of transmitters is given by T_x, the number of active receivers for each transmitter is R_x^{act}, and the number of iterations required for the main optimization loop in the CSI algorithm is denoted by M_{cg}^{CSI}. In Table 3.5.1 we have ignored any operations which are proportional to N, which includes the contrast update for both the CSI and MR-CSI algorithms.

Each step of the MR-CSI method requires calling the $\mathcal{G}_{\mathcal{D}}$ operator once, and the $\mathcal{G}_{\mathcal{D}}^*$ operator twice, and requires calling both the $\mathcal{G}_{\mathcal{S}}$ and $\mathcal{G}_{\mathcal{S}}^*$ operator R_x^{act} times. Thus, the overall scaling of the algorithm is $O(NlogN)$. Due to the fact that each iteration requires only an integral, rather than an integral equation, the overall algorithm takes about 2 times the amount of computational time as a forward solver for the same problem [58, 64].

4. COMPARISON OF INVERSION TECHNIQUES

Mathematics seems to endow one with something like a new sense.
Charles Darwin

In a previous paper [33], our research group considered and compared an example of each of the two primary types of inversion techniques in use for quantitative MWT: the conventional, and modified gradient types. The comparison was completed by blindly inverting a wide range of scattering data collected from multiple MWT systems (by blindly, we mean that no extra information about the scatterer was used in the inversion process). For this comparison, we utilized the MR-CSI algorithm, and the DBIM algorithm. Both inversion techniques were applied to the 2D TM (scalar) inverse problem. While both conventional and modified gradient types of inversion algorithms have provided successful microwave imaging results, the relative performance of these two groups of algorithms, in terms of inversion quality, regularization needs, and computational resources, was poorly understood. We show this comparison and present some of those results here.

The MR-CSI algorithm used for this comparison was outlined in the previous

chapter. The DBIM algorithm utilizes Tikhonov regularization, with the Laplacian as Tikhonov operator (see section 2.4.2). The DBIM algorithm was also combined with the same weighted-L_2 norm multiplicative regularizer used in the MR-CSI method, in order to ensure that the comparison between the two methods was fair. With the MR term, we have labeled the algorithm MR-DBIM. Since the MR-DBIM method is not directly a part of this thesis the details are left to [33]. The primary purpose of including these results is to provide a benchmark of another state-of-the-art non-linear inversion algorithm to compare with the MR-CSI algorithm.

4.1 Comparison Results

In order to test the blind inversion capabilities of these algorithms, we present inversion results from three different data sets: synthetic data, 2D experimental scattering data collected by the Fresnel Institute in 2005 [40, 85], and a data set from a MWT system at UPC Barcelona [86, 87]. Each data set has different levels and types of noise, utilizes different background media, and different antenna types and positions (computational point sources, bi-static free-space broad-band antennas in the far field, and co-resident water-submerged narrow-band antennas respectively). This wide range of data provides an excellent cross-section of MWT data types. For the inversions, the only constraints utilized were to keep the permittivity values within physical values (e.g., $Re(\epsilon_r) \geq 1$, and $Im(\epsilon_r) \leq 0$).

Unless otherwise noted, all DBIM reconstructions shown in this section are gener-

ated with the Laplacian regularizer and MR.

4.1.1 Synthetic leg data results

While the ultimate test of any inversion algorithm must involve experimentally collected scattering data, it is very useful for comparison purposes to have a synthetic data set where the exact, 'ideal' contrast is known. Towards this end, we have created a synthetic model of a leg, shown in parts (a) and (b) of Fig. 4.1. Permittivity values for the model were taken from published values on human tissue [88]. The model consists of a bone (comprised of a marrow core, $\epsilon_r = 5.5 - j0.55$ surrounded by cortical bone, $\epsilon_r = 12.6 - j2.4$), inside of a large mass of muscle ($\epsilon_r = 54.8 - j13.0$), surrounded by skin ($\epsilon_r = 39.4 - j12.9$). Data were generated for the model based on a frequency of 1.5 GHz, with 30 transmitters and 30 receivers evenly spaced on a circle of radius 15 cm. The forward solver utilized a grid of 100×100 cells on a 10×10 cm grid. The inversions were performed on a grid of 100×100 cells on a 10.2×10.2 cm grid (thus avoiding the inverse crime, see section 2.5). The 'leg' was immersed in a lossless background medium with $\epsilon_r = 77.3$. To every measurement, 3% noise was artificially added using the formula

$$\tilde{u}_j^{\text{sct}} = u_j^{\text{sct}} + max\left(\left|u_j^{\text{sct}}\right|, \forall u_j^{\text{sct}}\right) N_s(\iota + j\zeta), \tag{4.1}$$

Tab. 4.1: Relative Vector Norms of Synthetic Leg Reconstructions

	MR-CSI Reconstruction	MR-DBIM Reconstruction
L_1 Error	20.3 %	21.1 %
L_2 Error	30.0 %	28.3 %
L_∞ Error	98.9 %	98.9 %

where $N_s = 0.03$ and ι and ζ are zero-mean, uniformly distributed, random numbers between -1 and 1.

The MR-CSI reconstruction is shown in part (c-d) of Fig. 4.1, and the DBIM reconstruction is given in part (e-f). A 1D cross-section of the $y = 0$ line for all three plots is shown in part (g-h). The two reconstructions are remarkably similar, which can be seen particularly clearly in the cross-section plots. Neither algorithm accurately resolves the skin, which is not surprising because the skin is approximately 1.5 mm, or $\approx (1/20)\lambda$, thus showing one of the limits of non-linear imaging algorithms. In the center of the bone, the dielectric constant values obtained by the CSI method are not correct, and the DBIM values are closer to the true values.

As this is a synthetic target, we are able to determine the various L_p norms for the reconstructed images (as compared with the exact image). For this case, the vector norms are given by

$$L_p = \frac{\|\epsilon_{exact}(\mathbf{r}) - \epsilon_{recon}(\mathbf{r})\|_p}{\|\epsilon_{exact}(\mathbf{r})\|_p}, \tag{4.2}$$

where $\epsilon_{recon}(\mathbf{r})$ is the reconstructed permittivity. Due to the fact that forward and

inverse grids are not identical, the discretized versions of (4.2) were calculated by interpolating onto a finer and finer mesh until the norm converged. The L-norms for the various reconstructions of the synthetic leg are shown in Table 4.1. These norms show that the two reconstructions are very close. For the L_1 norm, the MR-CSI reconstruction is better, for the L_2 norm the MR-DBIM reconstruction is better, and they are equal for the L_∞ norm. These data provide some quantifiable confirmation that the reconstructions are of a similar quality.

4.1.2 Fresnel data results

The MR-DBIM and MR-CSI methods were tested on the 2005 Fresnel Data set [40]. These data were collected in free-space over a broad frequency range utilizing double-ridged horn antennas, at a distance of 1.67 meters away from the center of the imaging region. Two antennas and a mechanical positioning system are utilized to collect the data. The scatterers are 2D objects elongated enough in the z-direction so that the objects and fields may be accurately modeled as 2D [40]. To calibrate these data, we utilize the same process outlined in [89]. Calibration methods are discussed further in chapter 7. Here, we present results from the *FoamTwinDiel* and *FoamMetExt* data sets.

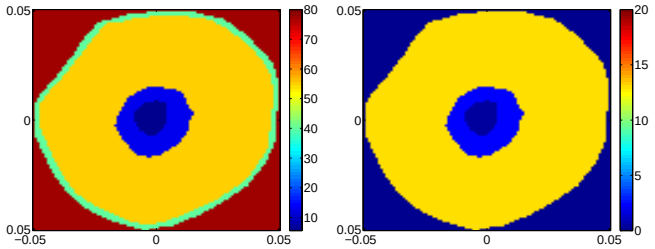

(a) $Re(\epsilon_r)$ Ideal (b) $-Im(\epsilon_r)$ Ideal

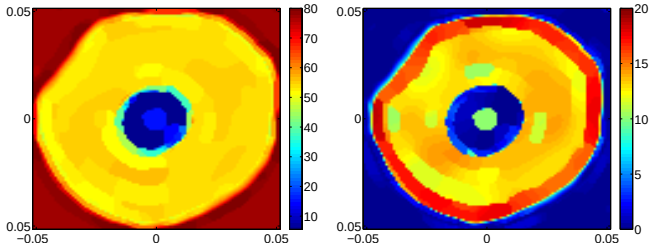

(c) $Re(\epsilon_r)$ MR-CSI (d) $-Im(\epsilon_r)$ MR-CSI

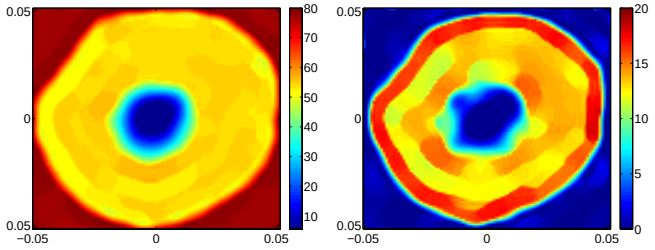

(e) $Re(\epsilon_r)$ MR-DBIM (f) $-Im(\epsilon_r)$ MR-DBIM

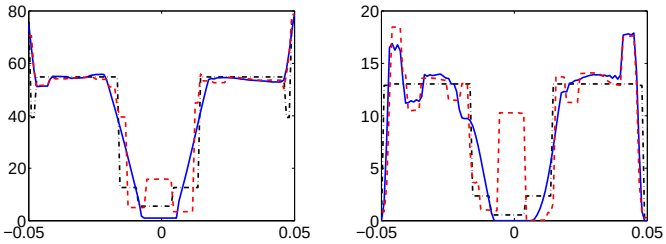

(g) $Re(\epsilon_r)$ Cross-Section (h) $-Im(\epsilon_r)$ Cross-Section

Fig. 4.1: Synthetic leg data set. (a-b) The exact dielectric constant, (c-d) the MR-CSI reconstruction, (e-f) The MR-DBIM reconstruction with Laplacian Regularizer, and (g-h) A 1D cross-section along $y = 0$ of the ideal (black dash-dot line), MR-CSI (red dashed line) and DBIM (blue solid line). The frequency used was $f = 1.5$ GHz. Dimensions are in meters.

FoamTwinDiel

These data were collected for 18 transmitters, 241 receivers per transmitter, and 9 frequencies from 2-10 GHz in 1 GHz steps. The scatterer, shown in part (a) of Fig. 4.2, consists of two smaller cylinders of dielectric constant $\epsilon_r = 3$ where one of the smaller cylinders is embedded in a larger cylinder with $\epsilon_r = 1.45$. As the cylinders are very low loss over the frequency range of interest, we constrain the inversion to $Im(\epsilon_r) = 0$ in this case. When inverting multi-frequency data, we utilize a 'marching-on-frequency' approach for the DBIM method [90]. That is, we invert the data at the lowest frequency, then use the result from that frequency as the first guess for the second frequency (and so on). The MR-CSI utilizes a simultaneous multi-frequency inversion, i.e., the data from all frequencies are utilized simultaneously. We have implemented a simultaneous multi-frequency inversion for the DBIM, but the marching-on-frequency method provides significantly better results, possibly due to the fact that the initial Born approximation used in the DBIM is poor at high frequencies.

Several reconstructions of this object, on a grid of 60×60 cells, are shown in Fig. 4.2. Part (b-c) shows the reconstruction at a single frequency of 2 GHz, (d-e) at a frequency of 6 GHz, and (f-g) the full data reconstruction from 2-10 GHz. In all cases, the reconstructions are quite similar. Overall, the DBIM overshoots the maximum dielectric constant of 3 in all three reconstructions, but otherwise the reconstructions are hard to tell apart.

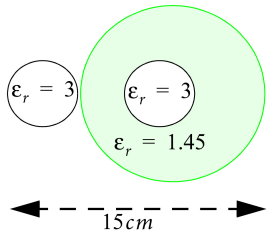

(a) FoamTwinDiel Target

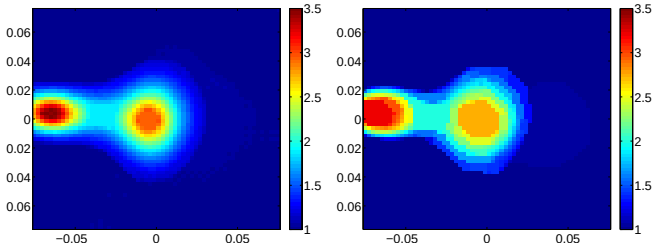

(b) 2 GHz MR-DBIM (c) 2 GHz MR-CSI

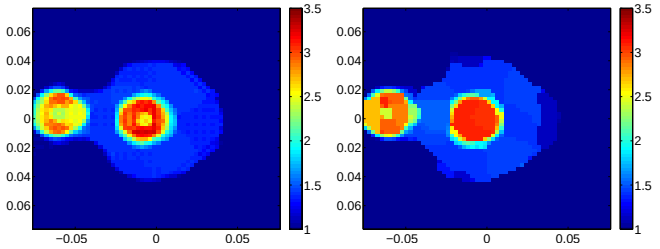

(d) 6 GHz MR-DBIM (e) 6 GHz MR-CSI

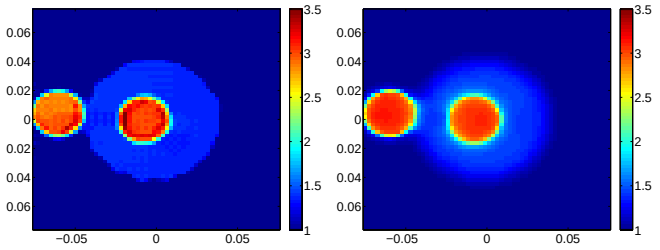

(f) 2-10 GHz MR-DBIM (g) 2-10 GHz MR-CSI

Fig. 4.2: Reconstruction of Fresnel Data Set *FoamTwinDiel*. DBIM with MR and the Laplacian regularizer reconstructions are on the left, and MR-CSI reconstructions are on the right. (a) Schematic of the scattering cylinders, (b-c) Reconstructions at 2GHz, (d-e) Reconstructions at 6 GHz and (f-g) Full-frequency reconstructions 2-10 GHz. Dimensions are in meters.

FoamMetExt

This data set was collected for 18 transmitters, each with 241 receivers, over seventeen 1 GHz steps in the frequency range of 2-18 GHz. The 2D schematic of the scatterers is shown in Fig. 4.3(a). In this case, the scatterers consist of a small (radius of 1.55 cm) cylindrical copper rod, next to a weakly scattering dielectric cylinder of radius 4 cm with $\epsilon_r = 1.45$.

The reconstructions on a grid of 60×60, at a frequency of 6 GHz, are shown in Fig. 4.3. Part (b-c) shows the MR-CSI method and (d-e) the DBIM method. Again for this data set, the reconstructions are very similar. In this case, the MR-CSI method gives some oscillations inside the larger scatterer which the DBIM does not. There are some differences inside the copper cylinder, but as there are no fields inside the cylinder (and thus no information about the inside of the scatterer), these differences are not relevant. The full frequency (2-18 GHz) reconstruction is shown in Fig. 4.4. Part (a-b) shows the MR-CSI reconstruction, while part (c-d) shows the DBIM reconstruction. In this case, the two are very similar, with the only significant differences being inside the copper cylinder.

4.1.3 UPC Barcelona data set

The UPC Barcelona data set [86, 87] was collected from a near-field single frequency scanner, pictured in [91]. There are 64 transmitters, and 33 active receivers for each transmitter (64 total receiver positions). The data were collected at a frequency of

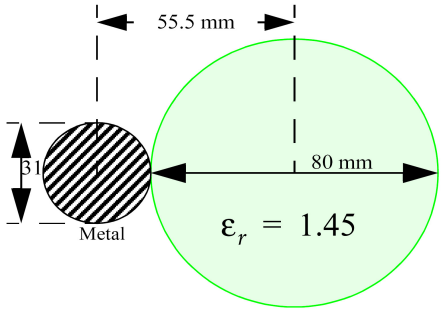

(a) FoamTwinDiel Target

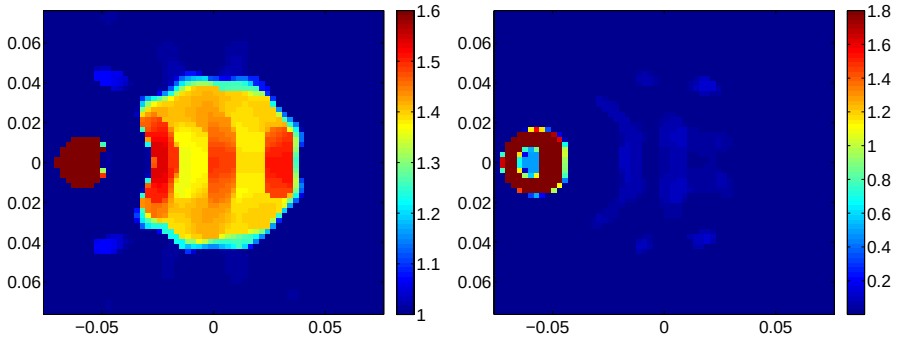

(b) $Re(\epsilon_r)$ MR-CSI 6 GHz

(c) $Im(\epsilon_r)$ MR-CSI 6 GHz

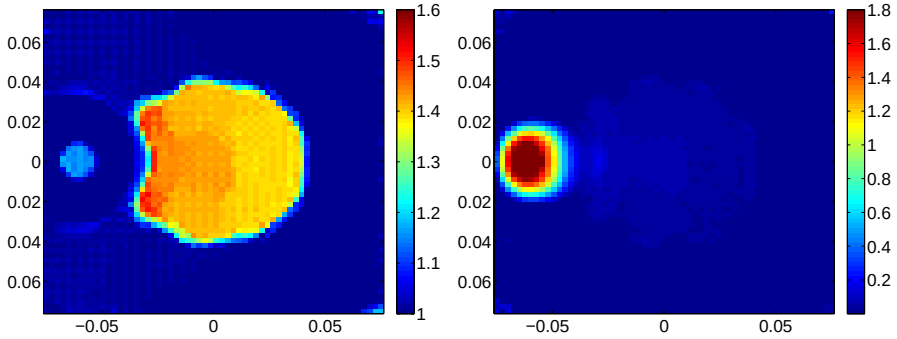

(d) $Re(\epsilon_r)$ MR-DBIM 6 GHz

(e) $Im(\epsilon_r)$ MR-DBIM 6 GHz

Fig. 4.3: Single frequency reconstructions of Fresnel Data set FoamMetExt. (a) Schematic of the scattering cylinders, (b-c) MR-CSI reconstruction at 6GHz, (d-e) DBIM reconstructions at 6 GHz. Dimensions are in meters.

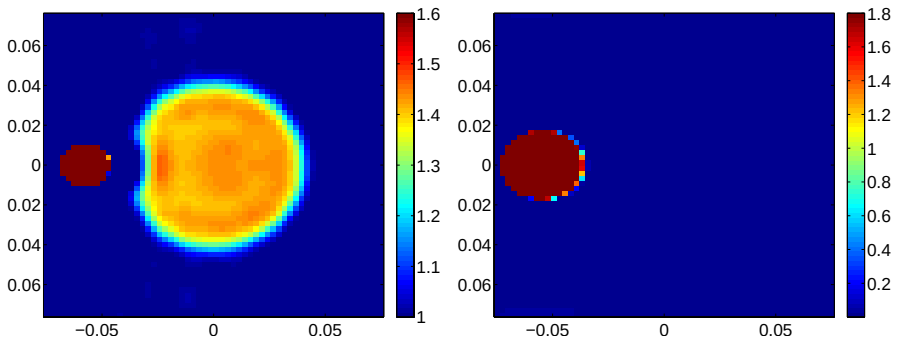

(a) $Re(\epsilon_r)$ MR-CSI 2-18 GHz (b) $Im(\epsilon_r)$ MR-CSI 2-18 GHz

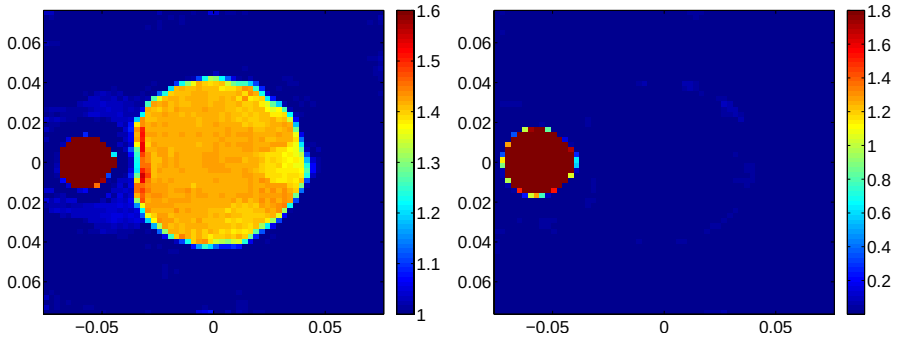

(c) $Re(\epsilon_r)$ MR-DBIM 2-18 GHz (d) $Im(\epsilon_r)$ MR-DBIM 2-18 GHz

Fig. 4.4: Full-Frequency reconstruction of Fresnel Data Set *FoamMetExt*. (a-b) MR-CSI reconstructions from 2-18 GHz data, (b-c) DBIM reconstructions from 2-18 GHz data. In this case, the differences between the images are primarily inside the copper rod, where no fields exist. In order to see the weakly scattering object, all images have been limited to a maximum pixel intensity. Dimensions are in meters.

2.33 GHz. The data collection tank was filled with a background solution of water, with permittivity $\epsilon_b = 77.3 - j8.66$ at 2.33 GHz. We consider two different data sets: a biomedical phantom, FANTCENT and a human forearm, BRAGREG. In all inversions in this section, the results were restricted to lie within $0 \leq Re(\epsilon_r) \leq 80$ and $-20 \leq Im(\epsilon_r) \leq 0$ after each iteration, as the targets do not have permittivities higher than water. For this data set, we do not show the MR-DBIM results, but these are available in [33].

Cylindrical Phantom: FANTCENT

We utilize this data set to display the results from several different types of regularization for both the (MR)-CSI and (MR)-DBIM algorithms. The FANTCENT data set consists of a water and ethyl-alcohol based phantom. A schematic of the phantom (not to scale), with the constituent materials and their dielectric constants, is shown in Fig. 4.5 (a).

The reconstructions for the CSI method are shown in Fig. 4.6. The reconstructions with the DBIM method, and the identity regularizer are shown in Fig. 4.7 (a-b), the DBIM with the Laplacian regularizer in (c-d) and the MR-DBIM (Laplacian regularizer) are shown in (e-f).

Several points may be noted with regards to Figs. 4.6 and 4.7: (i) The CSI algorithm is regularized well enough by the physical regularizer that reasonable results are achieved without the use of MR. However, the use of MR does improve the inversion.

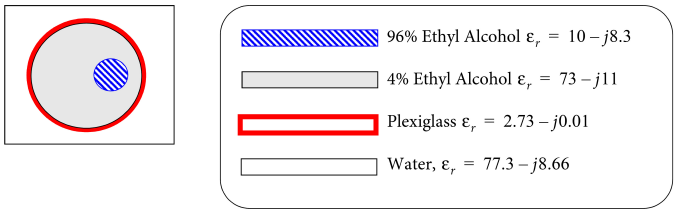

Fig. 4.5: The schematic of the 2D FANTCENT scatterer.

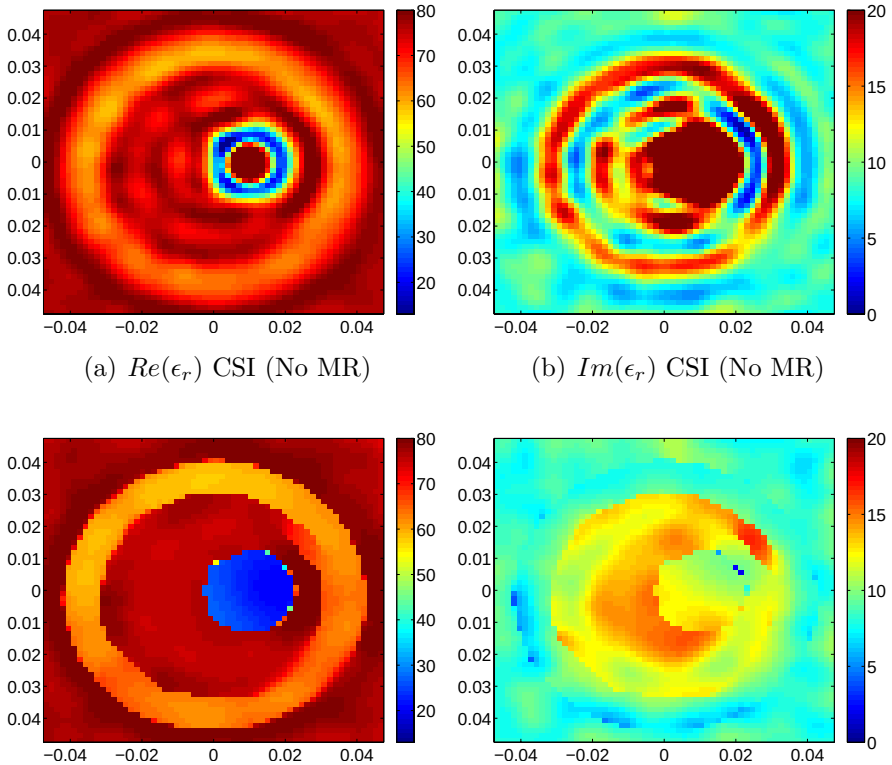

(a) $Re(\epsilon_r)$ CSI (No MR) (b) $Im(\epsilon_r)$ CSI (No MR)

(c) $Re(\epsilon_r)$ MR-CSI (d) $Im(\epsilon_r)$ MR-CSI

Fig. 4.6: Inversion of FANCENT data set: (a-b) The inversion with the CSI method (no MR), (c-d) the results of the MR-CSI method. Dimensions are in meters.

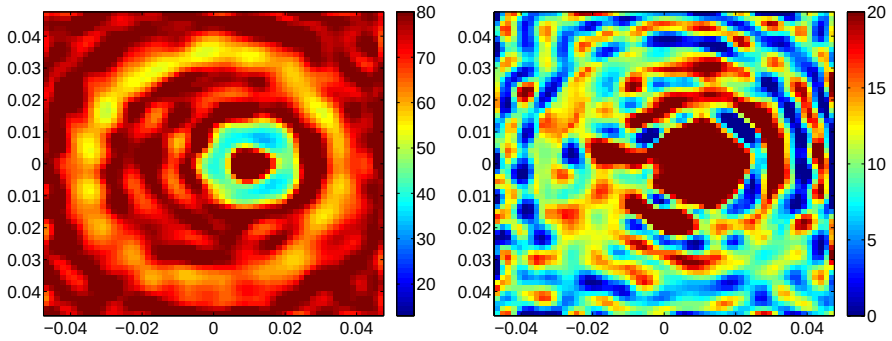

(a) $Re(\epsilon_r)$ DBIM Identity (b) $Im(\epsilon_r)$ DBIM Identity

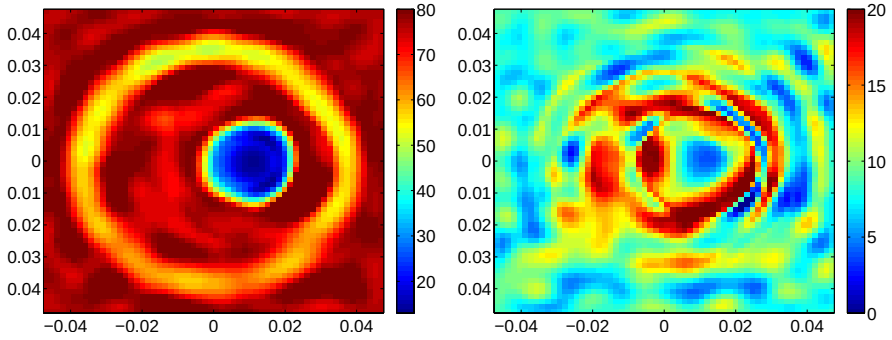

(c) $Re(\epsilon_r)$ DBIM Laplacian (d) $Im(\epsilon_r)$ DBIM Laplacian

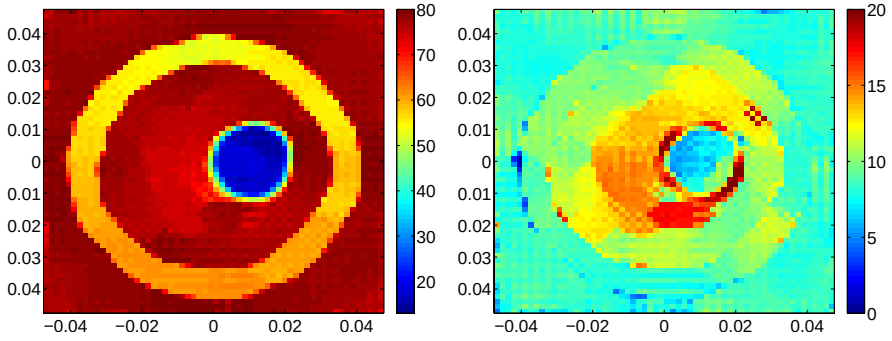

(e) $Re(\epsilon_r)$ MR-DBIM (f) $Im(\epsilon_r)$ MR-DBIM

Fig. 4.7: Inversion of FANCENT data set: (a-b) The results for the DBIM with Identity regularizer, (c-d) DBIM with Laplacian, and (e-f) DBIM with MR and Laplacian regularizers. Qualitatively, the MR-DBIM and MR-CSI reconstructions are quite similar. Dimensions are in meters.

(ii) The basic CSI method is somewhere between the DBIM-identity regularized and DBIM-Laplacian regularized solution. (iii) The MR-DBIM algorithm is quite similar to the MR-CSI algorithm.

It is hard to determine which inversion method provides the better result in this case. Both algorithms do not reconstruct the imaginary part of the dielectric constant very well, although there seems to be fewer oscillations in the MR-CSI reconstruction. However, the DBIM reconstruction obtains a closer result for the dielectric constant of the inner cylinder, particularly for the real part of the dielectric constant, where it reaches a value of $Re(\epsilon_r) = 15$, when the actual value should be $Re(\epsilon_r) = 10$. The MR-CSI algorithm reaches approximately $Re(\epsilon_r) = 20$.

Human Forearm: BRAGREG

The final data set detailed in this chapter is the scattering data taken from a human forearm, data set BRAGREG. The expected relative permittivities at this frequency are approximately $\epsilon_r = 54 - j13$ for muscle, $\epsilon_r = 38.5 - j10$ for skin, $\epsilon_r = 8 - j1$ for bone marrow, and $\epsilon_r = 5.5 - j0.6$ for bone [31, 88].

The reconstruction from the MR-CSI algorithm for this data set is shown in Fig. 4.8 (a-b), and the MR-DBIM inversion is shown in Fig. 4.8. In this case it is difficult to determine which is a better reconstruction, due to the fact that there is no ideal case with which to compare the reconstructions. In both cases, the overall structure of the arm may be seen in both the real and imaginary part of the reconstructions. The

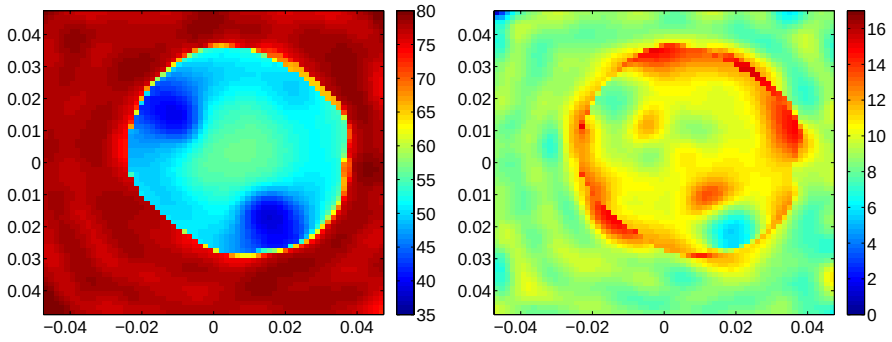

(a) $Re(\epsilon_r)$ MR-CSI (b) $Im(\epsilon_r)$ MR-CSI

(c) $Re(\epsilon_r)$ MR-DBIM (d) $Im(\epsilon_r)$ MR-DBIM

Fig. 4.8: Human forearm inversions: (a-b) Results of the MR-CSI method. (c-d) Results for the DBIM method with MR and Laplacian regularizer after 9 iterations. Dimensions are in meters.

one advantage of the DBIM method is that it reaches closer to the expected value for the real part of the permittivity of the bones. However, we again note that the DBIM reconstruction with the identity regularizer (not shown) did not provide satisfactory results, emphasizing the importance of the Laplacian regularizer.

4.2 Discussion of inversion results

Using an example of each of the two major classes of non-linear inversion techniques, the MR-CSI and DBIM methods, we blindly inverted a wide-range of data sets: noisy synthetic data, free-space far field data, and near-field water-submerged data. These inversion results provide a benchmark of the state-of-the art capabilities of non-linear inversion techniques, and provide an excellent basis for inverting the results from our MWT system.

The primary differences between these two examples of inversion techniques lie not in the inversion results, but rather in implementation issues and computational complexity. The details of the computational complexity comparison are left to [33], but the conclusion is that the computational cost of the two algorithms is very similar. In terms of implementation concerns, the MR-CSI is somewhat easier, primarily because there is no need for the user to select a regularization parameter.

5. THE FINITE-DIFFERENCE CONTRAST SOURCE INVERSION METHOD

The ability to infer information on an object without direct contact also expands man's sensory horizon. No doubt, it is a much sought after capability.
W.C. Chew

All reported biomedical MWT systems use some kind of *matching media* (e.g., [3,67,86]). The matching media is a specially chosen fluid which surrounds the antennas and scatterers. The primary effect of this matching media is to allow the imaging of targets which would otherwise not be possible, by effectively reducing the contrast of the scatterer. The result is that more of the incident wave is transmitted into the scatterer. This allows more energy, which must ultimately carry the information about the scatterer, to enter, interact with, then exit the scatterer. For example, if a scatterer embedded in free-space has high permittivity around its edge (e.g., $\epsilon_r = 80$), then assuming normal incidence of a wave, at this edge only $\approx 20\%$ of the energy will enter the scatterer [38]. If however, a matching media of $\epsilon_r = 60$ is used, $\approx 93\%$ of

[0] The work outlined in this chapter was completed while the author was at Schlumberger-Doll Research, Cambridge, MA, USA.

the energy will get through the boundary. Intuitively, this should lead to improved inversion, as the higher magnitude waves are much more likely to be detectable.

The computational inversion problem is also affected by the use of matching media. Even in the case of noiseless measurement and lossless media, the non-linear problem can be very hard to solve when the scatterer is electrically large and/or has a high contrast. For example, an empirical limit of the electrical size of the object $k_b d\chi = 25$, (where d is the largest dimension of the scatterer) has been suggested for the 3D vectorial MR-CSI method [73]. Another example of large high-contrast scatterers being difficult to reconstruct may be seen in Fig. 6.9. In general, it has been suggested that the convergence of non-linear inversion algorithms is closely related to the norm of the combined Green's function operator (i.e. $\chi G(\mathbf{r}, \mathbf{r}')$) [92], which is reduced through the use of a matching material.

While the use of a matching media has well-known advantages, there is, however, a way to computationally reduce the contrast without a physical matching media. In the data (2.36) and domain (2.37) equations the background wavenumber k_b may be arbitrarily chosen. With a judicious selection of the background wavenumber, i.e., selecting the wavenumber to be as close as possible to the scatterer, the contrast can be computationally reduced, rather than both physically and computationally reduced. However, using non-homogeneous backgrounds requires a Green's function for those backgrounds, and this is easiest to accomplish with a difference based solver. In this chapter, we use a Finite-Difference based solver.

In addition to the ability to computationally reduce the contrast, difference based solvers also have the advantage of readily incorporating other, known, inhomogeneities (such as the non-active antenna elements [93–95]). While this advantage is not dealt with in this chapter, it is discussed in chapter 7.

5.1 Difference based inverse solvers

The most common method of solving the full non-linear inverse wave-field problem, especially with the CSI method, is to utilize the previously described (section 3.5) Integral-Equation (IE) based modeling technique. Other examples of inversion and imaging techniques which utilize IE modeling include [70, 71, 96, 97]. IE techniques are not suitable for a computational reduction of the contrast, as the Green's function for the background medium, $G(\mathbf{r}, \mathbf{r}')$, must be known in a (semi)-analytic form to render the IE approach of practical use. This restricts the background to simple geometric shapes [34, 98]. A way around this problem is to use a differential technique (Finite-Difference or Finite-Element) [1, 7, 99, 100], but to date, these differential inversion methods are all of the conventional type and require the repeated use of a full-forward solver call at each iteration of the inversion algorithm, combined with some other type of problem-specific regularization parameter.

It is possible to modify the MR-CSI technique to use a differential solver to implement the data and domain operators, $\mathcal{G}_{\mathcal{S}}$ and $\mathcal{G}_{\mathcal{D}}$ [36, 74]. The algorithm used for this implementation in our paper [36] is the Finite-Difference technique, and with

this modification of the MR-CSI algorithm, we can capitalize on the advantages of both a differential solver and the CSI technique.

5.1.1 A-priori *information as an initial guess vs. inhomogeneous backgrounds*

In order to computationally reduce the contrast, it is obvious that we must have some kind of information available about the unknown scatterer, e.g., information that the skin forms the outer layer of a biomedical scattering object and/or the average properties of the tissues inside [101]. While 'prior information' is perhaps a better term for this type of information, the MWT and general electromagnetic inversion community have co-opted the term *a priori* information to refer to this type of information. We utilize this nomenclature throughout. *A priori* information is not restricted to surface or average properties: it may come from other imaging modalities such as ultrasound or x-ray computed tomography or it may come from earlier inversions with the same imaging method (this is known as time-lapse imaging). Utilizing multiple imaging modalities may allow the construction of an accurate background model from techniques which have a high resolution, but are not sensitive to a particular pathology (such as x-ray CT), followed by a lower-resolution technique, such as microwave imaging, that is sensitive to the pathology.

While it seems obvious that the use of *a-priori* information in the background wave-number will improve the inversion results overall, for a fair comparison we must also consider the use of this information as an initial guess for the inversion

process. The use of *a-priori* information as an initial guess is readily incorporated into both integral and differential based inversion algorithms. Therefore, throughout this chapter, we always compare the use of *a-priori* knowledge as the background to the inversion with the use of the same information as an initial guess to the (homogeneous background based) inversion algorithm.

5.2 Finite-Difference Implementation of the Data and Domain Operators

To discuss the Finite-Difference implementation of the CSI method we introduce a new domain, T. The new computational domain is shown in Fig. 5.1 and is necessary because our chosen differential operator requires discretization of the entire domain, whereas integral operators require only the discretization of the unknowns (i.e., discretization of the domain D). The Helmholtz equation for the scattered field (2.29) may be written using operator notation as

$$\boldsymbol{\mathcal{H}}_b \left[u_j^{\mathrm{sct}}(\mathbf{r}) \right] = -k_b^2 w_j(\mathbf{r}), \qquad \mathbf{r} \in T. \tag{5.1}$$

The solution of (5.1) may be written as

$$u_j^{\mathrm{sct}}(\mathbf{r}) = \boldsymbol{\mathcal{H}}_b^{-1} \left[-k_b^2 w_j(\mathbf{r}) \right] = \boldsymbol{\mathcal{L}}_b \left[w_j(\mathbf{r}) \right] \qquad \mathbf{r} \in T. \tag{5.2}$$

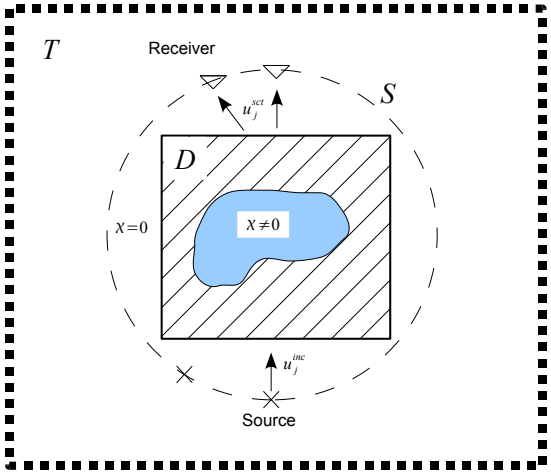

Fig. 5.1: Inverse scattering schematic for the FD-CSI method. The inversion domain D, and measurement domain S, are embedded inside the total computational domain T.

where the operator $\boldsymbol{\mathcal{L}}_b[\cdot]$ is defined as

$$\boldsymbol{\mathcal{L}}_b[\cdot] = \boldsymbol{\mathcal{H}}_b^{-1}\left[-k_b^2(\cdot)\right]. \tag{5.3}$$

Using this notation, we may write the data equation operator as

$$\mathcal{G}_{\mathcal{S}}[\cdot] = \boldsymbol{\mathcal{M}}^S\left(\boldsymbol{\mathcal{L}}_b\left[\cdot\right]\right), \tag{5.4}$$

where $\boldsymbol{\mathcal{M}}^S$ is a characteristic operator which selects the fields at the measurement domain S from the full computational domain T. We may write the domain operator as

$$\mathcal{G}_{\mathcal{D}}[\cdot] = \boldsymbol{\mathcal{M}}^D\left(\boldsymbol{\mathcal{L}}_b\left[\cdot\right]\right), \tag{5.5}$$

where $\boldsymbol{\mathcal{M}}^D$ is a characteristic operator which selects the fields in the inversion domain D from the computational domain T.

With this notation, the CSI objective function becomes

$$F(\chi, w_j) = \frac{\sum_j \left\| \tilde{u}_j^{\mathrm{sct}} - \boldsymbol{\mathcal{M}}^S \left\{ \boldsymbol{\mathcal{L}}_b \left[w_j \right] \right\} \right\|_S^2}{\sum_j \left\| \tilde{u}_j^{\mathrm{sct}} \right\|_S^2} + \frac{\sum_j \left\| \chi u_j^{\mathrm{inc}} - w_j + \chi \boldsymbol{\mathcal{M}}^D \left\{ \boldsymbol{\mathcal{L}}_b \left[w_j \right] \right\} \right\|_D^2}{\sum_j \left\| \chi u_j^{\mathrm{inc}} \right\|_D^2}. \tag{5.6}$$

5.2.1 The FD-CSI method

Once the new operators $\boldsymbol{\mathcal{M}}^D \left\{ \boldsymbol{\mathcal{L}}_b \left[\cdot \right] \right\}$ and $\boldsymbol{\mathcal{M}}^S \left\{ \boldsymbol{\mathcal{L}}_b \left[\cdot \right] \right\}$ have been defined, the FD-CSI method is conceptually identical to the CSI algorithm previously outlined in Chapter 3. The only change required is to replace the operators $\mathcal{G}_{\mathcal{D}}$ and $\mathcal{G}_{\mathcal{D}}$ with their difference based counterparts: $\boldsymbol{\mathcal{M}}^D \left\{ \boldsymbol{\mathcal{L}}_b \left[\cdot \right] \right\}$ and $\boldsymbol{\mathcal{M}}^S \left\{ \boldsymbol{\mathcal{L}}_b \left[\cdot \right] \right\}$.

This change also requires the use of the adjoint operators in their FD domain counterparts. These are given by

$$\begin{aligned} \mathcal{G}_{\mathcal{S}}^* \left[\circ \right] &= \boldsymbol{\mathcal{M}}^{S*} \left(\boldsymbol{\mathcal{L}}_{\mathrm{b}}^* [\cdot] \right) \\ \mathcal{G}_{\mathcal{D}}^* \left[\circ \right] &= \boldsymbol{\mathcal{M}}^{D*} \left(\boldsymbol{\mathcal{L}}_{\mathrm{b}}^* [\cdot] \right) \end{aligned} \tag{5.7}$$

where the operator $\boldsymbol{\mathcal{L}}_{\mathrm{b}}^*$ represents the adjoint of the operator $\boldsymbol{\mathcal{L}}_{\mathrm{b}}$, and is given by

$$\boldsymbol{\mathcal{L}}_{\mathrm{b}}^* [\cdot] = -\overline{k_b^2} \left(\boldsymbol{\mathcal{H}}_b^* \right)^{-1} [\cdot], \tag{5.8}$$

where

$$\boldsymbol{\mathcal{H}}_{\mathrm{b}}^{*}[\cdot] = \left[\nabla^2 + \overline{k_b^2}(\mathbf{r})\right][\cdot]. \tag{5.9}$$

The adjoint operator $\boldsymbol{\mathcal{M}}^{D*}$ simply takes fields from the inversion domain, and maps them into the total domain T. The adjoint operator $\boldsymbol{\mathcal{M}}^{S*}$ takes the fields from the measurement domain S, divides them by the area of the FD cell, and maps them into the total domain T. The division by the area of the cell is required by the definition of the adjoint operator [74]. Neither operator, $\boldsymbol{\mathcal{M}}^{S*}$ nor $\boldsymbol{\mathcal{M}}^{D*}$, conjugates any fields.

Multiplicative Regularization

The FD-CSI method may also utilize the MR term previously outlined in section 3.4.4. As the MR update does not involve the differential/integral operators, the MR update is unchanged from the previously reported MR-CSI method. With the MR term, the difference based method is labeled the FD-MRCSI method.

5.3 Finite Difference Solver and Computational Burden of FD-CSI

The Helmholtz equation is solved via the Finite Difference Frequency Domain (FDFD) method, using a 4th order FD scheme [102], which incorporates Perfectly Matched Layer (PML) boundary conditions[1]. Both fields and materials are collocated on the center of grid points. For the efficiency of the FD-MRCSI algorithm, it is important

[1] The FDFD code was previously developed at Schlumberger-Doll Research by another author [102, 103]

that the operators $\boldsymbol{\mathcal{H}}_b^{-1}$ and $(\boldsymbol{\mathcal{H}}_b^*)^{-1}$ are computed only once, at the beginning of the inversion process. The single initial computation is possible because the operators depend only on the background medium, which does not change throughout the inversion process. These operators are factorized with an efficient LU decomposition of the resultant discretized operator (see [102, 103]). The decomposition is stored, and the matrix system is solved via back-substitution for each call of the $\boldsymbol{\mathcal{H}}_b^{-1}$ and $(\boldsymbol{\mathcal{H}}_b^*)^{-1}$ operators. The decomposition process takes $O(N^{1.5})$ operations. Each back-substitution of the decomposed matrix system scales with $O(N \log N)$.

The solution of the $\boldsymbol{\mathcal{H}}_b^{-1}$ system is required once per iteration of the MR-CSI algorithm, and the solution of the adjoint system, $(\boldsymbol{\mathcal{H}}_b^*)^{-1}$ is required twice per iteration. Once the initial LU decomposition is completed, the scaling of the FD-CSI algorithm is the same as the integral-equation based CSI algorithm: $O(N \log N)$. However, we note that overall, the computational burden for the FD algorithm is larger than for the IE algorithm. This is due to: (i) the additional $O(N^{1.5})$ matrix decomposition, and (ii) the fact that N is larger for the FD based algorithm, because the entire domain, T must be discretized in the FD approach, while only the inversion domain, D, must be discretized in the IE approach.

5.4 Experimental Verification of the Algorithm

We first show that the FD-MRCSI algorithm is capable of inverting experimental data, and we again use the UPC data set (see section 4.1.3).

5.4.1 Cylindrical Phantom: FANTCENT

The cylindrical phantom data has been discussed previously and is shown in Fig. 4.5. For ease of comparison, we show an approximation of the actual relative permittivity of the phantom in Fig.5.2 (a) and (b) (not to scale). The complex dielectric constant reconstruction from FD-MRCSI algorithm is shown in Fig. 5.2(c) and (d). The reconstruction was carried out on a grid of 64×64 cells. The reconstruction of the dielectric constant is quite good, with the boundaries of the cylinders well delineated. However, the exact dielectric constant values are not retrieved, with the inner cylinder reaching a dielectric constant of about $\epsilon_r = 20 - j11$. The results closely match the IE-MRCSI results presented in Fig. 4.6.

5.4.2 Human Forearm: BRAGREG

Next, we consider the reconstruction of scattering data taken from the human forearm data set BRAGREG, which was previously utilized for the IE-CSI method in Chapter 4. The reconstruction of the data after 2,048 iterations of the FD-MRCSI algorithm is shown in Fig. 5.3. The reconstruction was carried out on a grid of 64×64 cells. In this case, the expected (i.e., the values taken from the literature) complex dielectric constants are not retrieved, particularly for the real dielectric constants for the bones. However, the overall structure of the arm is clearly visible. These results again closely match the IE-MRCSI results in Fig. 4.8.

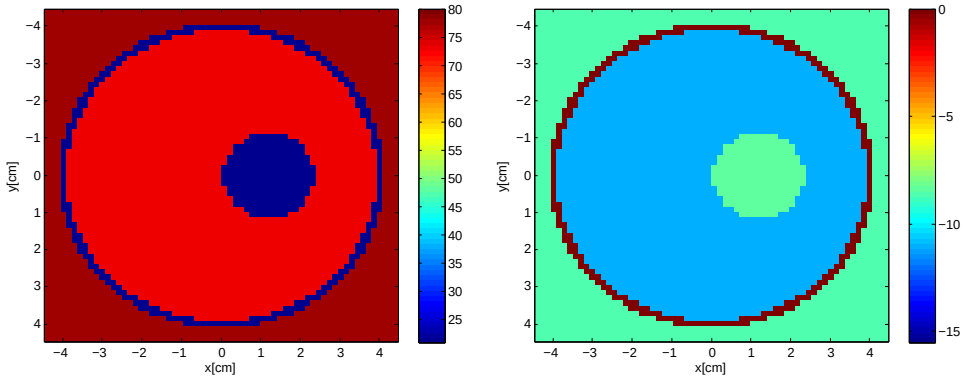

(a) Approx. of Physical $Re(\epsilon_r)$

(b) Approx. of Physical $Im(\epsilon_r)$

(c) Reconstructed $Re(\epsilon_r)$

(d) Reconstructed $Im(\epsilon_r)$

Fig. 5.2: Reconstruction of UPC Cylindrical Phantom data set. The configuration is shown in (a), an approximation of the physical dielectric constant, on the same scale as the reconstruction, is shown in (b) and (c), and the reconstruction with the FD-MRCSI method is shown in (d) and (e).

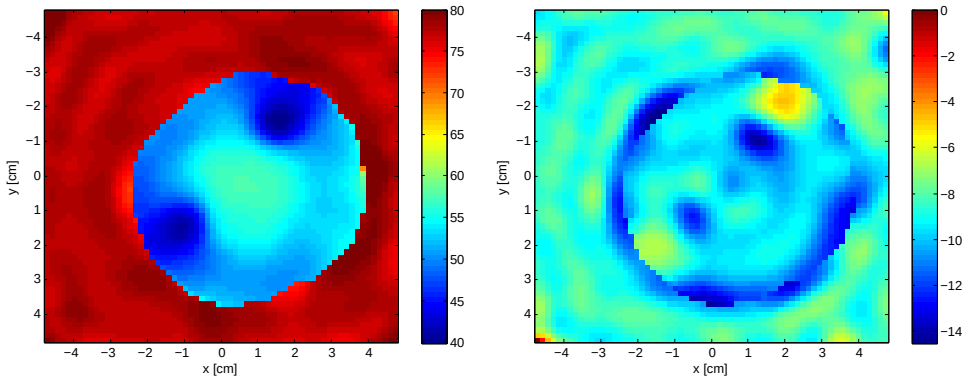

(a) $Re(\epsilon_r)$ (b) $Im(\epsilon_r)$

Fig. 5.3: Reconstruction of UPC Human Forearm data set. The reconstruction with the FD-MRCSI method is shown in (a) and (b).

5.4.3 Use of a-priori *information with experimental data*

In addition to the above results, we inverted the UPC data by utilizing *a priori* information. In the case of these two scatterers, *a priori* information is not directly available (e.g., the exact sizes of the cylinders in the cylindrical phantom data set are not available). Despite this, we have extracted '*a priori*' information from the blind inversion results presented in Figs. 5.2 and 5.3. This was accomplished by performing a visual-based edge extraction, then creating a model with the outline of the blind inversion result, but filled with the average permittivity values taken from inside the cylinder in the blind inversion. This simple model was then used for two cases: (i) as an initial guess for the inversion process, and (ii) as a background model for the inversion.

The resulting inversions were similar or worse compared to the blind inversion.

When the average model was used as an initial guess, the algorithm simply converged to the same result faster (e.g., in the case of the human forearm, in about 1/2 of the iterations). In the case when the average model was used as a background, the algorithm was trapped inside a local minimum, and the results were worse than the blind results. These results clearly point to the importance of utilizing accurate and meaningful *a priori* information.

5.5 Synthetic Results

To show the performance of the FD-MRCSI algorithm when accurate *a priori* information is available, we consider two different computational examples. As a quality indicator, we define the error between the true model and the reconstructed model as follows:

$$E_{\text{model}} = \frac{\|\epsilon_n(\mathbf{r}) - \epsilon_{\text{true}}(\mathbf{r})\|_D}{\|\epsilon_{\text{true}}(\mathbf{r})\|_D}, \tag{5.10}$$

where ϵ_n is the reconstructed complex dielectric constant at iteration n, and ϵ_{true} is the true complex dielectric constant.

To all synthetic experiments, random uniformly distributed noise with maximum amplitude of 0.2% of the maximum value of the magnitude of the total field at the receivers was added to the computed total fields, via the equation

$$u_j = u_j + max\left(|u_j|, \forall u_j\right) N_s(\iota + j\zeta), \tag{5.11}$$

where $Ns = 0.002$ and ι and ζ are uniformly distributed random numbers between -1 and 1. This is equivalent to a signal-to-noise ratio (in the scattered fields) of approximately 18 dB. Noise was added to the total fields (as opposed to the scattered fields) because adding noise to the scattered field would cause the amount of noise to vary significantly depending on the background model used (i.e., when a good estimate of the background is available, the scattered field will be significantly smaller). Thus, to add a noise based on the percentage of the scattered field would bias inversion results towards the cases where a background model is utilized. This amount of noise is equivalent to about 5% noise on the scattered fields when a homogeneous background is assumed. It should be noted that experimental systems measure the total field, so it is more appropriate to add noise to the total field.

5.5.1 Brain Model

As a synthetic example we consider a brain model, where we have added a 'stroke' region to the brain. The model is loosely based on the model outlined in [104], and consists of an outer skin region, followed by bone, cerebral-spinal-fluid (CSF), gray matter and white matter. The two "hemispheres" of the model are separated by CSF. An image of the exact model is shown in Fig. 5.4(a) and (b). The dielectric constants of the model were taken from [88], [105] and are given by $\epsilon_{r,\text{skin}} = 46 - j15$, $\epsilon_{r,\text{bone}} = 12.8 - j2.4$, $\epsilon_{r,\text{gray}} = 52.8 - j16.9$, $\epsilon_{r,\text{white}} = 38.6 - j9.0$ and $\epsilon_{r,\text{CSF}} = 69.3 - j42.8$ at the operating frequency of 1 GHz. The model was embedded in a background with

dielectric constant $\epsilon_r = 45 - j13$. We also included a stroke region in the left side of the brain, consisting of blood, with dielectric constant $\epsilon_{r,\text{blood}} = 61.1 - j28.5$. The brain was illuminated with 32 line sources each with 32 receivers located on a circle of radius 11cm.

As *a priori* information, we created the model shown in Fig. 5.4(c) and (d), which consists of the skin and bone layers, with the interior filled with gray matter. We inverted the data from the brain with the stroke twice, once by utilizing the *a priori* information as an initial guess, and once by utilizing the information as a background around which the model is reconstructed. These two inversion results are shown in Fig. 5.5. The inversion where the information was used as an initial guess achieved an error of $E_{\text{model}} = 14.4\%$, and the inversion where the information was used as a background guess achieved a slightly better result of $E_{\text{model}} = 13.2\%$. Although these two results are quite close, it is of interest that the stroke region is more accurately reconstructed when the background model is utilized.

5.5.2 Time Lapse Brain Reconstruction

Another possible area of application for the FD-MRCSI method is in time-lapse inversion. In this case, we are looking for the differences between a scattering object when the data are collected at two different times. To explore this application, we utilize the same brain model as above both with and without the stroke inclusion. First, a base model is constructed by blindly inverting the brain model without the

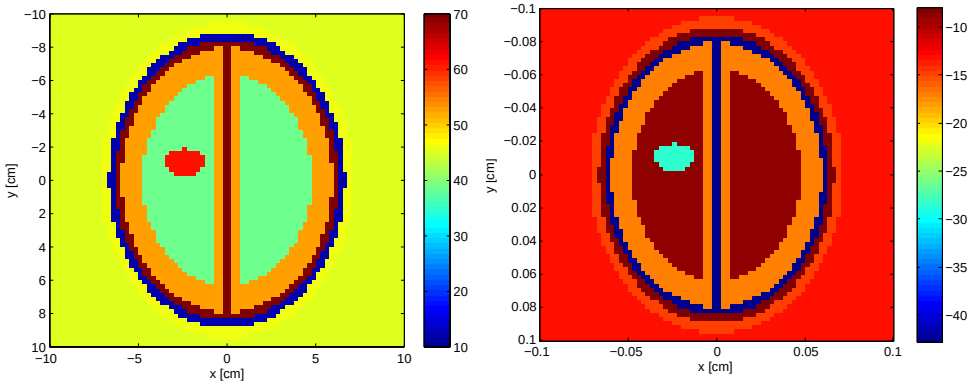

(a) Exact $Re(\epsilon_r)$ (b) Exact $Im(\epsilon_r)$

(c) *a priori* $Re(\epsilon_r)$ (d) *a priori* $Im(\epsilon_r)$

Fig. 5.4: Synthetic Brain Model: the exact model is shown in (a) and (b), and the assumed *a priori* information in (c) and (d).

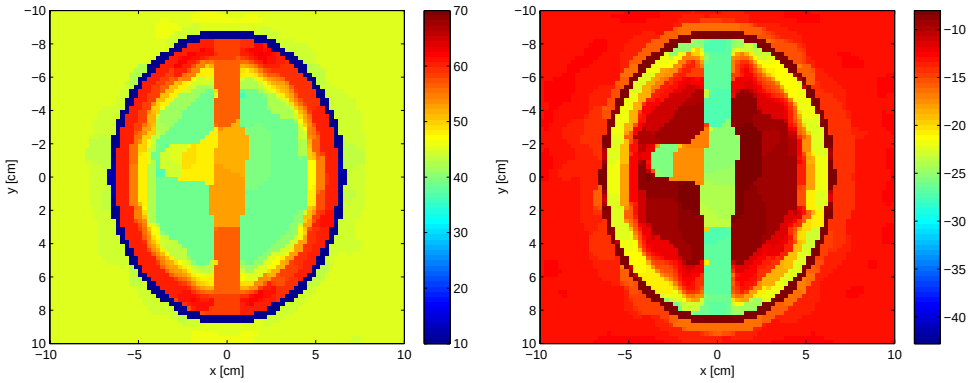

(a) Initial $Re(\epsilon_r)$ (b) Initial $Im(\epsilon_r)$

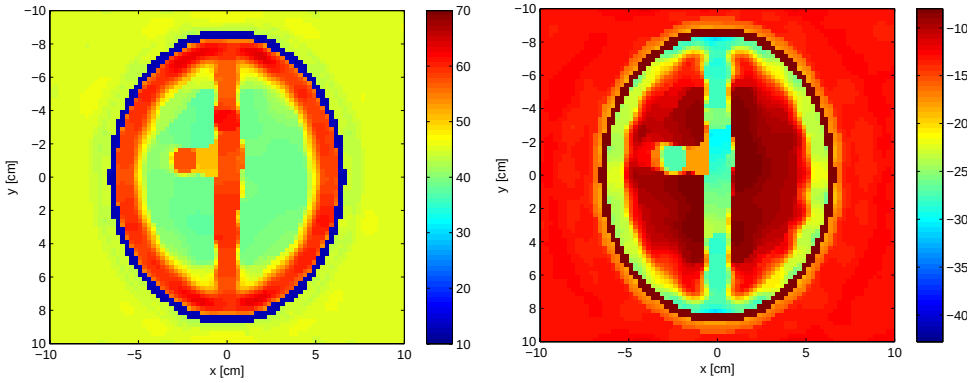

(c) Background $Re(\epsilon_r)$ (d) Background $Im(\epsilon_r)$

Fig. 5.5: Synthetic brain model reconstructions. (a) and (b) show the real and imaginary parts of the FD-MRCSI reconstruction when the *a priori* information is utilized as an initial guess. Parts (c) and (d) show the real and imaginary FD-MRCSI reconstruction when the *a priori* information is used as the background.

stroke. The parameters for the forward field generation and for the inversion were identical to that of the brain model above. The result of the blind inversion is shown in Fig. 5.6(a) and (b) (by blind inversion, we imply that no *a priori* knowledge is utilized in the inversion and we employed a homogeneous background medium).

Next, data were collected with the stroke present in the model, representing data collected at a later time. These data were inverted using the base model both as initial model and as a background model. The results of the initial model inversion are shown in Fig. 5.6(c) and (d), and the inversion results when the base model is utilized as a background are shown in Fig. 5.6(e) and (f). In this example, the images are quite similar, and this is borne out by the errors of the two inversions, with the initial guess case having an error of $E_{\text{model}}^{\text{initial}} = 20.6\%$, and with the background model having an error of $E_{\text{model}}^{\text{back}} = 20.8\%$.

In time-lapse inversion, we are usually concerned with the differences between the earlier and later-time inversions. If we look this difference, shown in Fig. 5.7, it may be argued that the inversion when the base model is used as the background shows the differences (i.e., the stroke) more clearly than the initial case. We do note, however, that the stroke is clearly visible in both sets of difference images. We also note that no *a priori* information was utilized in this time-lapse imaging example.

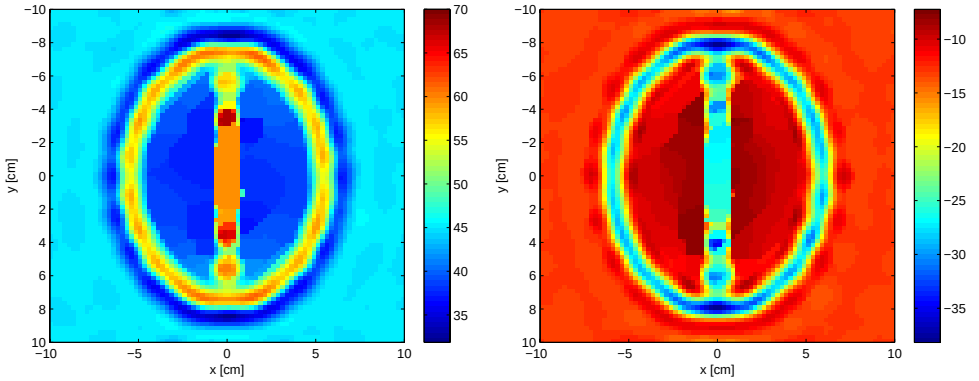

(a) Blind $Re(\epsilon_r)$ (b) Blind $Im(\epsilon_r)$

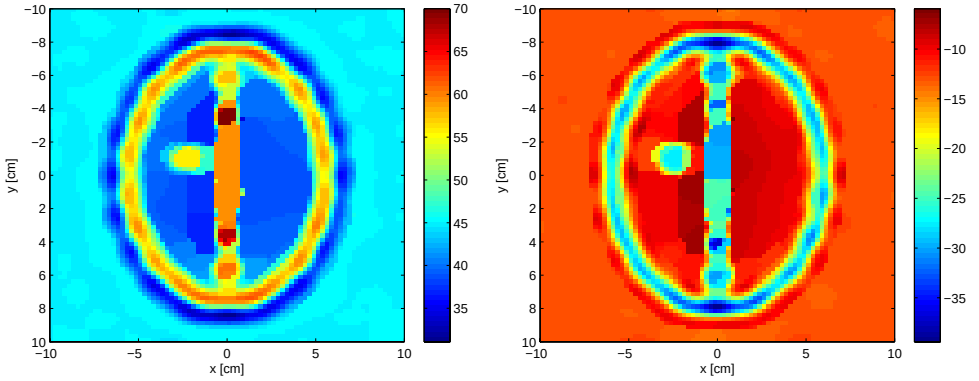

(c) Initial $Re(\epsilon_r)$ (d) Initial $Im(\epsilon_r)$

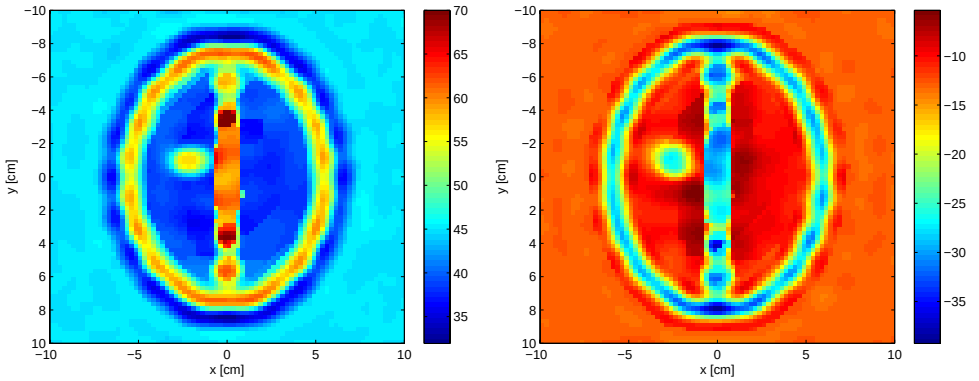

(e) Background $Re(\epsilon_r)$ (f) Background $Im(\epsilon_r)$

Fig. 5.6: Time-lapse inversion example. Parts (a) and (b) show the blind inversion (base model) of the brain model without a stroke. Parts (c) and (d) show the inversion of the brain model with a stroke when the blind inversion is used as an initial guess. Parts (e) and (f) show the inversion of the brain model with a stroke when the blind inversion results are used as a background model.

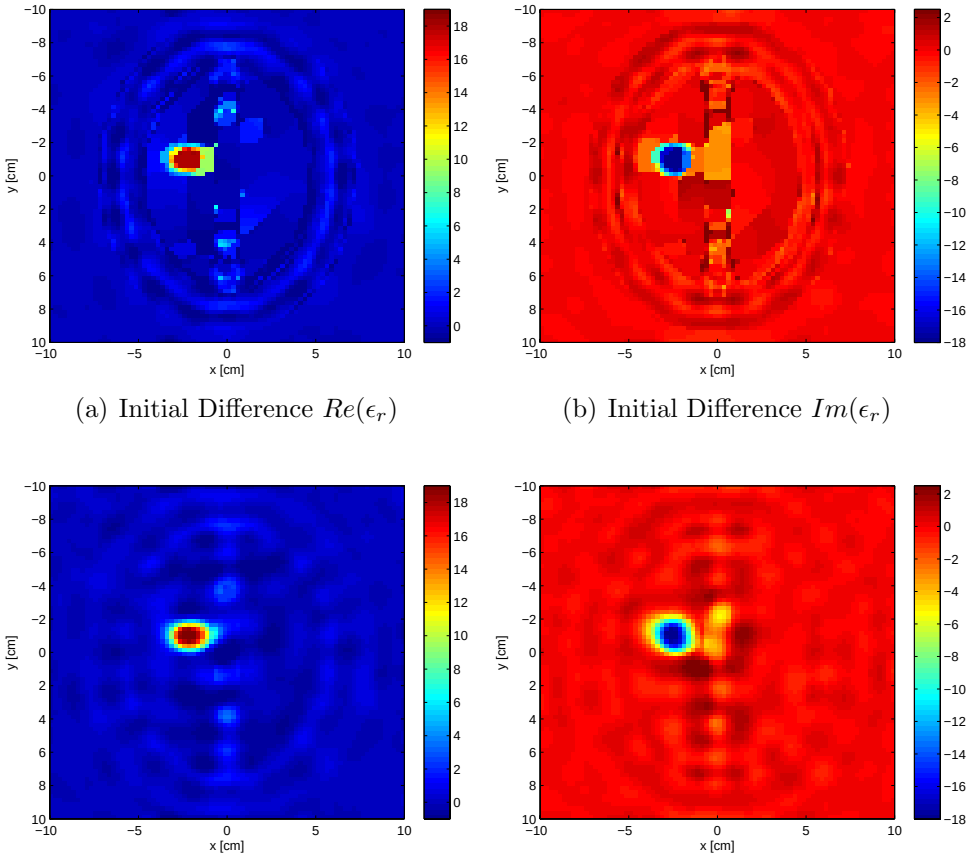

(a) Initial Difference $Re(\epsilon_r)$

(b) Initial Difference $Im(\epsilon_r)$

(c) Back. Difference $Re(\epsilon_r)$

(d) Back. Difference $Im(\epsilon_r)$

Fig. 5.7: Time-lapse difference images. Parts (a) and (b) show the subtraction of the base model from the initial guess inversion. Parts (c) and (d) show the difference between the base model and the background guess inversion. The second case has fewer artifacts.

5.5.3 Breast Model

To test the FD-MRCSI algorithm on a more complex, multi-frequency problem, we consider a breast cancer example. We utilize a 2D breast model taken from a larger 3D model from the University of Wisconsin-Madison breast model repository [106]. The 3D model provides realistic breast tissue values over a broad range of frequencies, based on the studies outlined in [23, 24]. Created from detailed MRI's, the model assigns several different tissue types to regions within the breast. There is further variance of the permittivity values within each tissue type. We utilize the 'mostly fatty phantom #1' model, from which we have selected a single 2D z =constant slice of the full 3D model. The original repository model consists of 0.3 mm pixels, which we decimated to 0.6 mm pixels for more efficient computations. To the basic breast model, we added an elliptically shaped tumor with a major axis of length 1.2 cm, and a minor axis of 0.8 cm. The permittivities for the tumor were taken from the '75th percentile' group from [24].

We simulate the breast model over a frequency range of 2 to 6 GHz in 1 GHz steps. As the permittivities of breast tissues vary significantly over this frequency range, i.e., both the real and imaginary parts of ϵ_r are functions of frequency, we re-calculate the values of the permittivities for the model at each frequency. The model is embedded in a matching medium of oil ($\epsilon = 2.6$), and data are collected at 32 transmitters and 32 receivers. The transmitters and receivers are located on a circle of radius 4 cm. The breast model at a frequency of 6 GHz is shown in Fig. 5.8(a) and (b).

Due to the fact that the permittivity values vary significantly over the frequency range, we treat the inversion of each frequency independently and utilize a marching-on-frequency (MOF) inversion approach [90, 107], as opposed to a simultaneous frequency approach. The simultaneous inversion approach requires a more complicated permittivity model (e.g., a Cole-Cole model), while the MOF approach is capable of utilizing the simple model $\epsilon = \epsilon' + j\epsilon''$, which is valid at each individual frequency. We further utilize the *a priori* information of the skin location (see [18]) and assign the interior of the breast to fatty tissue (50th percentile). The assumed *a priori* knowledge at a frequency of 6 GHz is shown in Fig. 5.8(c) and (d).

We consider two different strategies of MOF inversion: the first is the standard marching-on-frequency approach, which we label the 'initial' model. In this technique we utilize the *a priori* information as an initial guess for the 2 GHz inversion. At the subsequent frequencies, we use the result from the previous frequency as an initial guess. In order to utilize the *a-priori* information as much as possible, we also enforce the skin to the known permittivity values after each frequency. This inversion strategy is amenable to IE inversion techniques. The results from the 'initial model' inversion at 2, 4 and 6 GHz are shown in Fig. 5.9 (not shown are the 3 and 5 GHz results). While the results are reasonable for the 2 GHz inversion, at 4 GHz artifacts begin to appear around the skin of the breast. At 6 GHz, the exterior structure of the breast begins to disappear (particularly in the imaginary part of the permittivity), and many artifacts appear. At 6 GHz, the model error is $E_{\text{model}}^{\text{initial}} = 62.8\%$.

In the second strategy of MOF inversion, labeled the 'background model', we utilize the *a priori* information as the background model for the 2 GHz inversion. At the subsequent frequencies, we utilize the result from the earlier frequency as an initial guess, but we also use the *a priori* information as a background model for each frequency (with the ϵ values of the skin and inner tissue adjusted for the frequency). The inversion results for 2, 4 and 6 GHz are shown in Fig. 5.10. The resultant model error at 6 GHz is $E_{\text{model}}^{\text{back}} = 39.5\%$, a significant improvement over the 'initial' case.

In both inversion cases, the utilization of the result from the previous frequency as an initial guess for the next frequency ignores the dispersive nature of the tissues. However, this error is equivalent for both approaches, and allows for a fair comparison between the two methods.

In the background case, the inversion does not break down at the higher frequencies, and the structure of the breast is clearly visible. As opposed to the 'initial' model, there are no obvious artifacts in the inversion. We also note that the tumor is clearly visible and its dielectric constant is accurately reconstructed despite the fact that the contrast of the tumor is $\chi \approx 20$. We note that while many inversion algorithms will see a 'spike' in the image at contrasts of that magnitude, it is a difficult problem to obtain an accurate dielectric constant at such a high contrast.

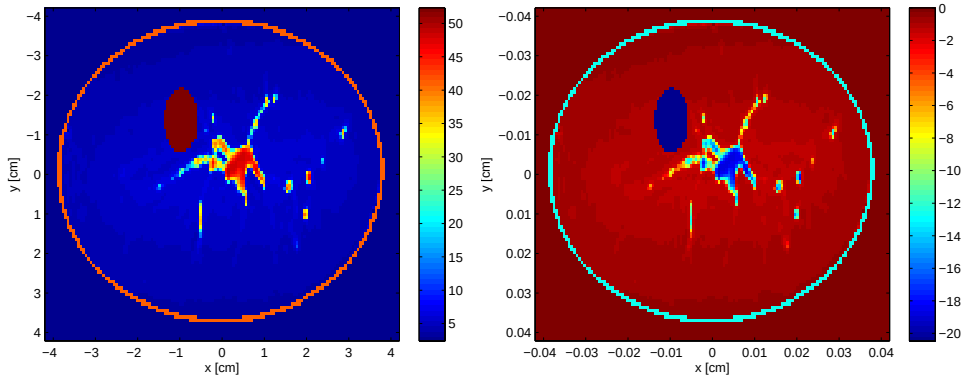

(a) Exact $Re(\epsilon_r)$ 6 GHz (b) Exact $Im(\epsilon_r)$ 6 GHz

(c) *a priori* $Re(\epsilon_r)$ 6 GHz (d) *a priori* $Im(\epsilon_r)$ 6 GHz

Fig. 5.8: Exact breast model at 6 GHz. The exact model is shown in (a) and (b). The assumed *a priori* information is shown in (c) and (d)

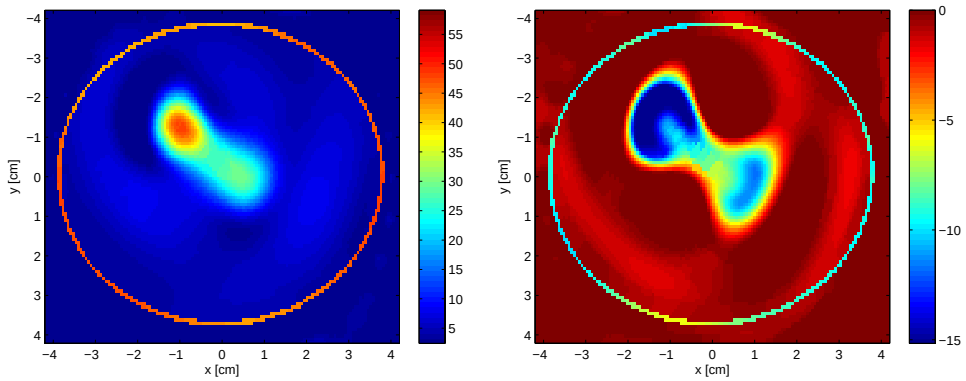

(a) $Re(\epsilon_r)$ 2 GHz

(b) $Im(\epsilon_r)$ 2 GHz

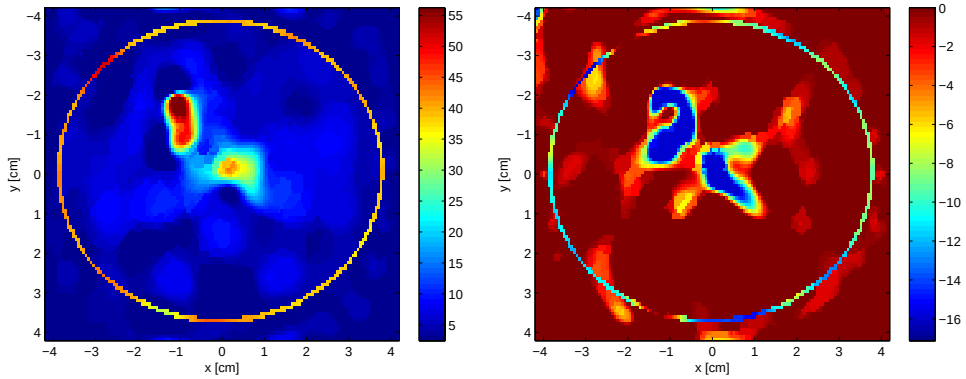

(c) $Re(\epsilon_r)$ 4 GHz

(d) $Im(\epsilon_r)$ 4 GHz

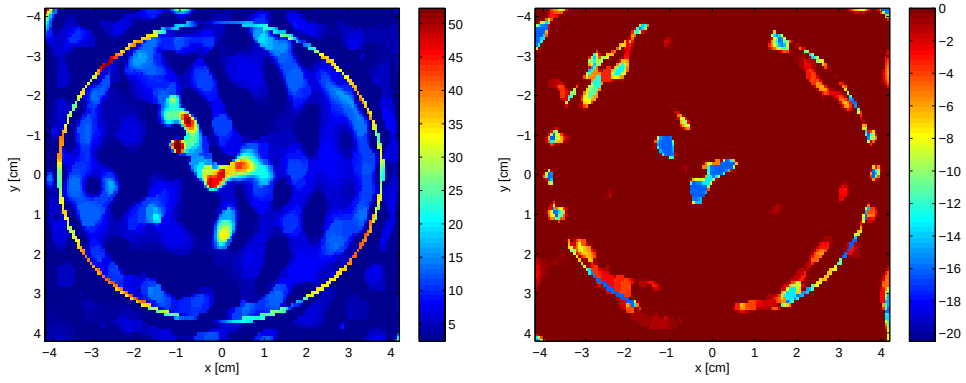

(e) $Re(\epsilon_r)$ 6 GHz

(f) $Im(\epsilon_r)$ 6 GHz

Fig. 5.9: 'Initial model' marching-on-frequency reconstruction of breast model from 2-6 GHz. The reconstructions at 2,4 and 6 GHz are shown.

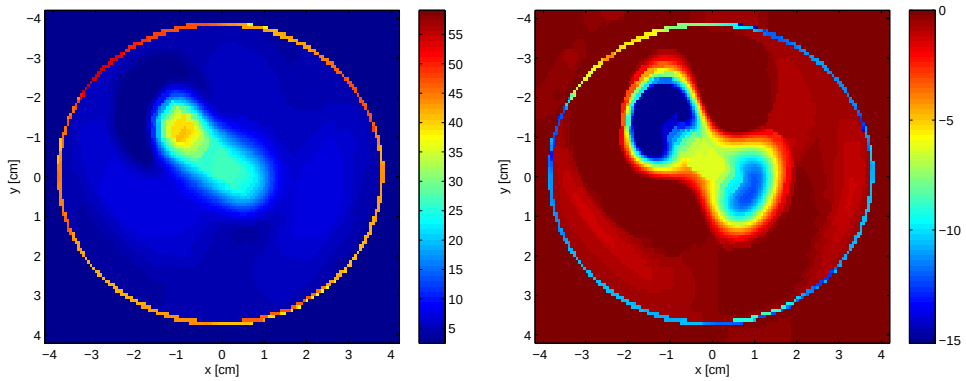

(a) $Re(\epsilon_r)$ 2 GHz

(b) $Im(\epsilon_r)$ 2 GHz

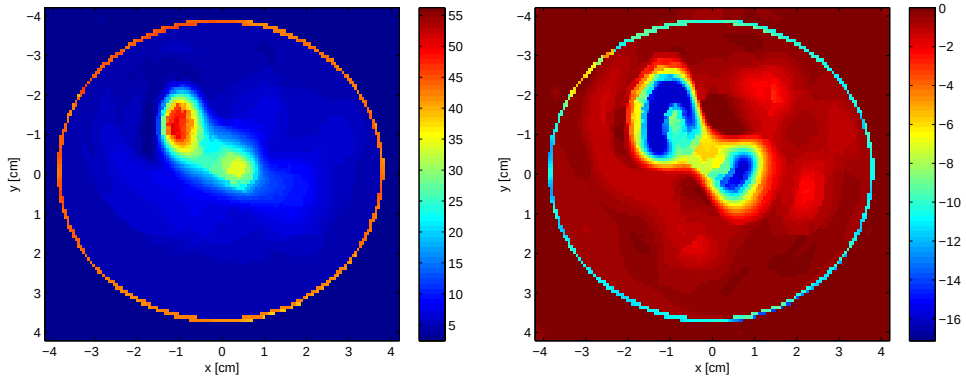

(c) $Re(\epsilon_r)$ 4 GHz

(d) $Im(\epsilon_r)$ 4 GHz

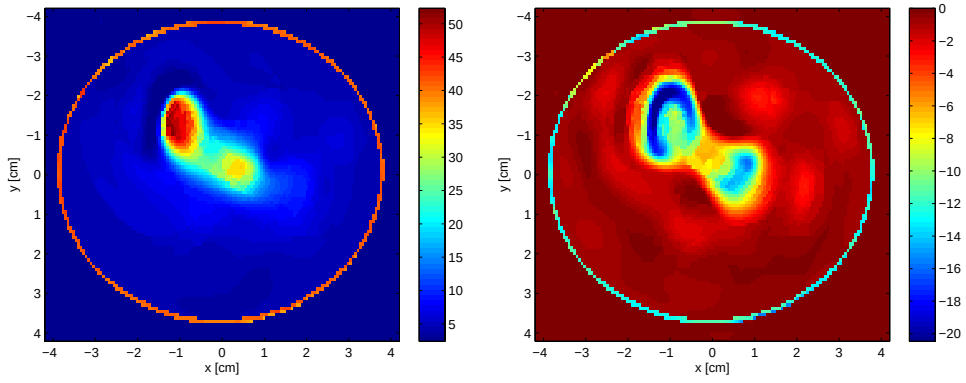

(e) $Re(\epsilon_r)$ 6 GHz

(f) $Im(\epsilon_r)$ 6 GHz

Fig. 5.10: 'Background model' marching-on-frequency reconstruction of breast model from 2-6 GHz. The reconstructions at 2,4 and 6 GHz are shown.

5.6 FD-CSI Conclusions

In this chapter, we have presented an FD-based CSI algorithm which is capable of inverting complex permittivity biomedical data sets. The utility of the algorithm was demonstrated with the inversion of experimentally collected biomedical data sets. The use of an FD-based inversion technique allows the use of complex background models where a Green's function is not readily available.

Through the use of experimental and synthetic examples, we have reached several tentative conclusions regarding the use of *a priori* information in the inversion process. We do note that further study is necessary before these conclusions can be confirmed. (i) When accurate information about the scattering object is available, its use as a background model will improve the inversion result, and is probably preferable over using the *a priori* information as an initial guess for the inversion algorithm. This holds true particularly for high contrast and/or for the multi-frequency case. (ii) It is important that the *a priori* information is accurate, otherwise its use may cause the inversion algorithm to get caught in an undesired local minimum. (iii) When accurate *a priori* information is not available, in time-lapse imaging applications the baseline (earlier-time) model may be used advantageously as a background model.

6. INVERSION INSIDE OF CONDUCTING ENCLOSURES

The book of nature is written in the language of mathematics; without its help it is impossible to comprehend a single word of it.

Galileo

The most common method of collecting biomedical MWT data is to place the unknown scatterer inside an imaging tank filled with a matching fluid. Of necessity, the tank holding the matching fluid is finite in extent. However, the vast majority of imaging algorithms assume that the background is of infinite extent (this was done in the last chapter, even when the background was not homogeneous). This mismatch between the physical situation and model assumptions has the possibility of leading to errors in the reconstruction. At the very least, it effectively adds extra noise to the scattered field data. Consideration of this problem originally lead us to formulate the inverse-scattering problem for an imaging region that is surrounded by a highly-conductive (metallic) boundary.

However, in the course of investigating conducting enclosure MWT systems, it was realized that besides correcting the errors associated with the matching material

[0] The work outlined in this chapter is the subject of a patent application [108].

boundary, there may be other beneficial reasons to consider the use of such systems. Perhaps the most important of these from a practical point of view is that the scattered fields are stronger inside of an enclosure, and the signal-to-noise ratio can expected to be higher [49]. A higher signal-to-noise ratio should lead to higher resolution imaging, and as we believe that the limited resolution is one of the few factors holding back MWT as a technology, this is an important result. There are many other reasons why the enclosed region problem shows great promise, and some of these are outlined herein. The main result of this chapter is to show how the conducting enclosure can be taken into account in MWT.

6.1 Potential advantages to enclosed-region MWT

We have split the potential advantages of enclosed-region Microwave Tomography into two categories: theoretical advantages related to the inverse problem, and practical advantages related to the collection of scattering data. There is some overlap between these two categories, in that some features of enclosed-region MWT affect both theoretical and practical advantages.

The practical potential advantages include:

- Stronger scattered fields are caused by the presence of the conducting boundary [34, 49], and therefore a better signal-to-noise ratio based on the same measurement system may be expected, even in the absence of external noise sources.

- The enclosure provides isolation from outside cables and instruments which degrade the measurement accuracy and perturb the fields inside the imaging domain from what is being assumed in the inversion algorithm.

- The enclosure shields the measurement domain from other sources of interference (e.g., wireless networks and cell phones, etc.).

- As outlined in [34], the conducting enclosure gives the ability to accurately model and monitor the boundary conditions of the problem, which is particularly important for non-lossy matching media.

Although the theoretical advantages associated with the enclosed-region electromagnetic inverse problem are not all clear at the present time, and are area of active research, the following list is probably exhaustive:

- Even if the quantity of information obtainable with a conducting enclosure is not more than that obtainable with an open-region system [49], the resulting optimization problem can have significantly different convergence properties, both in terms of convergence rate as well as to where the algorithm converges (i.e., local/global optima). One reason for this is because the domain of where the search is being performed may be different for the (unknown) field variables. Also, because the Green's function operators are significantly different between the two problems the iterative algorithms will have significantly different performance. For example, even in a simple example such as finding the square-root of two,

different formulations of the associated optimization problem may converge to the correct answer, or not at all [109]. Changes in the Green's could have similar effects to the optimization problem associated with the inverse scattering problem.

- The use of conducting enclosures allows for the possibility of capturing evanescent fields without being in extremely close proximity to the scatterer. This may have advantages for the inversion process, as outlined in [110–112].

- Because the Green's function is ultimately responsible for the sensitivity of the scattered field to permittivity changes inside the scatterer, the modified Green's function resulting from the enclosure can be used to enhance the sensitivity at particular points in the imaging domain.

- The use of several conducting enclosures of different shapes and in conjunction with data obtained from open-region systems may provide further information and regularization of the non-linear inverse problem.

6.1.1 Other Enclosed MWT Research

To the best of our knowledge, our paper [34] was the first paper to consider the possibility that inversion inside conductive-enclosures may improve MWT inversion results. There is, however, another enclosed MWT system which has been considered in the literature [113–115]. These earlier works did not consider the potential advantages

of conductive-enclosed imaging (e.g., in [115] the reflections from the scanner wall are considered 'undesired'). Subsequent to the publication of our paper (the results of which are outlined in this chapter), new experimental results with the enclosed MWT system described in [113] have been published [4, 116], with the some experimental imaging published. Further, an analysis of the inverse source problem via the singular value decomposition of the enclosed Green's operator has been completed [49]. This analysis shows some of the ways that the inverse source problem differs inside a conducting enclosure. In particular, [49] shows that the signal-to-noise ratio is higher in a conductor-enclosed system.

6.1.2 Corrections to Previously Published Results

The results presented in this thesis differ from those presented in [34] upon which this chapter is based. This is due to (i) a coding error which was present in the forward solver associated with the open-region problem used for comparison purposes and (ii) an error in the implementation of the MR term of the CSI method. These errors are noted in [35].

6.2 Derivation of scalar Green's function for cylindrical conductor-enclosed imaging

To implement both a forward solver to generate synthetic data and implement the MR-CSI inversion algorithm we require an appropriate closed-form Green's function

for the enclosed MWT system (for this chapter, we consider only an integral-equation based inversion method). Thus, we seek the solution to the scalar wave equation when the boundary condition is that of a circular Perfect Electric Conductor (PEC) cylinder. Let the surface of the PEC cylinder be denoted by Ω, and the region enclosed by the cylinder as T. The inverse scattering configuration with a conducting cylinder is shown in Fig. 6.1. The Helmholtz equation for this system is given by

$$\nabla^2 u(\mathbf{r},\omega) + k^2(\mathbf{r},\omega)u(\mathbf{r},\omega) = -q(\mathbf{r},\omega), \qquad \mathbf{r} \in T \tag{6.1}$$

where the field quantity $u(\mathbf{r},\omega)$ must also satisfy the boundary condition

$$u(\mathbf{r};\omega) = 0 \qquad \mathbf{r} \in \Omega \tag{6.2}$$

on the surrounding PEC surface.

The Green's function for a homogeneous medium satisfies the equation

$$\nabla^2 G(\mathbf{r},\mathbf{r}') + k^2 G(\mathbf{r},\mathbf{r}') = -\delta(\mathbf{r}-\mathbf{r}') \qquad \mathbf{r} \in T \tag{6.3}$$

Different Green's functions result from the selection of different boundary conditions for $G(\mathbf{r},\mathbf{r}')$. The boundary conditions may be selected to best suit a particular problem.

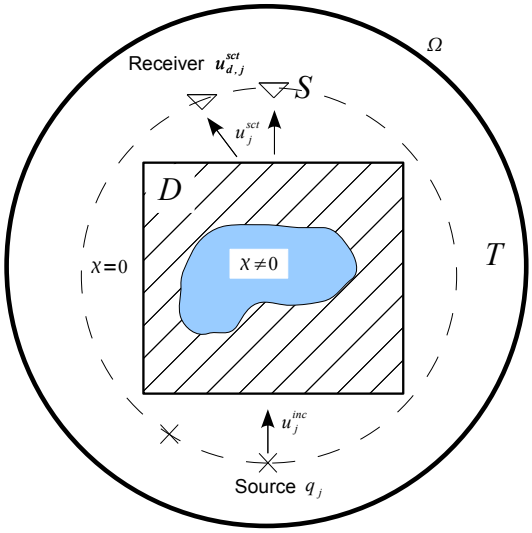

Fig. 6.1: The inverse scattering configuration inside of a conducting cylinder.

By using Green's second identity,

$$\int_T (\phi\nabla^2\psi - \psi\nabla^2\phi)dT = \oint_\Omega \left(\phi\frac{\partial\psi}{\partial n} - \psi\frac{\partial\phi}{\partial n}\right) dS, \tag{6.4}$$

with $\phi := u$ and $\psi := G$ and noting that

$$\begin{aligned} \nabla^2 u(\mathbf{r}) &= -q(\mathbf{r}) - k^2 u(\mathbf{r}) \\ \nabla^2 G(\mathbf{r},\mathbf{r}') &= -\delta(\mathbf{r}-\mathbf{r}') - k^2 G(\mathbf{r},\mathbf{r}') \end{aligned} \tag{6.5}$$

we may write

$$u(\mathbf{r}) = \int_T G(\mathbf{r},\mathbf{r}')q(\mathbf{r}')d\mathbf{r}' - \oint_\Omega \left(u\frac{\partial G}{\partial n} - G\frac{\partial u}{\partial n}\right) d\Omega. \tag{6.6}$$

If this were an open-region problem, we could eliminate the surface integral selecting G to satisfy the Sommerfeld radiation condition. However, with the PEC surface, we remove the surface integral by imposing $G = 0$ on Ω. To construct this G we utilize the Modified Green's function method [117]. We introduce a function, $p(\mathbf{r}, \mathbf{r}')$ which satisfies the homogeneous scalar Helmholtz equation

$$\nabla^2 p(\mathbf{r}, \mathbf{r}') + k^2 p(\mathbf{r}, \mathbf{r}') = 0 \qquad \mathbf{r} \in T, \tag{6.7}$$

and define the Modified Green's function as

$$G(\mathbf{r}, \mathbf{r}') = g_{fs}(\mathbf{r}, \mathbf{r}') + p(\mathbf{r}, \mathbf{r}'), \tag{6.8}$$

where $g_{fs}(\mathbf{r}, \mathbf{r}')$ is the free-space Green's function, i.e., the usual Green's function in the absence of the PEC surface. It may be noted that the addition of the function p makes no contribution to the right hand side of (6.3). Because G satisfies the PEC boundary condition, the boundary condition for p becomes

$$p(\mathbf{r}, \mathbf{r}') = -g_{fs}(\mathbf{r}, \mathbf{r}') \qquad \mathbf{r} \in \Omega. \tag{6.9}$$

Thus the function p satisfies the system

$$\begin{aligned} \nabla^2 p(\mathbf{r},\mathbf{r}') + k^2 p(\mathbf{r},\mathbf{r}') &= 0 \qquad \mathbf{r} \in T \\ p(\mathbf{r},\mathbf{r}') &= -g_{fs}(\mathbf{r},\mathbf{r}') \qquad \mathbf{r} \in \Omega. \end{aligned} \tag{6.10}$$

With this construction, and the assumption that the derivative of the Green's function is finite on the surface Ω, the surface integral in (6.6) is eliminated and we get

$$u(\mathbf{r}) = \int_T G(\mathbf{r},\mathbf{r}')q(\mathbf{r}')d\mathbf{r}'. \tag{6.11}$$

6.2.1 Solution for the Scalar Green's Function

We turn to finding an expression for the function p. The homogeneous differential equation of (6.10) may be solved in a cylindrical coordinate system (r,θ), centered at the origin and using separation of variables [118]. The eigenfunction expansion of p is given by (see Appendix C for the full derivation)

$$p(r,\theta,\mathbf{r}') = \frac{A_0}{\sqrt{2\pi}} J_0(kr) + \sum_{n=1}^{\infty} \left(A_n(\mathbf{r}') J_n(kr) \frac{\cos(n\theta)}{\sqrt{\pi}} + B_n(\mathbf{r}') J_n(kr) \frac{\sin(n\theta)}{\sqrt{\pi}} \right), \tag{6.12}$$

where J_n is the n^{th} order Bessel function of the first kind. The coefficients A_n and B_n are given by

$$A_n(\mathbf{r}') = \frac{-1}{\sqrt{\pi}J_n(ka)} \int_{-\pi}^{\pi} g_{fs}(a,\theta,\mathbf{r}')cos(n\theta)d\theta$$
$$B_n(\mathbf{r}') = \frac{-1}{\sqrt{\pi}J_n(ka)} \int_{-\pi}^{\pi} g_{fs}(a,\theta,\mathbf{r}')\sin(n\theta)d\theta \tag{6.13}$$

where a is the radius of the cylinder. In our case,

$$g_{fs}(\mathbf{r},\mathbf{r}') = \frac{1}{4j}H_0^{(2)}(k\,|\mathbf{r}-\mathbf{r}'|). \tag{6.14}$$

where $H_0^{(2)}$ is the zeroeth order Hankel function of the second kind (note this is the 2D homogeneous space Green's function corresponding to the use of $e^{j\omega t}$ time dependency).

Closed-form expressions for A_n and B_n may be derived (see Appendix C), and are given by

$$A_n = \frac{-\pi}{4j\sqrt{\pi}J_n(ka)}\left[J_n(k\,|\mathbf{r}'|)e^{-jn\phi'}H_n^{(2)}(ka) + J_{-n}(k\,|\mathbf{r}'|)e^{jn\phi'}H_{-n}^{(2)}(ka)\right] \tag{6.15}$$

and

$$B_n = \frac{-\pi}{4\sqrt{\pi}J_n(ka)}\left[J_n(k\,|\mathbf{r}'|)e^{-jn\phi'}H_n^{(2)}(ka) - J_{-n}(k\,|\mathbf{r}'|)e^{jn\phi'}H_{-n}^{(2)}(ka)\right], \tag{6.16}$$

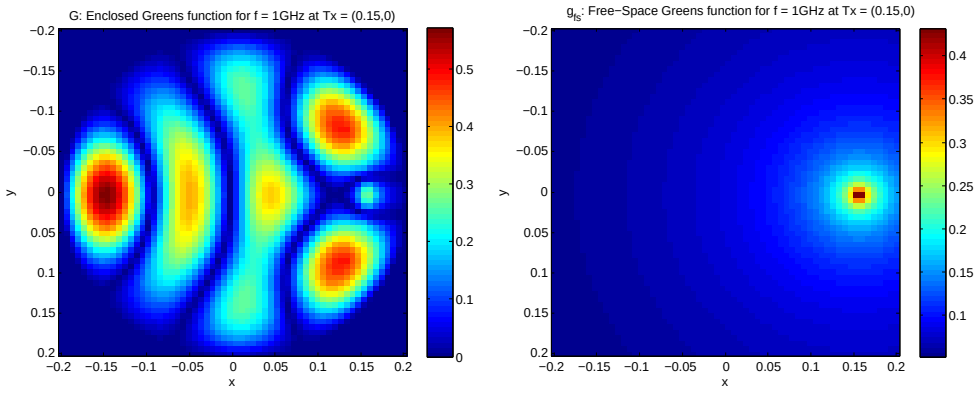

(a) (b)

Fig. 6.2: An example of (a) the conductor-enclosed Green's function vs. (b) the open-region Green's function at 1 GHz. The enclosing cylinder has a radius of 20 cm, and $\epsilon_r = 3$.

where $H_n^{(2)}$ is the n^{th} order Hankel function of the second kind, and ϕ' is the angle associated with the position vector $\mathbf{r}'$. These closed-form expressions significantly reduce computation time for the Green's function.

Figure 6.2 shows a plot of the magnitude of Green's function for a frequency of 1 GHz inside a PEC cylinder of radius 20 cm with a lossless background of $\epsilon_r = 3$. For comparison purposes, the regular free-space Green's function is plotted in the same figure. Note that both Green's functions are singular at the source, but the discretization used in Fig. 6.2 avoids these singularities. However, it is instructive to note how much higher the fields are in the inversion region than for unbounded space, for the same magnitude the current source.

In the context of computational electromagnetics, it is important to eliminate the surface integral in (6.6). The elimination of this integral allows for the application of

standard (frequency-domain) electromagnetic computational techniques, i.e., only a minimal change is required to switch an extant computational code to the new physical situation. In addition, we note that the only singularity of the enclosed-region Green's function, G, is located in the free-space term, $g_{fs}(\mathbf{r}, \mathbf{r}')$. This is due to the fact that p satisfies a homogeneous differential equation. This means that standard methods of extracting singularities in Method of Moments (MoM) codes (e.g., [82, 119]) remain unchanged. This advantage is not a feature of other forms of the Green's function (see for e.g., [120] section 14.6.2). To evaluate integrals of the function p, we may utilize standard quadrature techniques because p is a smooth function.

6.3 Implementation of the Modified Green's function in the MR-CSI

The use of the Modified Green's function in MR-CSI requires little or no changes at the conceptual level. All that is required is the substitution of the modified Green's function in the CSI functional (equation (3.6)). However, the switch in Green's functions does affect the numerical implementation. From a computational perspective, the most important aspects of the PEC Green's function are that (i) it cannot be written in the form $G(\mathbf{r}, \mathbf{r}') = G(\mathbf{r} - \mathbf{r}')$ and (ii) the fields do not decay monotonically as the distance between $\mathbf{r}$ and $\mathbf{r}'$ increases. As these two properties are the core requirements required for the FFT and Fast Multipole acceleration methods respectively, the usual techniques used to make $O(N^2)$ (in memory and computational time) matrix operations into fast $O(N \log N)$ matrix operations are not applicable

to matrices which result from the use of this Green's function. The lack of these two desirable properties is not formulation-dependent, in that they represent the actual physics of EM point sources in a PEC enclosed structure (the existence of standing waves). Thus, a re-formulation of the Green's function which would allow these acceleration methods to be applied is not possible.

Despite these apparent difficulties with the enclosed problem, a solution which does scale as $NlogN$ in computation time is reported in [114], thus the problem is tractable. Further, this N^2 problem may also be solved through the use of a differential solver (our group has done this, see [37, 99]). However, for simplicity, the results in this chapter are generated with all matrix multiplication performed using N^2 algorithms [1].

In practice, the infinite sum in equation (6.12) must be truncated. This is accomplished by taking enough terms in the series until it converges to within some error tolerance. For the examples used in this chapter, given an error tolerance of 10^{-10}, the number of terms was always less than 50.

[1] We have also invested significant effort into the creation of a Finite-Element-Method based version of the CSI method (FEM-CSI). This method is very similar to the FD-CSI method, in that it is a differential based solver that scales with $O(N^{1.5} + NlogN)$, but it has the advantage that curved boundaries may be accurately modeled without a stair-case approximation. In this method, two grids: the triangle-based FEM grid, and the regular inversion grid must be defined. Switching between these grids is done with FEM equivalents of the $\mathcal{M}$ operators (see section 5.2). Unfortunately, it seems that the use of two grids with the FEM-based $\mathcal{M}$ operators interferes with the inversion result. Research is ongoing.

6.4 Sythetic Data Inversion Results

Several different synthetic data sets based on a 2D model have been generated to test the efficacy of the enclosed microwave tomographic method. The incident field for every transmitter was a line-source parallel to the axis of the scatterer, i.e., the incident field was taken to be the Green's function itself. The data were generated with a 2D Method of Moments (MoM) solver using pulse basis functions and point matching.

In order to test the inversion algorithm's performance in the presence of noise, 5% RMS additive uniformly distributed noise was added to all scattered field measurements as follows:

$$\tilde{u}_j^{\text{sct}} = u_j^{\text{sct}} + max\left(\left|u_j^{\text{sct}}\right|, \forall u_j^{\text{sct}}\right) \frac{Ns}{\sqrt{2}}(\iota + j\zeta), \tag{6.17}$$

where ι and ζ are uniformly distributed random numbers between -1 and 1, and Ns is the desired fraction of noise ($Ns = 0.05$ for all examples). For every inversion example, the conditions $Re(\chi) > 0$ and $-Im(\chi) < 0$ were enforced at every step of the MR-CSI algorithm.

For image clarity, all results in Figures 6.3 to 6.9 display the negative of the imaginary part of the contrast, $-Im(\chi) = \epsilon''/\epsilon_b$. Furthermore, for all reconstructions displayed in Figures 6.3 to 6.9, we calculated the L_1, L_2 and L_∞ vector norms based on the exact permittivity, χ_{exact}. The vector norms are normalized by the norm of the

exact contrast, and are discretized versions of the norms for the continuous case:

$$L_p = \frac{\|\chi_{exact}(\mathbf{r}) - \chi_{recon}(\mathbf{r})\|_p}{\|\chi_{exact}(\mathbf{r})\|_p}, \tag{6.18}$$

where $\chi_{recon}(\mathbf{r})$ is the reconstructed contrast. These vector norms are given in Table 6.1. Due to the fact that forward and inverse grids are not identical, the discretized versions of (6.18) were calculated by interpolating onto a finer and finer mesh until the norm converged.

6.4.1 Square Scatterer

For the first numerical example, we consider a simple scenario consisting of a square lossy scatterer. The operating frequency is 1 GHz, and the scatterer is embedded in a PEC cylinder of radius 20 cm. The lossless background has a permittivity of $\epsilon_b = 3$. This low value of relative permittivity was chosen to avoid excessively small wavelengths which overburden the $O(N^2)$ computations. The scatterer is illuminated by 10 transmitters located evenly on a circle of radius 15 cm. The scattered field is measured at 40 receiver points placed on a circle of radius 16 cm. The inversion region D is a square with edges of 20 cm length located in the centre of the PEC cylinder. The scatterer consists of a square object with sides of length 10 cm and a contrast of $\chi = 2.0 - j1.0$. Thus, the object has edges slightly larger than 0.5 λ (with respect to the background). The exact contrast is shown in parts (a-b) of

Figure 6.3. The forward data were generated on a grid of 30 $\times$ 30 placed over D. In order to avoid the inverse crime, the inversion grid was selected to be 29 $\times$ 29 cells. The inversion results after 1024 iterations of the MR-CSI algorithm with the enclosed (PEC bounded) Green's function are shown in parts (c-d) of Figure 6.3.

The reconstruction results show a good, but not perfect reconstruction of the object. The overall shape of the scatterer is clearly visible, and the magnitude of both the real and imaginary parts of the contrast are close to the exact values (within 10%). However, the edges of the object are slightly blurred, which is not unexpected given difference between the forward and inversion grids, and the real part of the reconstruction overshoots the exact value of 2.0.

For comparison purposes, new data were generated for the equivalent unbounded problem: all input parameters for the forward solver were kept the same, except the PEC cylinder was removed, i.e., the regular unbounded-space Green's function was used. Thus, the target was embedded in an infinite medium filled with the background permittivity of $\epsilon_b = 3$. The forward data were then inverted with the MR-CSI method using the regular unbounded-space Green's function. This reconstruction is shown in parts (e-f) of Figure 6.3. The inversion result is quite close to the inversion result from the enclosed case, with slightly less overshoot in the real part of the reconstruction, and more overshoot in the imaginary part of the reconstruction.

For further clarity, one-dimensional cross-sections of the two reconstructions are shown in Figure 6.4. The value of the MR-CSI objective function, $C(w, \chi)$, for these

two reconstructions is shown in part (a) of Figure 6.11. The objective function is lower when the PEC cylinder is present. However, as shown in Table 6.1 the L_1 and L_2 vector norms are slightly better for the open-region problem. The L_∞ norm is better for the enclosed reconstruction.

6.4.2 Concentric Squares

Low Contrast Concentric Squares

Next, we consider the same scattering object that has often been used as a test case for the MR-CSI method [58, 64, 78]. The scatterer consists of two concentric squares, with an inner square having sides of length λ (with respect to the background), with a contrast of $\chi = 0.6 - j0.2$, embedded in an exterior square having sides of 2λ and contrast $\chi = 0.3 - j0.4$. The exact contrast profile is shown in parts (a-b) of Figure 6.5. The imaging region D consists of a square having sides of length 3λ. A single frequency of 1 GHz was utilized, and free-space was assumed for the background. The forward data were generated on a grid of 31 $\times$ 31. Thirty (30) transmitters were spaced evenly on a circle of radius $2.33\lambda = 70$ cm, and 40 receivers were placed evenly on a circle of radius $2.17\lambda = 65$ cm. The scatterer was surrounded by a PEC cylinder of radius 90 cm or approximately 3λ.

The data were inverted via the MR-CSI algorithm with the bounded Green's function. The inversion mesh was selected to have 29 $\times$ 29 elements. The reconstruction after 1024 iterations of the MR-CSI algorithm is shown in parts (c-d) of Figure 6.5.

The reconstruction is very close to the exact contrast, but with a few spurious pixels.

Again, the forward data were re-generated for the case where no PEC cylinder was present, but keeping every other parameter of the forward solver the same. These unbounded free-space data were inverted via the MR-CSI algorithm with the unbounded Green's function, and the results are shown in parts (e-f) of Figure 6.5. One-dimensional cross-section results are shown in parts (a-b) of Figure 6.6. The MR-CSI objective function vs. iteration number is shown in part (b) of Figure 6.11. The three vector norms of the reconstructions are also given in Table 6.1.

In this case, the reconstruction results are ambiguous as to which result is better. Considering the vector norms, the L_1 is better for the enclosed case, while the L_2 and L_∞ are better for the open-region case. From the center of the square in the imaginary part of the contrast it may be argued that the inversion result from the enclosed case is better, where the enclosed reconstruction is within 5% and the open-field reconstruction has an error of over 50% (as seen from the 2D cross section plot). However, both reconstructions provide reasonable results, in that the overall structure of the scatterer is visible.

Mid Contrast Concentric Squares

The concentric square example was run again, but this time with a higher contrast scatterer, with a contrast of 150% of the previous example for both inner and outer squares. With this, the inner square now has a contrast of $\chi = 0.9 - j0.3$, and the

outer square has a contrast of $\chi = 0.45 - j0.6$. Both the bounded Green's function and unbounded forward solvers were run again, and the data were inverted via the appropriate MR-CSI program. All computational parameters were unchanged from the previous concentric squares case.

The reconstruction results are shown in Figure 6.7, the cross sectional plots in Figure 6.8 the MR-CSI objective functions in part (c) of Figure 6.11, and the vector-norm errors in Table 6.1. The results are very close for all metrics. Both algorithms resolve the two squares (in that concentric squares are clearly visible). However, once again, in the interior of the square the enclosed inversion is improved over the open-region case.

6.4.3 High-Contrast Multi-Frequency Concentric Squares

A high-contrast scatterer was created which consists of two concentric squares with the inner square having sides of length 6 cm, and the outer square having sides of length 10 cm. The contrast for the inner cylinder is given by $\chi = 3.6 - j0.2$ at a frequency of 0.5 GHz, and the outer square has a contrast of $\chi = 2.0 - j0.1$ (also at 0.5 GHz). The scatterer was embedded in a background medium with permittivity of $\epsilon_b = 3$. The object was illuminated by 12 sources, placed on a square centered at the origin with sides of 15 cm, at frequencies of 0.5, 1, and 2 GHz. Thus, at the lowest frequency, the scatterer had dimensions of $L \approx 0.29\lambda$, and at the highest frequency, $L \approx 1.15\lambda$. Forty (40) receivers were utilized on a circle of radius 16 cm. For the forward solver,

the scatterer was discretized into 45 $\times$ 45 cells, and for the inverse solver, a grid of 47 $\times$ 47 was utilized. For the first experiment, the scatterer was surrounded by a PEC surface of radius 20 cm. For the second, the scatterer was embedded in an infinite homogeneous background medium.

The reconstructions of the contrast are shown in Figure 6.9, the cross-section plots in Figure 6.10, the MR-CSI objective function is shown in part (d) of Figure 6.11, and the vector-norm errors for the reconstructions are given in Table 6.1. Both reconstructions fail for the imaginary part the contrast (by this we mean the structure of the object cannot be determined by looking at the imaginary part of the reconstruction). The L metrics are very similar for the two cases.

Tab. 6.1: Relative Vector Norms of Reconstructed Contrast Functions

	Recon. with PEC enclosure	Recon. without PEC enclosure
Simple Squares (Fig. 6.3)		
L_1 Error	27.3 %	18.3 %
L_2 Error	26.5 %	19.4 %
L_∞ Error	63.2 %	75.3 %
Low contrast concentric squares (Fig. 6.5)		
L_1 Error	15.4 %	16.1 %
L_2 Error	17.8 %	17.1 %
L_∞ Error	72.0 %	56.4 %
Mid contrast concentric squares (Fig. 6.7)		
L_1 Error	20.0 %	19.9 %
L_2 Error	22.3 %	22.0 %
L_∞ Error	53.3 %	48.0 %
Multi-frequency concentric squares (Fig. 6.9)		
L_1 Error	48.8 %	45.8 %
L_2 Error	51.9 %	51.8 %
L_∞ Error	55.5 %	55.5 %

6.5 Discussion of the results

These results are inconclusive as to the possible benefits of the inversion inside of conducting enclosures. In terms of the practical benefits of the enclosed-region for the synthetic examples shown, we emphasize that for these examples, the signal-to-noise ratio was the same for both enclosed and open-region systems (this is not the case in physical systems), and the examples were arbitrarily chosen. Even in this case, for the concentric square objects (Figures 6.5 and 6.7) the interior of the objects are better reconstructed inside of the PEC (particularly for the imaginary part of the contrast). As the interior regions of scatterers are typically the regions of the highest interest in

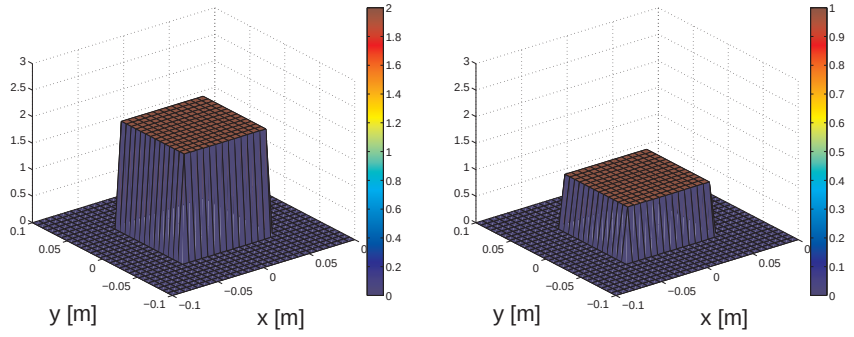

(a) Exact $Re(\chi)$ (b) Exact $Im(\chi)$

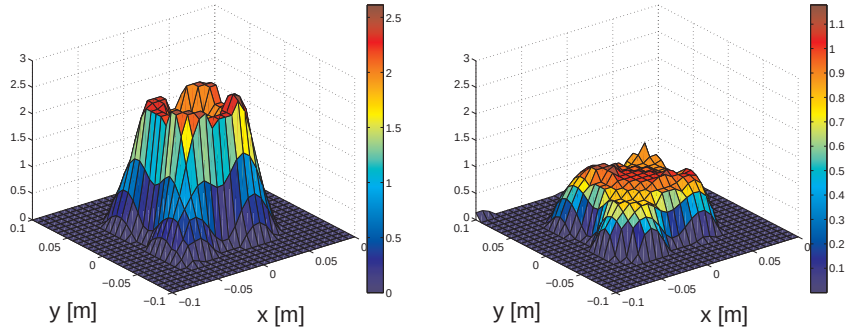

(c) Enclosed $Re(\chi)$ (d) Enclosed $Im(\chi)$

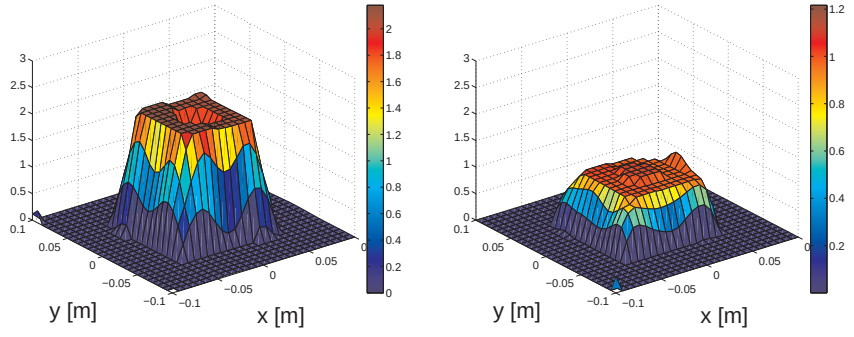

(e) Open $Re(\chi)$ (f) Open $Im(\chi)$

Fig. 6.3: Square Scatterer Reconstruction after 1024 steps of the MR-CSI algorithm. (a-b) The exact contrast of the scatterer. (c-d) The MR-CSI reconstruction when the both forward data generation and inversion include a circular PEC enclosure. (e-f) Reconstruction when both the forward data generation and inversion assume an open-region background.

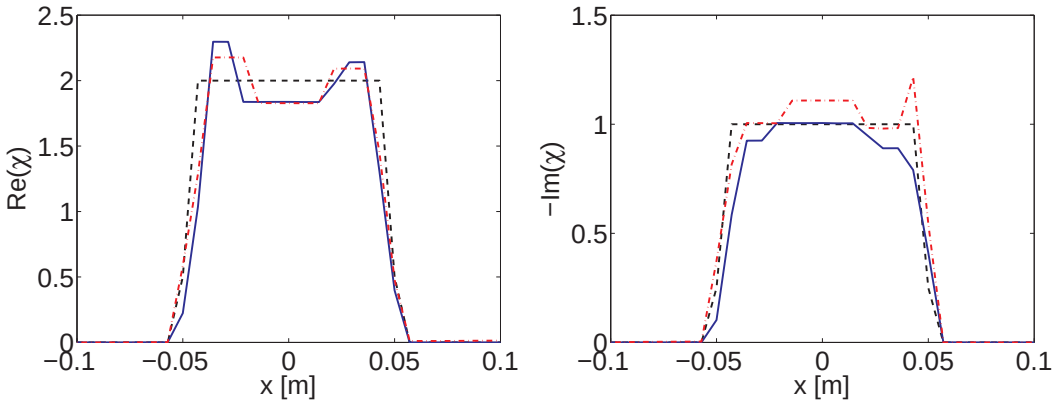

(a) $Re(\chi)$ (b) $Im(\chi)$

Fig. 6.4: Cross-section of square scatterer reconstructions. (a-b) shows a 1D cross section at $y = 0$ for the exact (black dash line), conductor-enclosed (blue solid line), and open-region (red dash-dot) reconstructions for the square scatterer shown in Fig. 6.3.

MWT, this is a positive sign.

Investigation of the other possible benefits of conductor-enclosed imaging still needs significant research. As noted above, another group [49] has considered the linear (inverse scattering) problem by analyzing the SVD of the Green's function operator. Their conclusion is that the enclosure does not add quantitative information to the linear problem (in the sense that no larger number of singular values may be retrieved), but that the 'quality' of the information may be different. By this, it seems that they mean that the particular singular values which are retrievable do not represent the same data as the open-region problem, and different reconstructions may be better for different cases. The results of this chapter support this conclusion.

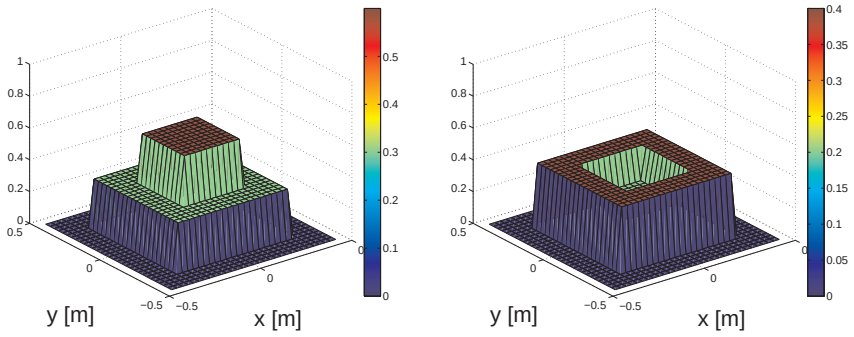

(a) Exact $Re(\chi)$ (b) Exact $Im(\chi)$

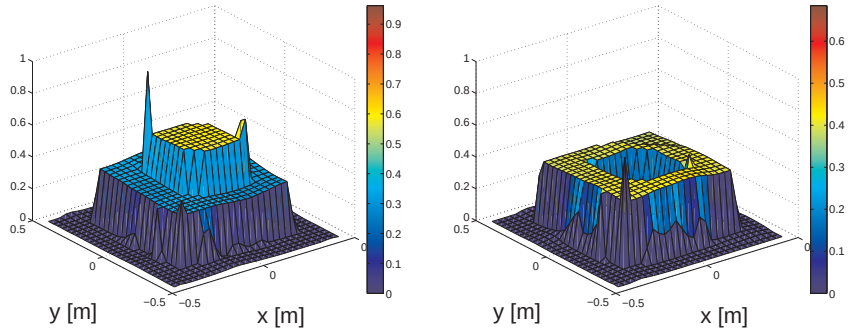

(c) Enclosed $Re(\chi)$ (d) Enclosed $Im(\chi)$

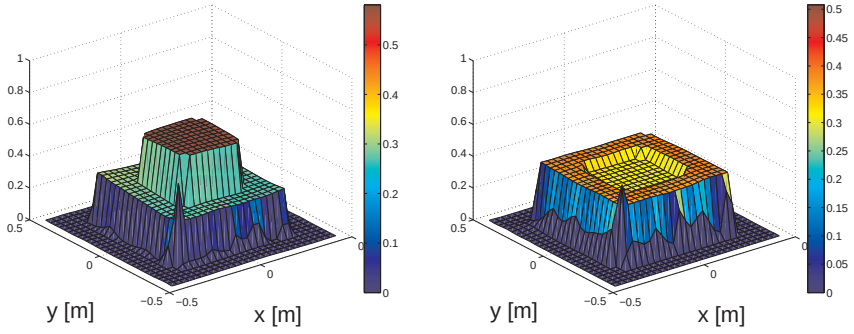

(e) Open $Re(\chi)$ (f) Open $Im(\chi)$

Fig. 6.5: Low Contrast Concentric Squares after 1024 steps of the MR-CSI algorithm. (a-b) The exact contrast of the scatterer. (c-d) The MR-CSI reconstruction when the both forward data generation and inversion include a circular PEC enclosure.. (e-f) Reconstruction when both the forward data generation and inversion assume an open-region background. (d) A 1D cross section at $y = 0$ for exact (black dash line), conductor-enclosed (blue solid line), and open-region (red dash-dot) reconstructions.

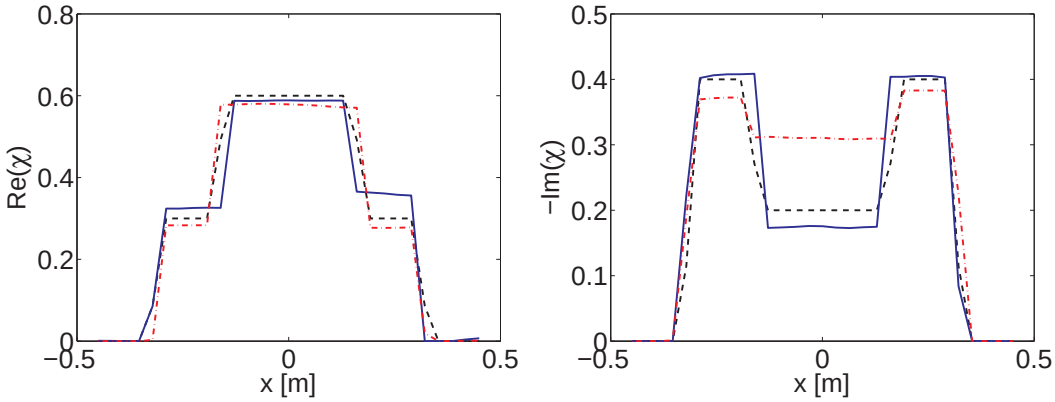

(a) $Re(\chi)$ (b) $Im(\chi)$

Fig. 6.6: Cross-Section of the Low Contrast Concentric Square Scatterer. (a-b) A 1D cross section at $y = 0$ for exact (black dash line), conductor-enclosed (blue solid line), and open-region (red dash-dot) reconstructions, for the low contrast concentric square scatterer.

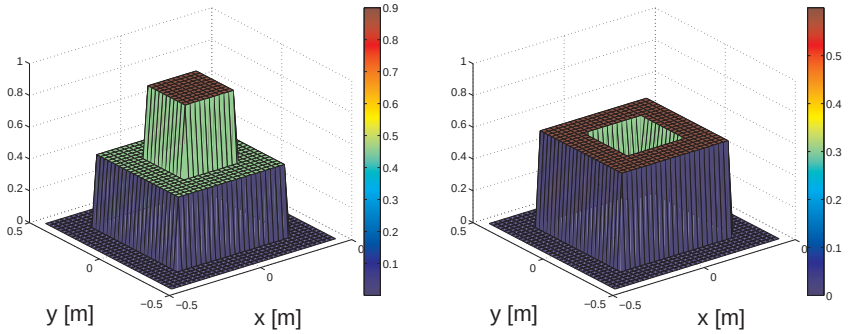

(a) Exact $Re(\chi)$ (b) Exact $Im(\chi)$

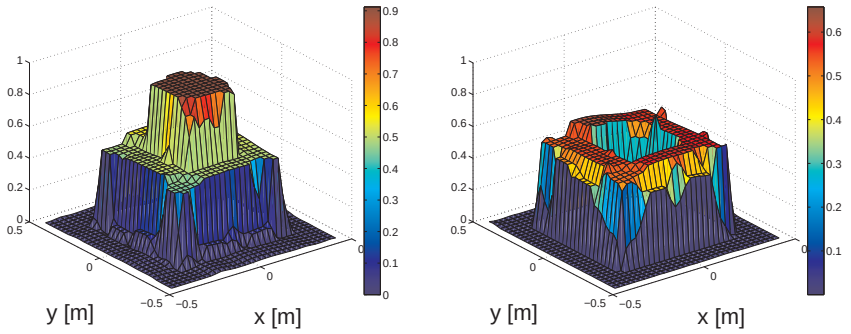

(c) Enclosed $Re(\chi)$ (d) Enclosed $Im(\chi)$

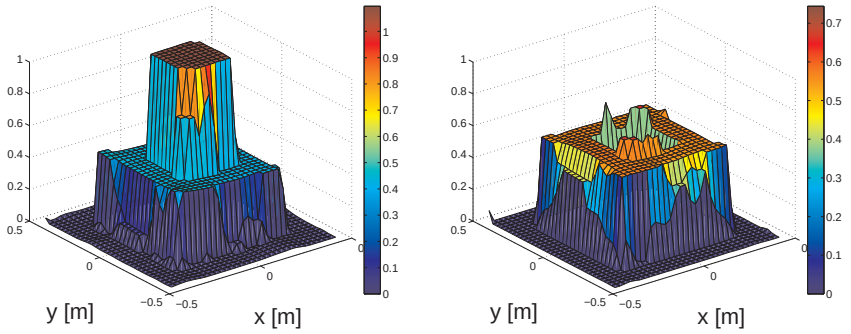

(e) Open $Re(\chi)$ (f) Open $Im(\chi)$

Fig. 6.7: Mid Contrast Concentric Squares after 1024 steps of the MR-CSI algorithm. (a-b) The exact contrast of the scatterer. (c-d) The MR-CSI reconstruction when the both forward data generation and inversion include a circular PEC enclosure. (e-f) Reconstruction when both the forward data generation and inversion assume an open-region background.

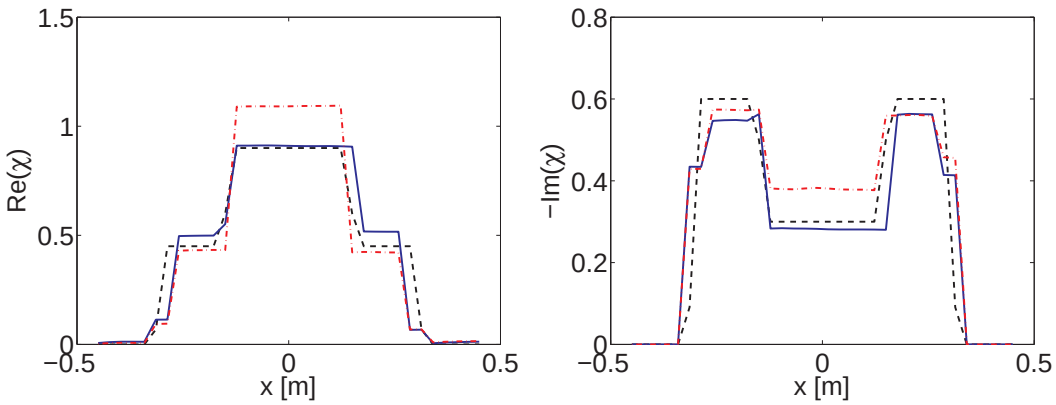

(a) $Re(\chi)$ (b) $Im(\chi)$

Fig. 6.8: Cross-section of mid contrast concentric squares scatterer. (a-b) show a 1D cross section at $y = 0$ for exact (black dash line), conductor-enclosed (blue solid line), and open-region (red dash-dot) reconstructions.

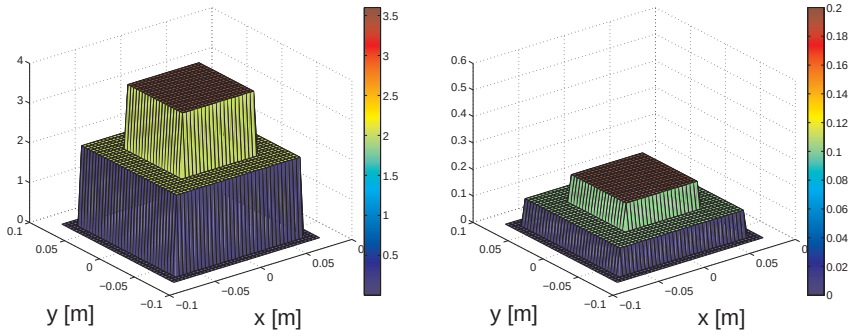

(a) Exact $Re(\chi)$ (b) Exact $Im(\chi)$

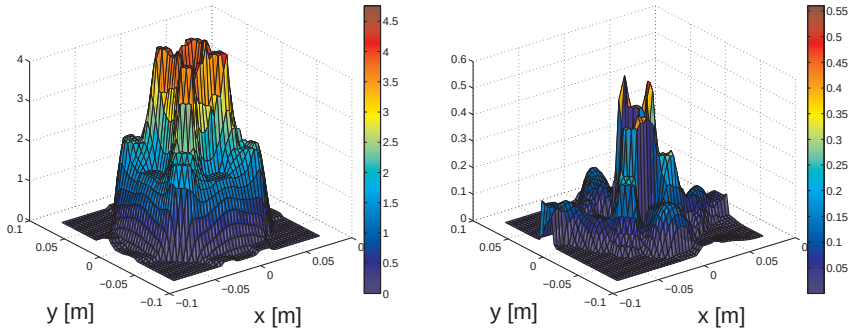

(c) Enclosed $Re(\chi)$ (d) Enclosed $Im(\chi)$

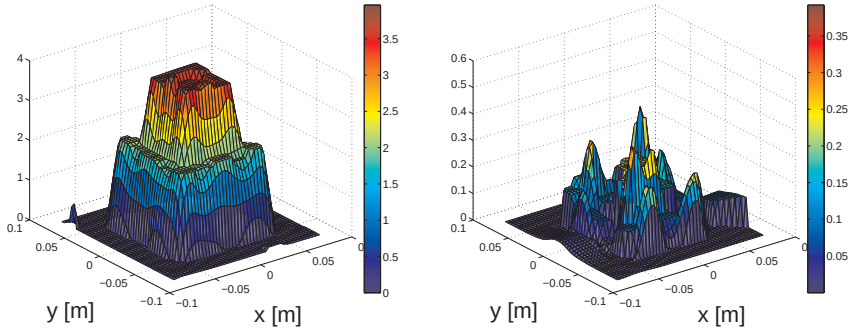

(e) Open $Re(\chi)$ (f) Open $Im(\chi)$

Fig. 6.9: Mutli-Frequency Concentric Squares after 1024 steps of the MR-CSI algorithm. (a-b) The exact contrast of the scatterer. (c-d) The MR-CSI reconstruction when the both forward data generation and inversion include a cylindrical PEC shield. (e-f) Reconstruction when both the forward data generation and inversion assume a free-space background.

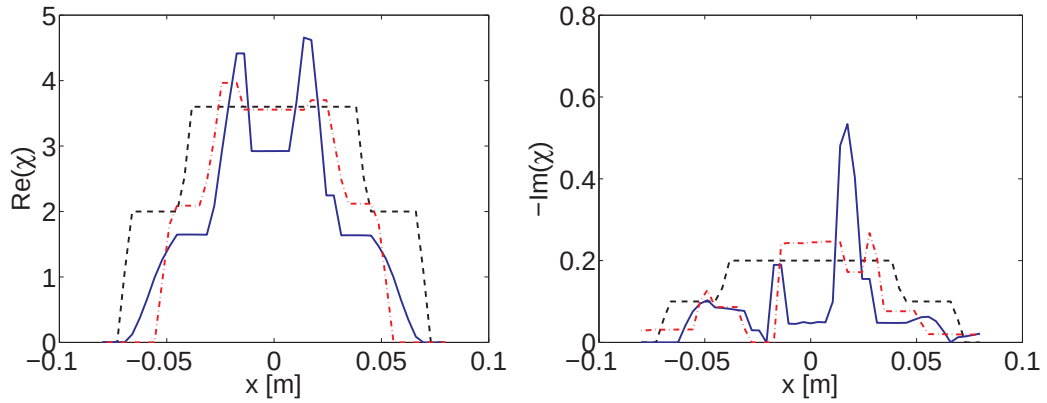

(a) $Re(\chi)$ (b) $Im(\chi)$

Fig. 6.10: Cross-Section of the Mutli-Frequency Concentric Square Scatterer. (a-b) A 1D cross section at $y = 0$ for exact (black dash line), conductor-enclosed (blue solid line), and open-region (red dash-dot) reconstructions.

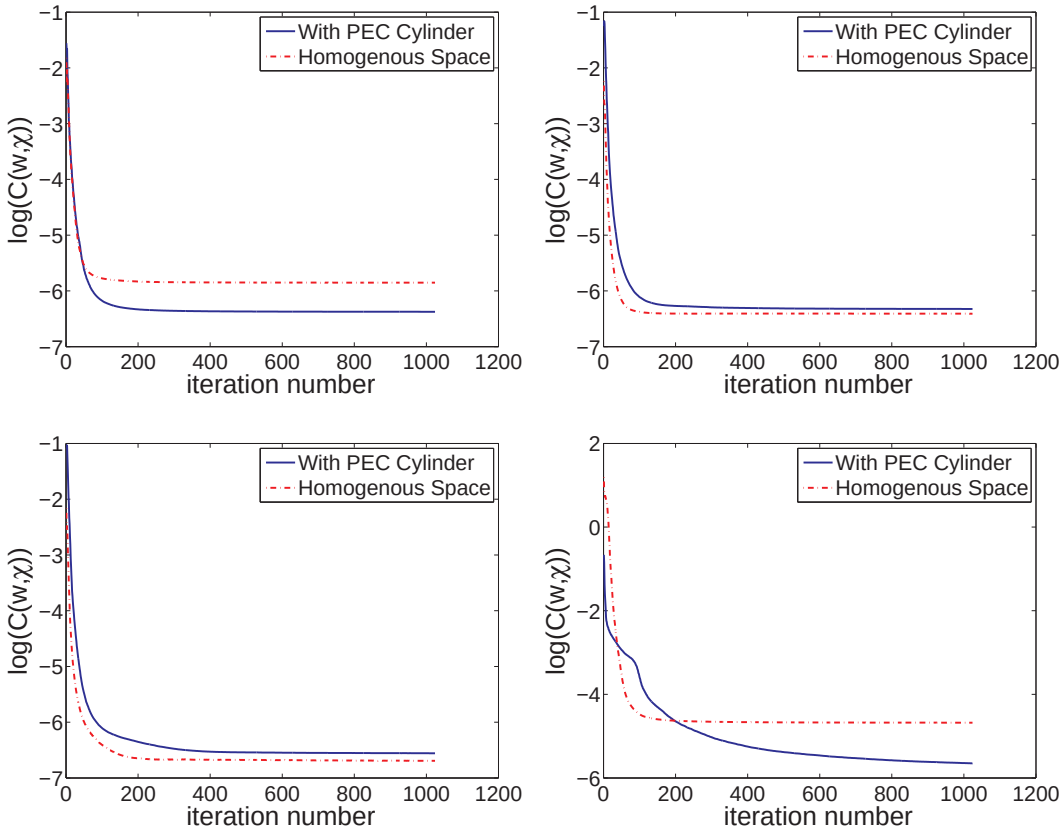

Fig. 6.11: The MR-CSI objective function, $C(w, \chi)$ vs. iteration number for (a) simple square, (b) low contrast concentric squares, (c) high-contrast concentric squares and (d) multi-frequency concentric squares reconstruction

7. EXPERIMENTAL MICROWAVE TOMOGRAPHY SYSTEM AND RESULTS

Research is what I'm doing when I don't know what I'm doing.
Wernher von Braun

While the use of synthetic data for investigating inversion techniques may be instructive, ultimately, all inversion techniques must be tested on experimental data. Adding noise to the synthetically generated field data may avoid the inverse crime, but the actual noise in data obtained from experimental data is not so easily modeled: 2D/3D errors, the assumption of scalar fields, external noise sources, and errors due to near-field effects of antennas all play critical roles in practical MWT performance.

Our group at the University of Manitoba has constructed several prototype MWT systems. One type of system is an open-region ultra-wideband system, which is modeled with an open-region Green's function. The others are conductor-enclosed system, modeled with the enclosed Green's function outlined in chapter 6. The enclosed system will operate at similar, and lower frequencies bands than the open-region system. All results presented herein use free-space as the background medium.

Although these systems will allow the use of various fluids as matching media, currently the antennas that are used have not been designed for immersion inside such media. Note that a lossy background matching material will reduce errors such as reflections from non-radiating antenna elements, but it is instructive to see the effects of these errors without the matching fluid.

7.1 Overview of Open-Region MWT System

A photograph of the current open-region prototype is shown in Fig.7.1. We have employed a two-port Agilent 8363B PNA-Series Network Analyzer (NA) as our microwave source and receiver, capable of producing measurements at discrete frequencies or sweeps within the required frequencies at an approximate system dynamic range of 120dB (an additional 15dB of dynamic range is available using the configurable test set). The NA is connected to the antennas with a 2×24 cross-bar mechanical switch (Agilent 87050A-K24), which provides excellent isolation (> 100 dB) over the frequency range of interest. Twenty-four antennas are arranged at even intervals of 15 degrees in a circular array at the midpoint height along the inside of a plexiglass cylinder. The cylinder has a radius of ≈ 22 cm, is 50.8 cm tall and is water-tight, allowing it to be filled with a matching liquid at a future time. For use with certain classes of test targets, there is also a motor assembly located underneath the cylinder support structure that consists of two precision stepper motors arranged to provide accurate positioning of the target within the chamber. The test target may be placed

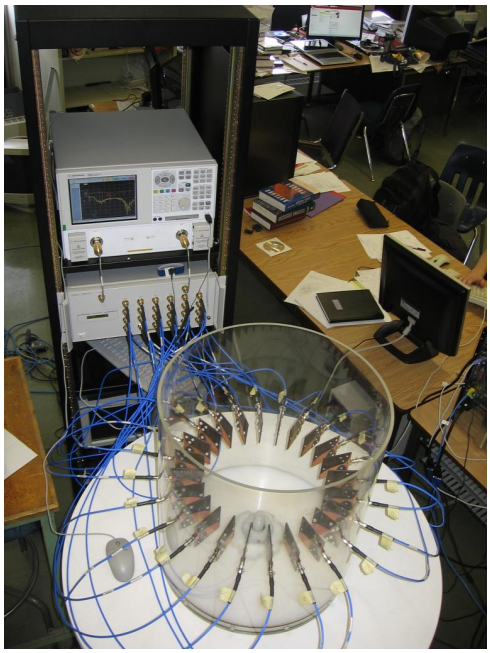

Fig. 7.1: The open-region microwave tomography system. The 24 Vivaldi antennas are connected to a network analyzer via a 2×24 switch.

on a teflon platform mounted on a central teflon pillar protruding from a water-tight, sealed hole in the center of the cylinder's bottom boundary. The platform can be rotated 360° (at increments smaller than 1° if needed). A vertical movement range for the pillar of roughly 15 cm is also accommodated by the motor assembly to provide full 3-D positioning of the target through the 2-D plane of the antenna array.

Communication between the NA, switch, and the controlling computer is accomplished through the General Purpose Interface Bus (GPIB), operating via a GPIB-Ethernet hub. The data acquisition process is entirely automated: a measurement of $23 \times 24 = 552$ data points takes less than 1 minute.

7.1.1 Antenna Description

For the open-region system, we currently use Vivaldi antennas, based on [121], which have been specifically designed and improved for this near field microwave imaging system [122].The design bandwidth of the antennas is from 3 GHz to 10 GHz, although in practice we have found them to be usable from to 2-10 GHz. These antennas utilize a double-layer construction which significantly reduces the cross-polarization level of radiation pattern [122]. This is critical to the use of the scalar 2D assumption about the wave propagation in the chamber, as antennas which create and detect x and y polarized fields would seriously degrade the resultant images. A picture of one of the antennas is shown in Fig. 7.2.

It is further desirable that these antennas have a radiation pattern as similar as possible to an ideal 2D line source ideal radiator, as this is the assumed source for the inversion algorithms used throughout. A plot of the gain pattern of a single antenna in the far-field region for the E_z polarization in the xy plane is given in 7.3. The main beam has a 70° beamwidth, and is relatively flat across the center of the beam. While we can expect this pattern to be significantly different inside the chamber (mostly due to the presence of the other co-resident antennas), we experimentally choose specific frequencies at which the coupling to the other antennas is minimal. At these frequencies the incident field should be reasonably close to that of an ideal 2D line source inside the inversion domain.

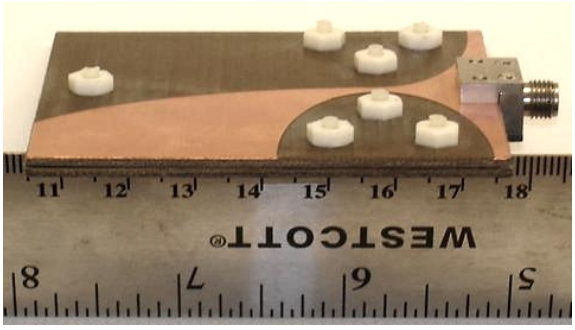

Fig. 7.2: Close-up of one of the double layered Vivaldi antennas used in the microwave imaging system. The two layers are held together with teflon screws.

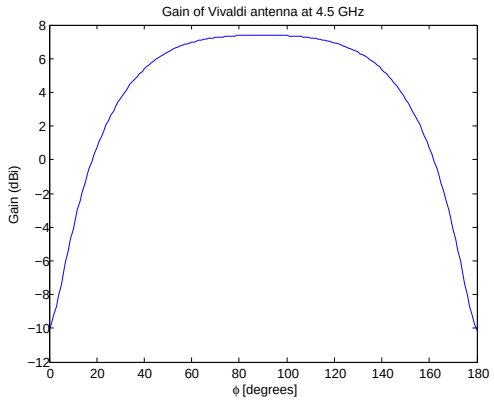

Fig. 7.3: Log-scale Gain of the Vivaldi antenna in the H-plane.

7.1.2 Data collection and System Calibration

As the MWT inversion algorithms require scattered field measurements, and any physical system is only capable of detecting the total field, the raw data are first collected for the MWT system with no scatterer present. This data, labeled the 'incident' measurement, is then subtracted from all the subsequent data so that to produce the scattered field data.

The scattered data must then be calibrated. There are two purposes for the calibration: (i) to convert the S_{21} values of the NA into u (E_z) field values used in the inversion algorithms, and (ii) to eliminate/compensate for as many measurement errors as possible. To perform the calibration, we first measure scattered data from a metallic cylinder with a known radius placed in the middle of the chamber. We denote these S parameters as $S_{21}^{\text{sct,known}}$. Next, the scattering experiment is repeated, but with the unknown target present. These S parameters are denoted $S_{21}^{\text{sct,unknown}}$. Assuming a 2D line source generated incident field, we further denote the analytic scattered fields from the known metallic cylinder as u_{known}^{sct}. These values are calculated analytically [38].

Finally, the calibrated measured fields for the unknown target are calculated by

$$u_{\text{cal}}^{\text{sct}} = \frac{u_{\text{known}}^{\text{sct}}}{S_{21}^{\text{sct,known}}} S_{21}^{\text{sct,unknown}}. \tag{7.1}$$

This method of calibration will eliminate any errors which are constant over the two

(S_{21}^{sct} known and unknown) measurements. Examples of these types of 'removable' errors include cable losses and phase shifts, or mis-matches at connectors. However, there are other factors in the measurement which are not constant between the two measurements, and thus not entirely removed via the above calibration object. For example, the antenna factor is not guaranteed to be the same for the known and unknown measurements (as the system is operating in the near field). Another critical component is the antenna coupling. For these reasons, the known object should be as similar as possible to the expected class of unknown target. The use of a metallic cylinder is not the only option: for example some MWT systems [123] [3] utilize the 'known' object to be the empty chamber (i.e., the incident measurement is utilized).

7.1.3 Antenna Coupling

In the current free-space configuration, one of the largest sources of error is the antenna coupling, which tends to change the radiation properties of the antennas, taking it further away from being well approximated as a line source. That is, the other co-resident antennas can significantly change the radiation properties of the antennas. As the coupling between the antennas will change significantly depending upon the total fields, and the total fields result from the scatterer inside the MWT system, the antenna coupling is a source of error which is not entirely removable by the calibration procedure.

In an attempt to quantify the strength of the coupling between the 24 co-resident

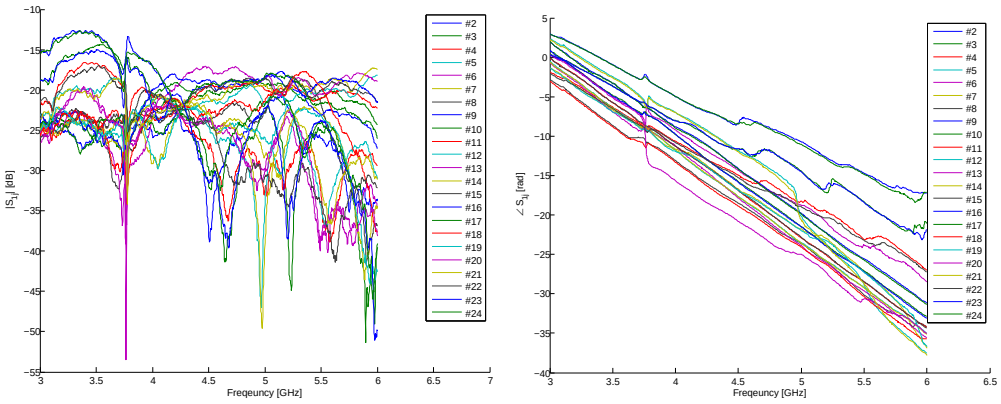

Fig. 7.4: Measurement of S_{1j} for Vivaldi antennas. (a) $|S_{1j}|$, and (b) angle(S_{1j}). For this measurement, all 24 antennas are co-resident in the tank.

antennas at different frequencies, we first measured the S_{1j} parameter of the antennas ($j = 2 \ldots 24$). These results are shown in Fig. 7.4. While these values of antenna coupling may seem low from an antenna design perspective, they are high enough to cause significant problems with the measurements (as analyzed below). Research to obtain a usable coupling reduction method from this information is ongoing.

To obtain usable frequencies for our inverse scattering experiments, we currently use the following procedure: measure the S_{11} parameter for a single antenna when no other antennas are present in the tank. This measurement is shown as the thick black line in Fig. 7.5. Next, the other 23 antennas are all placed in the MWT system, and the remaining S_{ii} measurements are taken. These measurements are shown as the colored lines in Fig. 7.5.

The S_{ii} measurement of Fig. 7.5 provide an idea of where the antennas are strongly/weakly coupling: we have found this plot to be predictive of which frequencies

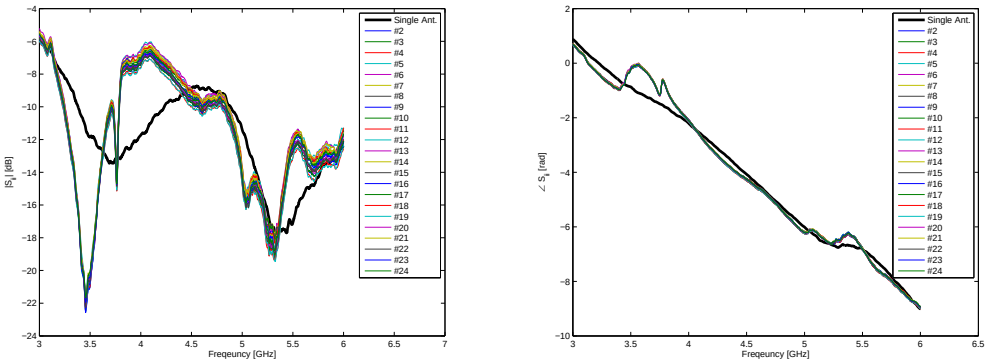

Fig. 7.5: Measurement of S_{ii} for Vivaldi antennas. (a) $|S_{ii}|$, and (b) angle(S_{ii}). The bold black line is a representative measurement when only a single antenna is present, the thin colored lines are the measurements for each antenna when all 24 antennas are co-resident in the tank.

will provide reasonable imaging results, and which frequencies will not. The usable-frequency selection is accomplished by avoiding the frequencies where there are large differences between the single antenna measurement and the co-resident measurement. For example, there is a significant difference between the single and co-resident measurements at 3.5 GHz and 4 GHz, while there are much smaller differences at 3 and 4.5 GHz. In order to show the effects of these differences, in Figs. 7.6 and 7.7 compare the analytic scattered fields from a metallic cylinder of radius 4.445 cm versus the calibrated measurement at 3, 3.5, 4, and 4.5 GHz. At the two frequencies where the co-resident S_{ii} measurements are significantly different than the free-space single S_{ii} antenna measurement (3.5 and 4 GHz), the calibrated measurements are much worse for both magnitude and phase. For example, the maximum relative error at 3.5 GHz is $\approx 70\%$, while the maximum relative error at 3 GHz is $\approx 20\%$. These figures

provide justification for the use of this basic method for avoiding the frequencies where the antennas are strongly coupling.

We do note that even for the cases where the coupling seems to be minimal (Fig. 7.7) there are still significant errors (e.g., at 4.5 GHz, the maximum relative error is $\approx 25\%$). These errors are most likely due to the continued near-field coupling between the antennas, and the fact that the metallic scatterers used for the calibration of the system and S_{ii} comparison purposes were not true 2D objects. This conjecture is based on the fact that other MWT systems with 2D objects and far-field antennas do not see errors as a large as this [85, 124]. For reference, the metallic cylinder used for calibration has a radius of 2.54 cm and is 65 cm tall, while the cylinder used for the comparison measurement has a radius of 4.445 cm, and a height of 46 cm. Cylinders of different radii were selected to avoid calibrating and measuring the scattered fields with the same object, which would have provided an overly-optimistic estimation of the experimental system accuracy.

7.2 Results for Open-Region Experimental System

7.2.1 Scatterer #1

As initial phantom experiments, we utilize a circular teflon cylinder with a diameter of 3.8 cm (1.5 inches) and an (approximately) square cross-section wooden cylinder. With the Agilent 85070E dielectric probe kit, we measured the wood to have a contrast

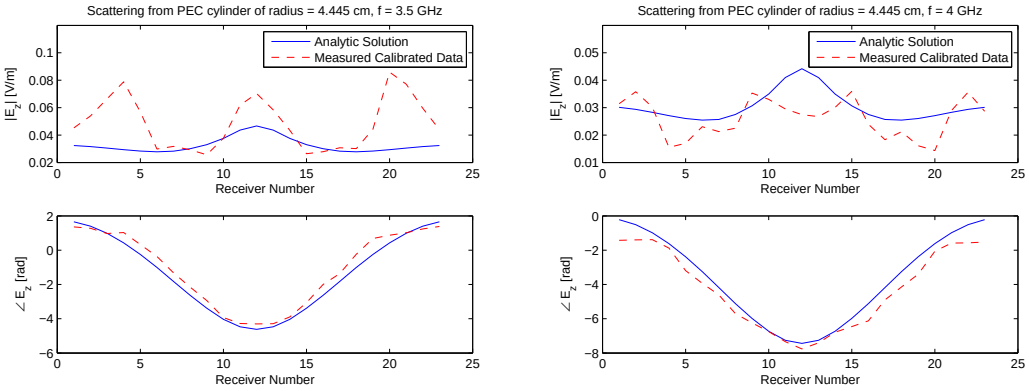

(a) (b)

Fig. 7.6: Magnitude and phase comparison of scattered fields (E_z) from a PEC cylinder at frequencies where the effects of antenna coupling are large: (a) 3.5 and (b) 4 GHz. The solid blue line shows the analytic solution, and the calibrated measured fields are shown with a dashed red line. The radius of the cylinder is 4.445 cm.

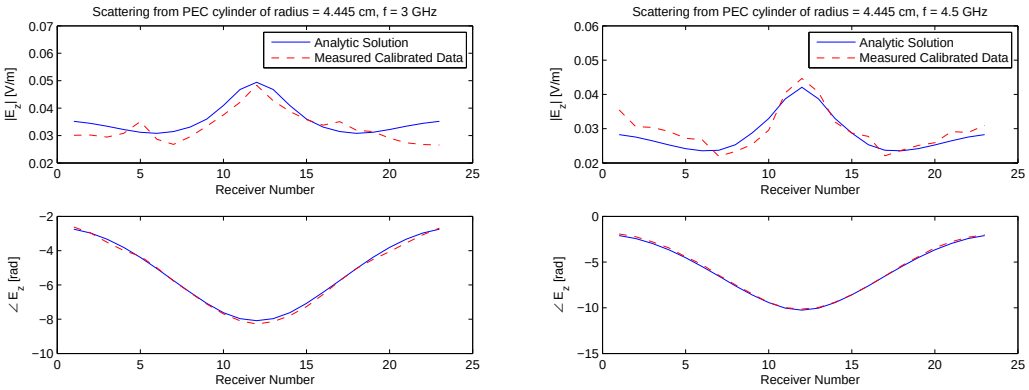

(a) (b)

Fig. 7.7: Magnitude and phase comparison of scattered fields (E_z) from a PEC cylinder at frequencies where the effects of antenna coupling are small: (a) 3 and (b) 4.5 GHz. The solid blue line shows the analytic solution, and the calibrated measured fields are shown with a dashed red line. The radius of the cylinder is 4.445 cm.

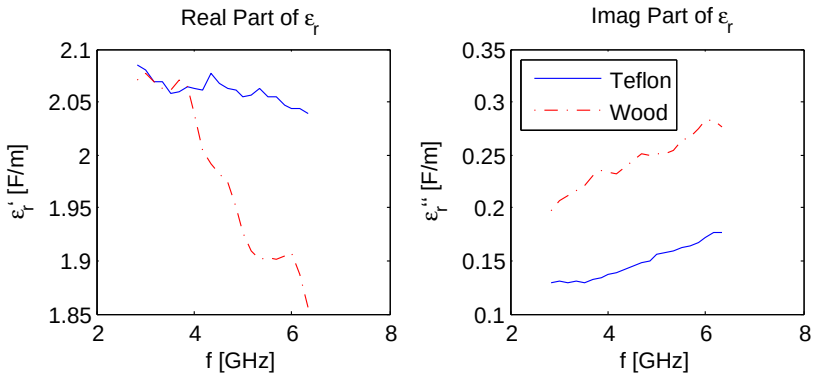

Fig. 7.8: Measured dielectric constant of teflon rod and wood block.

of $\chi^{\text{wood}} \approx 1.0 - j0.2$, and the teflon to have a contrast of $\chi^{\text{tefl.}} \approx 1.1 - j0.13$ (both at 3 GHz). A plot of the measured complex dielectric constant as a function of frequency for the teflon and wood is shown in Fig. 7.8. Due to the fact that the lossy part of the dielectric constant does not vary significantly, we assume a constant dielectric constant for all frequencies. i.e., $\epsilon''(\omega) = \text{const}$, as opposed to the usual Maxwell model [31, 64], where $\epsilon''(\omega) = \sigma/(\omega\epsilon_0)$.

The targets were placed in the chamber, as shown in Fig. 7.9 with an air background, and 23×24 measurements were taken for the frequencies of 3 and 6 GHz.

The single-frequency 3 GHz reconstruction from the enhanced-DBIM method is shown in (a) and (b) of Fig. 7.10, and a frequency-hopping based reconstruction is shown in (c) and (d) of Fig. 7.10. With the frequency-hopping scheme, the data from each frequency are inverted independently, and the solution from the lower frequency is used as the initial guess for the next higher frequency. As previously mentioned, we have found the DBIM to be better suited to a frequency-hopping approach rather

than a simultaneous multi-frequency reconstruction.

For the 3 GHz DBIM reconstruction (Fig. 7.10 (a) and (b)) we note that the real part of the contrast shows the overall structure of the targets quite well, but the reconstruction for teflon is too high: $Re(\chi_{\text{recon}}) = 1.6$ instead of the expected value of $Re(\chi) = 1.1$. For the wooden object, the real part of the contrast is reconstructed as ≈ 1.1, which is quite accurate, and the reconstruction shows a homogeneous region (which is what we expect). For the imaginary part of the DBIM 3 GHz reconstruction, we note that the presence of the two distinct objects is clear, but the imaginary part of the teflon is clearly overshot ($Im(\chi_{\text{recon}}) \approx -0.6$, when it should be $Im(\chi) = -0.13$). Further, the imaginary part of the contrast for the wooden object is not homogeneous, although the expected value of $Im(\chi) = -0.2$ is achieved in the center.

For the 3 and 6 GHz DBIM reconstruction, the contrast of the teflon is closer to the expected value than for the single frequency case in both real and imaginary parts ($\chi_{\text{recon}} \approx 1.4 - j0.45$). For the wood, the real part is again accurate (roughly the same as for the 3 GHz reconstruction). The edges of the objects are quite clear in the imaginary part of the reconstructed contrast, and the interior of the wood is more homogeneous, but the edges of the wood show some overshoot (in one particular spot, $Im(\chi_{\text{recon}}) \approx -0.4$ when the expected value is -0.2).

The single-frequency MR-CSI reconstruction at 3 GHz is shown in (a) and (b) of Fig. 7.11, and a simultaneous multi-frequency reconstruction from 3 and 6 GHz data in (c) and (d) of Fig. 7.11. In the multi-frequency case, data from all frequencies are

simultaneously inverted, with the data from each frequency equally weighted.

Similar to the DBIM case, the MR-CSI 3 GHz reconstruction over-estimates the value of the teflon cylinder to be $Re(\chi_{\text{recon}}) \approx 1.6$ when it should be 1.2. The edges of the wood are not reconstructed as straight lines, and while the real part of the contrast is homogeneous, the value of the contrast is too low: ($Re(\chi_{\text{recon}}) \approx 0.85$ instead of 1.0). For the imaginary part of the reconstruction, the contrast for the teflon is also overestimated (-0.6 instead of -0.13), and there is a point of high loss in the wood (-0.4 instead of -0.2).

In the multi-frequency MR-CSI reconstruction, Fig. 7.11 (c) and (d), the real part of the contrast over-estimates the value of teflon, but achieves the expected value for the wood (1.1). Additionally, the edges of the wood are much straighter. The imaginary part of the contrast misses the value of the teflon (i.e., shows a contrast of zero when it should be -0.13), but all values of $Im(\chi_{\text{recon}})$ are not over-estimated. The reconstruction of the wood is again inhomogeneous in $Im(\chi)$ reconstruction.

Finally, we also note that the off-axis rotation of the wood in all reconstructions reflects the physical orientation of the wood for the measurement.

7.2.2 Scatterer #2

The second scatterer consists of the same teflon cylinder, but this time combined with a hollow Poly-Vinyl-Chloride (PVC) cylinder. A photograph of the phantom is shown in Fig. 7.12. The thickness of the PVC cylinder is ≈ 0.6 cm, and it has a radius of

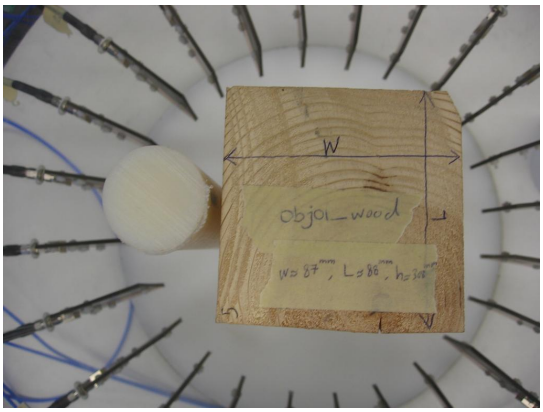

Fig. 7.9: Dielectric phantom target consisting of teflon and wooden cylinders.

≈ 6.5 cm. The permittivity of the PVC cylinder was not measured, because the thin width of the cylinder wall would make the measurements invalid (the measurement would require a larger mass of PVC).

For this phantom, data were collected at 3, 4.5 and 6 GHz. The enhanced DBIM reconstruction at 3 GHz is shown in (a) and (b) of Fig. 7.13 and the marching-on-frequency reconstruction is shown in (c) and (d) of Fig. 7.13. The MR-CSI single frequency reconstruction at 3 GHz is shown in (a) and (b) of Fig. 7.14, and the simultaneous multi-frequency reconstruction is shown in (c) and (d) of Fig. 7.14.

Similar to the previous phantom, the DBIM 3 GHz reconstruction (Fig. 7.13 (a) and (b)) overestimates the real part of the contrast for the teflon (2.2 instead of 1.2). The thickness of the PVC is estimated to be too wide (≈ 1.7 cm instead of 0.6 cm). In the imaginary part of the DBIM 3 GHz reconstruction, the overall structure of the phantom is not visible. This is mostly due to the large artifact in the center of the PVC pipe, and on the edge of PVC pipe closer to teflon. The value of $Im(\chi_{\text{recon}})$ for

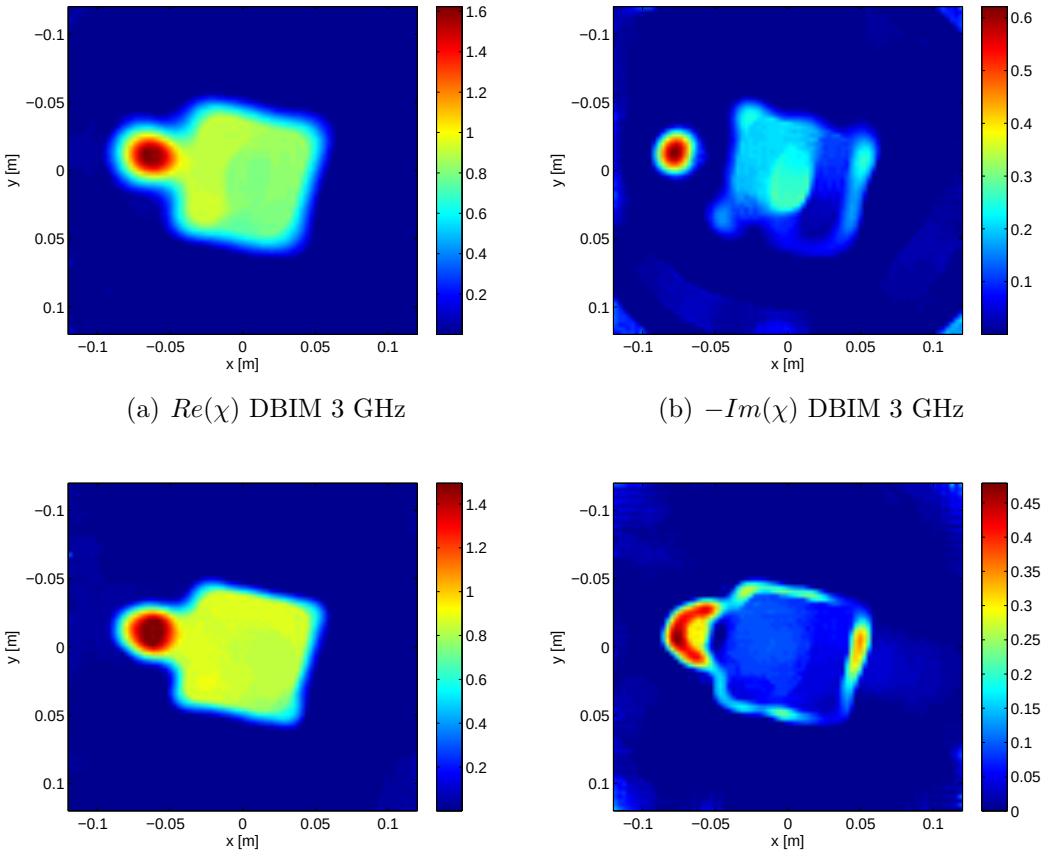

(a) $Re(\chi)$ DBIM 3 GHz

(b) $-Im(\chi)$ DBIM 3 GHz

(c) $Re(\chi)$ DBIM 3 and 6 GHz

(d) $-Im(\chi)$ DBIM 3 and 6 GHz

Fig. 7.10: (a) $Re(\chi)$ and (b) $-Im(\chi)$ show the DBIM reconstruction of the dielectric phantom #1 at 3 GHz. (c) and (d) show the real and imaginary parts of χ for DBIM reconstruction of the phantom using a frequency-hopping reconstruction at 3 and 6 GHz.

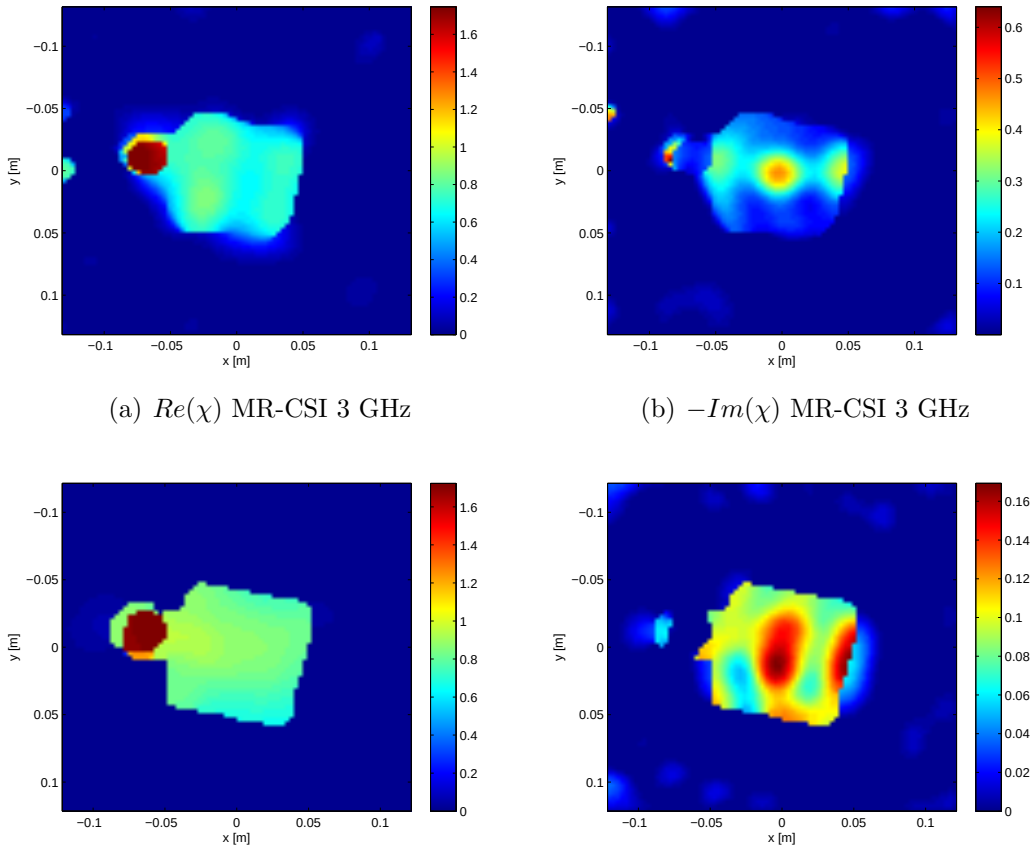

(a) $Re(\chi)$ MR-CSI 3 GHz

(b) $-Im(\chi)$ MR-CSI 3 GHz

(c) $Re(\chi)$ MR-CSI 3 and 6 GHz

(d) $-Im(\chi)$ MR-CSI 3 and 6 GHz

Fig. 7.11: (a) $Re(\chi)$ and (b) $-Im(\chi)$ show MR-CSI reconstruction for phantom #1 at 3 GHz. (c) and (d) show the real and imaginary parts of χ for the MR-CSI reconstruction of phantom #1 using a simultaneous frequency reconstruction at 3 and 6 GHz.

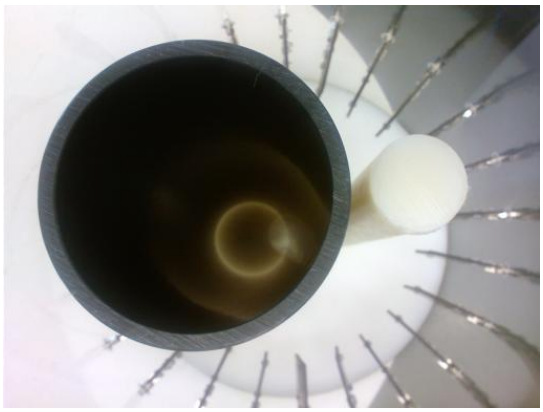

Fig. 7.12: Scatterer 2: Dielectric phantom target consisting of PVC and teflon cylinders. The separation between the cylinders is 1 cm.

the teflon is -0.2, but the edges are blurred.

The multi-frequency DBIM reconstruction, Fig. 7.13 (c) and (d), has less overshoot in the real part of the teflon, (2.0 instead of 1.2). The real part of the PVC pipe reconstruction is thinner and closer to the actual size (≈ 1.2 cm). In the imaginary part of the reconstruction, the Teflon's shape is not really visible, and the value is overshot (-0.3 instead of -0.13). Additionally, in the imaginary part of the PVC pipe's shape does not follow the entire way around the cylinder. However the artifact in the center of the PVC cylinder has disappeared.

In the single-frequency MR-CSI reconstruction, there is again an overestimate of the real part of the contrast for the teflon (2.3). The separation of the PVC and teflon is not at all clear and they are blurred together. The overall shape of the PVC cylinder is clear, but the thickness is overestimated (≈ 1.67 cm, instead of 0.6 cm). In the imaginary part of the MR-CSI single frequency reconstruction, the overall structure is

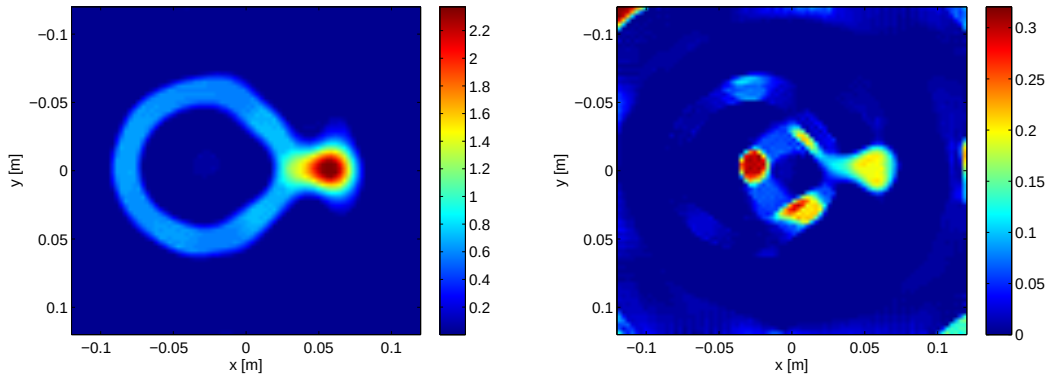

(a) $Re(\chi)$ DBIM 3 GHz

(b) $-Im(\chi)$ DBIM 3 GHz

(c) $Re(\chi)$ DBIM 3-6 GHz

(d) $-Im(\chi)$ DBIM 3-6 GHz

Fig. 7.13: (a) $Re(\chi)$ and (b) $-Im(\chi)$ show the DBIM reconstruction of the dielectric phantom #2 at 3 GHz. (c) and (d) show the real and imaginary parts of the DBIM reconstruction using a marching-on-frequency reconstruction at 3, 4.5 and 6 GHz.

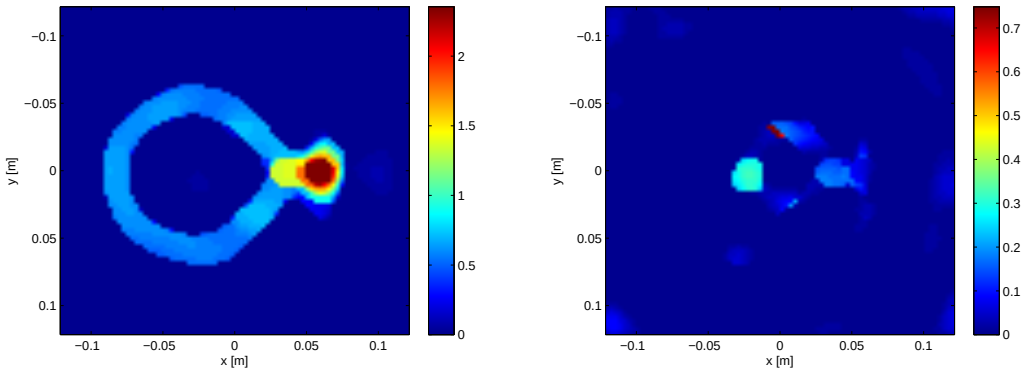

(a) $Re(\chi)$ MR-CSI 3 GHz

(b) $-Im(\chi)$ MR-CSI 3 GHz

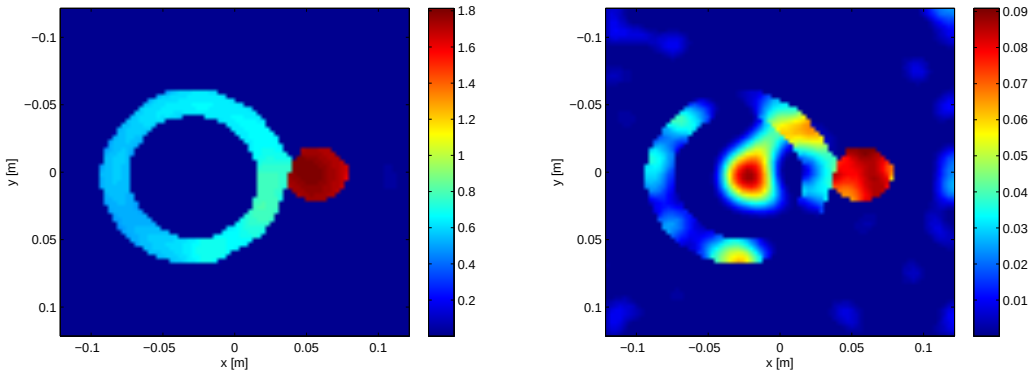

(c) $Re(\chi)$ MR-CSI 3-6 GHz

(d) $-Im(\chi)$ MR-CSI 3-6 GHz

Fig. 7.14: MR-CSI reconstruction of the dielectric phantom #2. (a) $Re(\chi)$ and (b) $-Im(\chi)$ of the reconstruction at 3 GHz. (c) $Re(\chi)$ and (d) $-Im(\chi)$ show the reconstructions using a simultaneous frequency reconstruction at 3, 4.5 and 6 GHz.

not visible, and there is a large artifact in the center of the inversion domain.

The multi-frequency MR-CSI reconstruction shows less overshoot in the real part of the teflon (1.8). The two objects are very distinct, although the physical separation of 1 cm is not. The PVC is shown to be about same width (1.67 cm). The imaginary part of the reconstruction shows the teflon size (3.8 cm) and contrast quite accurately (i.e., -0.1 when it should be -0.13). In the imaginary reconstruction, the PVC shape is visible but with includes artifacts and holes. Additionally, there still is a large artifact in the center of the imaging domain.

7.2.3 Discussion of Results for Open-region MWT System

In both phantoms, the multi-frequency reconstructions were an improvement over the single-frequency case. This is particularly apparent in the imaginary part of the permittivity of scatterer #2. As expected through the use of higher-frequency data the multi-frequency reconstructions had less blurred edges. As well, in phantom #2, both the DBIM and the MR-CSI multi-frequency reconstructions clearly show that two distinct objects are present, and in the DBIM case, the separation of the two objects is (arguably) visible (the physical separation was 1 cm, or 1/5 of λ at the highest frequency).

In general, the exact contrast/permittivity values were not obtained. For example, in the multi-frequency MR-CSI reconstruction of phantom #2, the permittivity of the teflon is reconstructed as $Re(\chi_{\text{recon}}) = 1.8$, when we expect it to be $Re(\chi) =$

1.1. However, in 3 of the 4 reconstructions of phantom #1, the multi-frequency reconstructions were closer to the true value of the teflon, and were never worse than the single-frequency case. The imaginary part of the permittivity is, in general, not accurately reconstructed, and there are many artifacts in the imaginary part of the reconstructions. This has been seen in other systems [5]. The problems in the imaginary part of the reconstructions were, however, improved with the use of multi-frequency data.

We also speculate that the imaginary part of the permittivity in the wood phantom is not homogeneous, as 3 of the 4 reconstructions of this target show a higher magnitude in the center of the block.

We suspect that these errors in the reconstructions are primarily due to the large amount of measurement noise caused by the coupling of the antennas. Other sources of error, such as the assumption of a 2D line source based incident field are probably less significant, and/or are adequately calibrated out by the calibration process. We expect that when the MWT system is filled with a matching fluid the antenna coupling will become significantly less noticeable due to losses in the fluid.

7.3 Enclosed MWT System Prototype

In addition to the open-region system, our group at the University of Manitoba has constructed several different conductor-enclosed imaging system prototypes. The enclosed system utilizes the same VNA, switch, and data collection process, but

(a) (b)

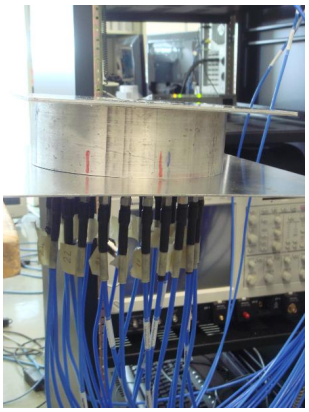

(c)

Fig. 7.15: Some Enclosed MWT system prototypes. (a) Large diameter cylinder with small antennas, (b) top and (c) side views of small diameter prototype with simple wire monopole antennas.

substitutes the plexiglass chamber for a chamber made of stainless steel. Prototypes with different cylinder sizes and with a series of antenna types have been constructed, and data collected from them.

Different prototypes have been constructed so as to systematically study the data collection, calibration, and inversion processes required for this class of system. Obtaining useable data for conductor-enclosed systems is much more difficult than for

the open-region system previously described. In particular, we have determined that (i) the antennas must be taken into account in the inversion solver in a process similar to that outlined in [93–95], and (ii) in a lossless system, as shown in Fig. 7.15, the 3D effects are extremely important, and extra effort must be made to build a system which is as close as possible to a 2D system. Inside of an enclosed chamber, any error in the model (e.g., having an antenna which radiates a field which has significant E_x and E_y components) will lead to significant errors. While this sensitivity has made successful inversion much harder than with the open-region system, we hope that this sensitivity will be advantageous once the calibration issues have been solved.

As with the open-region MWT system, we have also tried to analyze the antenna coupling. But because all the field distributions, at any frequency, are governed by the modes of the resonant enclosure which dictate the coupling, such an approach does not work with the enclosed scanner.

7.3.1 Enclosed System Analysis: Single antenna

In order to better understand the field distributions inside the resonant chamber, we have turned to a full-wave Finite-Volume Time-Domain (FVTD) solver [125–127]. This code utilizes tetrahedral mesh elements, combined with a thin-wire model which is capable of accurately modeling arbitrarily oriented thin wires in the mesh [128]. An example of the FVTD mesh for an enclosed system is shown in Fig. 7.16. For faster computations, the code has been fully parralleized [129].

To analyze the system in full-3D and help us understand the inversion results from the experimental system, we first generated an example enclosed inversion system with a single antenna, as shown in Fig. 7.16. The antenna is a resistively-loaded (Wu-King) dipole [130]. For both simulations, the PEC chamber cylinder had a radius of 10 cm, and a height of 21 cm. The background permittivity throughout the tank was $\epsilon_r = 6$. For the first example (Fig. 7.16 (a)), the scatterer consists of two concentric cylinders of radius 1.5 and 4.5 cm a each having height of 21 cm, and relative permittivities of $\epsilon_r = 12$ and $\epsilon_r = 8$ respectively ($\chi = 1.0$ and $\chi = 1/3$). The Wu-King dipole was located 1/4 of a wavelength (at 2 GHz) away from the PEC edge, had a total length of $\approx$1.5 cm, and was excited using a derivative of a Gaussian incident pulse with significant frequency content to up to 3 GHz. The second scatterer was embedded in the same system, but is now a sphere withing a sphere (the permittivities remain the same, and the radii of the spheres were equal to radii of the cylinders). For both scatterers, the E_z field was recorded at a series of 40 points around the scattering cylinder at the mid-line ($z = 0$) of the chamber, at a radius of 8 cm. Frequency domain data were generated with the Fourier Transform. Due to the fact that the scatterer is symmetric, the FVTD simulation was run only once, and the symmetry used to generate data for 10 transmitters.

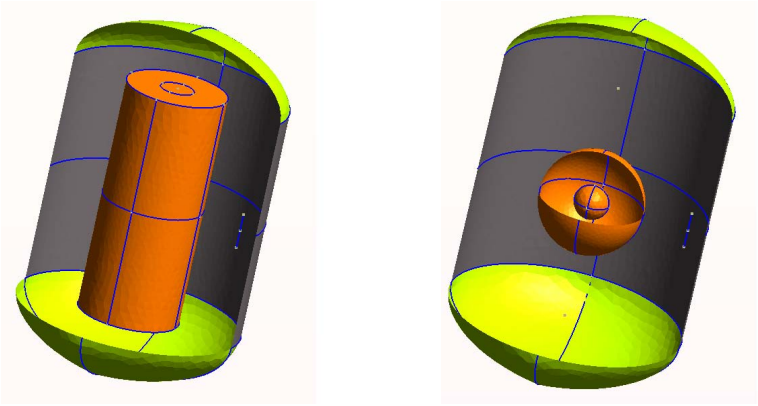

(a) (b)

Fig. 7.16: A simulated enclosed tomographic system with a single Wu-King resistively loaded dipole antenna. (a) shows an elongated (2D) target, (b) shows a spherical target. Only the surfaces of the tetrahedral elements are shown.

7.3.2 Enclosed FVTD Simulation Calibration

Because the FVTD simulated PEC system does not generate the incident field as a line source (as used in the MR-CSI inversion code), the data must be calibrated. Similar to the experimental system, we calibrated the data by utilizing the formula

$$u_{\text{cal}}^{\text{sct}} = \frac{u_{\text{known}}^{\text{inc}}}{u_{\text{FVTD}}^{\text{inc}}} u_{\text{FVTD}}^{\text{sct}}. \tag{7.2}$$

where u_{known}^{inc} is the incident field from a line source inside a true 2D enclosure, $u_{\text{FVTD}}^{\text{inc}}$ is the measured incident field from the 3D FVTD simulation, and $u_{\text{FVTD}}^{\text{sct}}$ is the scattered field taken from the FVTD simulation.

However, when this calibration method was applied to the FVTD data, it did not provide reasonable inversion results. The core assumption of the above calibration

procedure is that, within the inversion domain D, the true incident field is simply a scaled version of the assumed incident field (with a complex scaling constant). Thus, for this calibration procedure to give reasonable results, the plots of the magnitude of the normalized FVTD incident field, $u^{\text{inc}}_{\text{FVTD}}$, and the magnitude of the normalized analytic incident field, $u^{\text{inc}}_{\text{known}}$, should look very similar within D. For the tomographic system shown in Fig. 7.16, such a plot is shown in Fig. 7.17. Part (a) of Fig. 7.17 shows the normalized incident field for a point source in a 2D PEC circular cylinder of diameter 20 cm at a frequency of 2.5 GHz. Part (b) of Fig. 7.17 shows the normalized incident field from the Wu-King dipole, located at the same transmitter position as the point source, at the same frequency within the 3D approximation of the same enclosure. As can be seen, these field distributions are quite different, and a simple scaling is not possible between these two incident fields throughout the imaging region, D. We suspect that these differences are largely due to (i) the 3D nature of the fields from the Wu-King dipole, and (ii) multiple reflections from the dipole not being taken into account with the enclosed Green's function.

A new method of calibrating the incident field by first running the FVTD code for the tomographic system with no scatterers present was introduced. The incident fields in the domain D were recorded at the desired frequencies. Then, these incident fields were used as the incident field for the inversion (i.e., u^{inc} in the MR-CSI algorithm was taken to be the measured FVTD incident field). After this, the calibration of scattered fields using (7.2) was no longer used. Since the knowledge of the incident

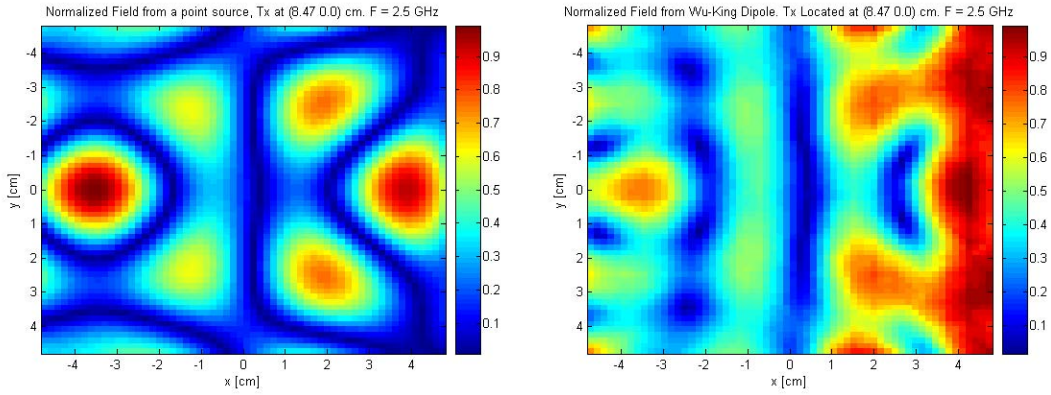

(a) (b)

Fig. 7.17: Normalized magnitude of the incident field at 2.5 GHz in the region D located in a 20 cm diameter PEC cylinder, for (a) a true 2D line source, and (b) A Wu-King dipole in the simulated 3D tomographic system. While both incident fields show resonant effects, the overall shape of the resonances is very different.

fields is required for multiple transmitter positions, we assume that all transmitters are located on a circle of constant radius inside the cylinder, and compute the incident fields by interpolation. This way, the FVTD simulation only needs to be run once (as opposed to once per transmitter), due to the circular symmetry of the tomographic system.

7.3.3 Enclosed FVTD Simulation Results

Using the new calibration method, meaningful inversion results were obtained from the single-antenna FVTD simulation. The reconstruction of the elongated cylinder with the MR-CSI algorithm are shown in 7.18 (a) and (b). Only the real part of the contrast is presented, as the scatterer is lossless. These results show that while the reconstruction has some problems (e.g., the value of the center of the elongated cylinder

is overshot by $\approx 40\%$), this basic calibration method is capable of reconstructing targets inside of the 3D environment. There are more errors in the reconstruction of the sphere, however, we do note that inner sphere is detected, but the exact contrast is not acheived.

7.3.4 Enclosed System Analysis: Multiple antennas

A preliminary study to extend the FVTD-based calibration process described above to a more realistic 24-antenna MWT system has begun in our group [1]. Designed to match the physical prototype shown in Fig. 7.15 (b) and (c), the FVTD mesh of this system is shown in Fig. 7.19. The shorter prototype of Fig. 7.15 (b) and (c) has been constructed because the antennas and scatterers may be better represented as 2D objects, which limits the 2D/3D errors from the system. In this system, the wire antennas extend from the bottom to the top plates of the enclosure.

The same simulation and calibration procedure was applied to this 24 antenna system. However, the inversion using the 2D analytic Green's function did not provide meaningful results. This is due to the presence of the full 24 antennas, which change the Green's function of the system sufficiently such that it cannot be modeled with the analytic homogeneous Green's function as outlined in Chapter 6. Evidence for this may be obtained by considering the plots of the S_{11} measurement when only two antennas are present in the chamber, and the same measurement when the other 22

[1] The work outlined in the next two sections relies on significant efforts from Amer Zakaria, Cam Kaye, and Puyan Mojabi.

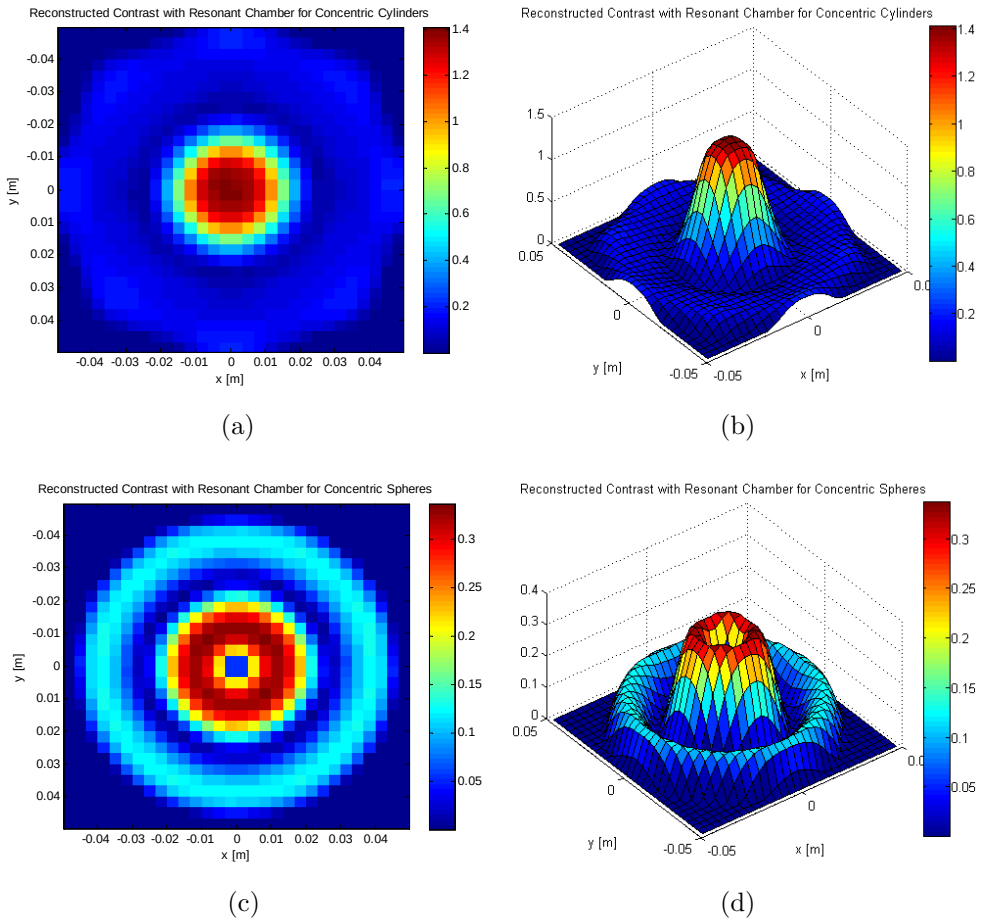

Fig. 7.18: MR-CSI reconstructions from the FVTD simulated single-antenna tomography system. (a) and (b) show the regular and surface image of $Re(\chi_{\text{recon}})$ for the elongated cylinder shown in Fig. 7.16, and (c) and (d) show $Re(\chi_{\text{recon}})$ for the spherical scatterer shown in Fig. 7.16.

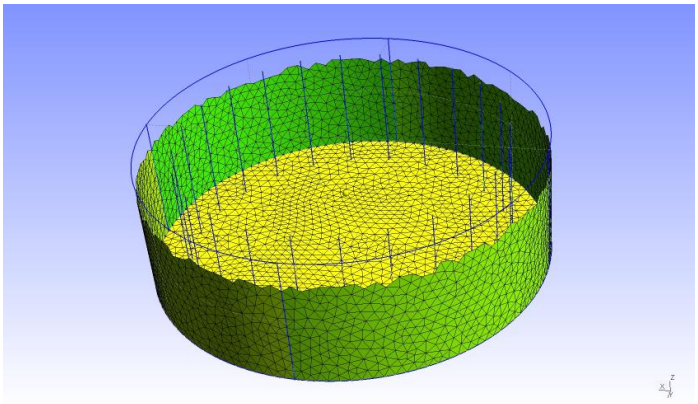

(a)

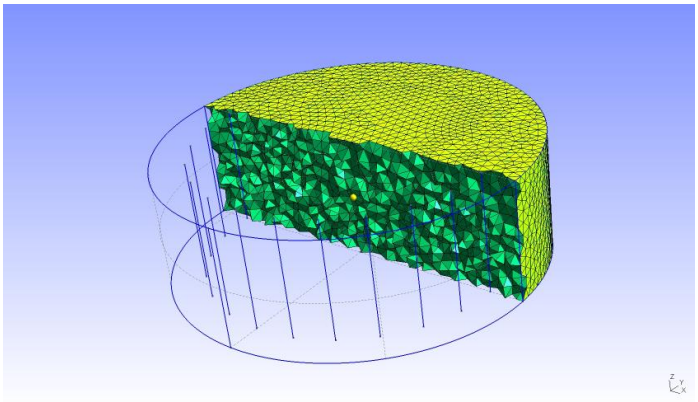

(b)

(c)

Fig. 7.19: Two perspectives on a Finite-Volume Time-Domain mesh of an enclosed MWT system. The experimental prototype being modeled is shown in (c). For measurements with the system, a metallic cover is placed over the top of the chamber.

passive antennas are added to the chamber. This comparison is shown in Fig. 7.20. In particular, the resonances have significantly changed with the introduction of the non-active antennas. Therefore, the presence of the other 23 antennas is substantially changing the input impedance of the transmitting antenna and the field distribution inside the chamber is not that of an empty 2D enclosure.

7.3.5 Experimental Inversion Results with Enclosed MWT system

As a way of further analyzing the enclosed MWT system, we turned to comparing the FVTD fields with the fields generated from a Finite-Element based 2D scalar solver[2] [131]. With the FEM solver, we are easily able to model curved boundaries. We are also able to easily model all the antenna elements in the enclosure. For the prototype shown in Fig. 7.15 (b) and (c), the 2D FRM simulation was performed with small PEC circles representing the antenna elements. The FEM mesh is shown in Fig. 7.21. The whole mesh is shown in Fig. 7.21 (a) and a close-up of an antenna element is shown in Fig. 7.21 (b). At the surface of the PEC antenna elements, the tangential electric field was set to zero.

Due to the fact that the small circles representing the antennas are at the exact positions of the sources/receivers, and that they represent PEC boundaries (where no field may penetrate), we chose to place the source/receiver points $\lambda/20$ away from the edge of the small PEC circles. This leads to some errors in the inversion, and

[2] The FEM solver was developed by Amer Zakaria.

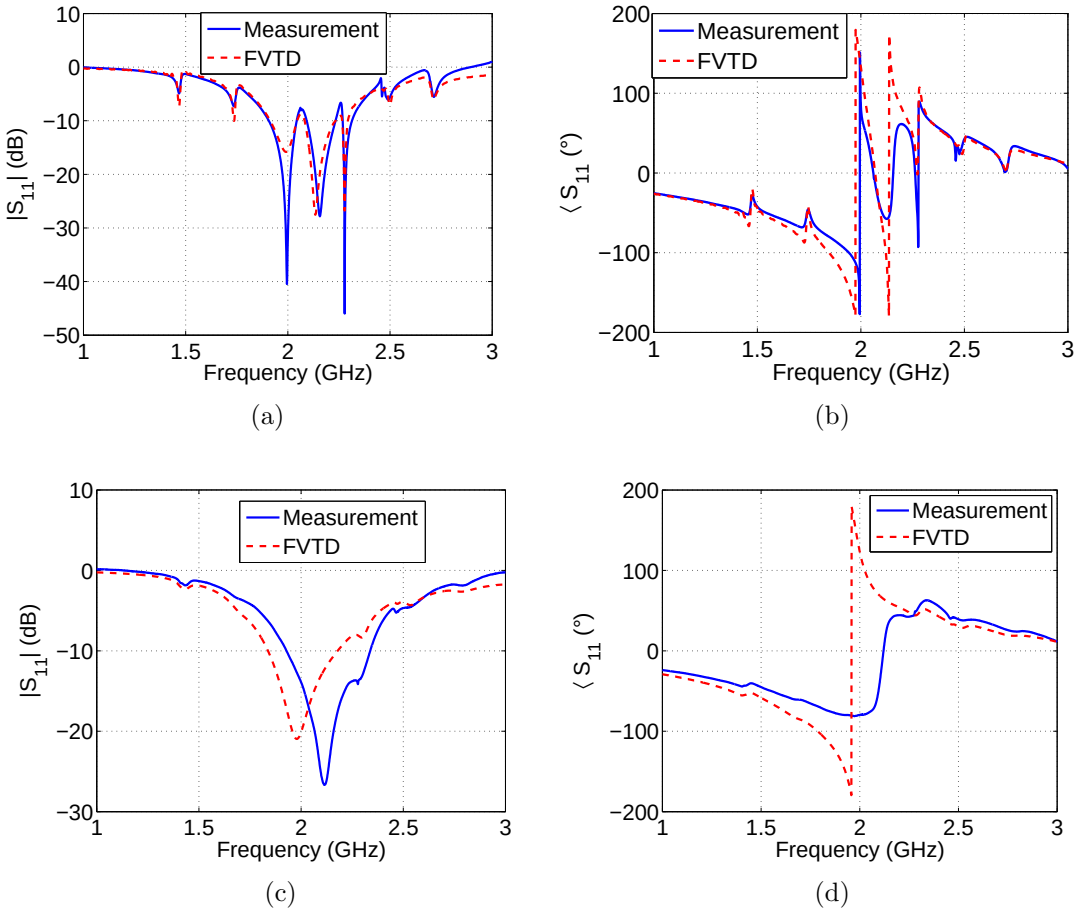

Fig. 7.20: FVTD simulation vs. experimental measurement in the conductor-enclosed MWT system. (a) and (b) show the magnitude and phase of S_{11} when only two antennas are present in the chamber. (c) and (d) show the same measurement when the other 22 non-active antennas are present in the chamber. The two plots are significantly different.

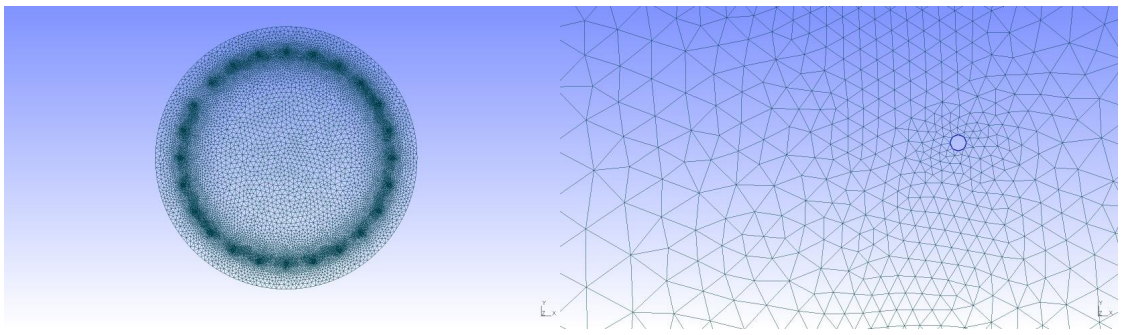

(a) (b)

Fig. 7.21: Example of an FEM mesh for the enclosed system prototype. The 24 antennas are modeled as small PEC cylinders, as shown in the zoomed image (b).

future work will focus on better ways to take the antennas into account. However, this method has provided reasonable inversion results.

Using these FEM simulations, combined with the FVTD full-wave solver (which better matches the physical system), we determine the frequencies at which the fields are well-modeled by the 2D assumption. Examples of the magnitude of the scalar field from the 2D FEM solver at 2.7 and 4 GHz are shown in Fig. 7.22 (a) and (c). These are compared to the magnitude of the E_z field from the full-wave FVTD solver in Fig. 7.22 (b) and (d). As is clear from the figure, the magnitude of the fields matches quite well at 2.7 GHz, and does not match at 4.0 GHz. This similarity of fields is predictive of the inversion results: at 4.0 GHz the inversion results are not meaningful, however, at 2.7 GHz, the inversion results are meaningful.

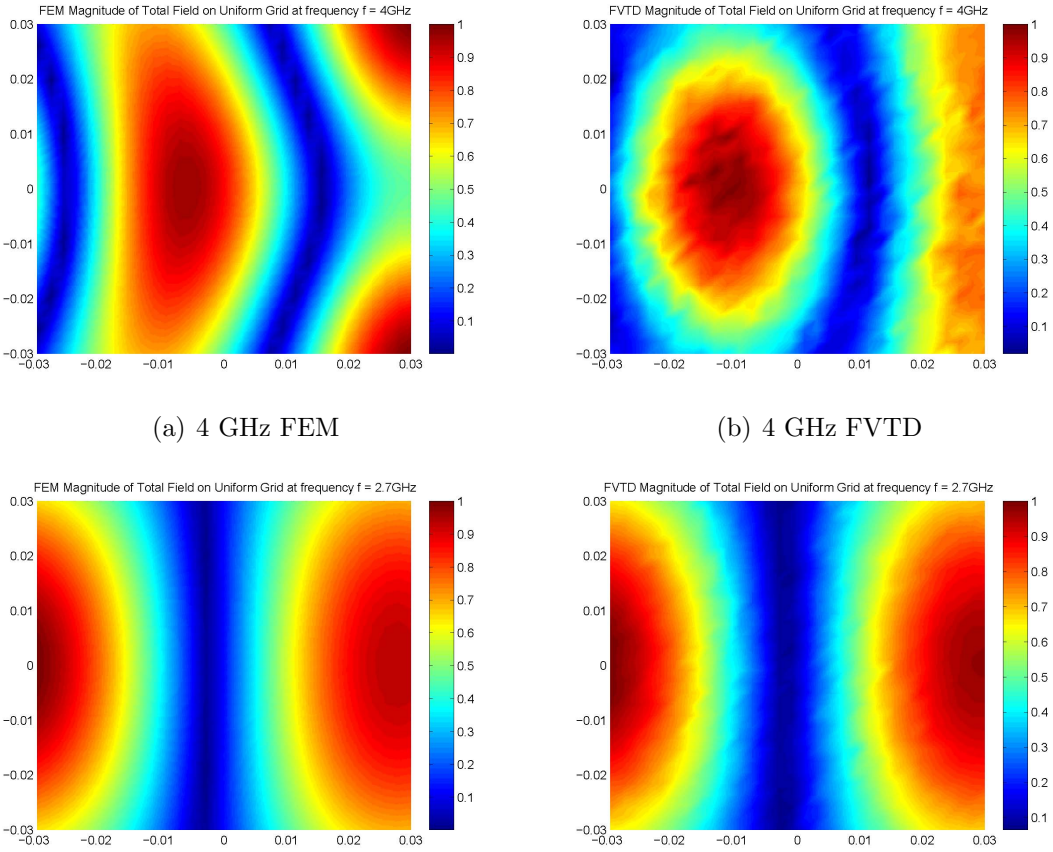

(a) 4 GHz FEM

(b) 4 GHz FVTD

(c) 2.7 GHz FEM

(d) 2.7 GHz FVTD

Fig. 7.22: Magnitude of 2D FEM vs. 3D FVTD Fields inside of imaging domain D. (a) FEM fields at 4.0 GHz (b) FVTD fields at 4.0 GHz. (c) FEM fields at 2.7 GHz, (d) FVTD fields at 2.7 GHz.

Inversion results at 2.7 GHz

The need to take into account the small antenna elements in the Green's function of the inversion solver precludes the use of the current MR-CSI for the inversion. As noted earlier (section 6.3), this author has attempted the creation of a FEM-based CSI solver, but it currently does not provide acceptable inversion results and work is on-going. However, an FEM-based DBIM solver has been implemented by another member of our group [3] and is outlined in [99]. It is based on the DBIM code utilized in chapters 3 and 4 earlier in this work. Instead of an integral equation based solver, the code utilizes the FEM method for the forward solver at each iteration, allowing the incorporation of the antenna elements into the Green's function operator of the inversion.

Inversion results obtained using this technique for a rectangular dielectric target of dimensions $0.18\lambda \times 0.54\lambda$ (2×6 cm) for three different target positions are shown in figures 7.23, 7.24, and 7.25. The first inversion, Fig. 7.23 shows the dielectric target centered in the chamber. The permittivity of the target was measured to be $\epsilon_r = 2.6 - j0.12$ at 2.7 GHz. In the FEM-DBIM reconstruction, the overall dimensions of the object and its position in the center of the chamber is fairly well reconstructed. The real part of the permittivity is undershot slightly (2.1 instead of 2.6), and the edges of the object are blurred into an hour-glass type shape. Additionally, the target appears lossless, with only a few artifacts appearing in $Im(\epsilon_r)$. The most significant

[3] Puyan Mojabi

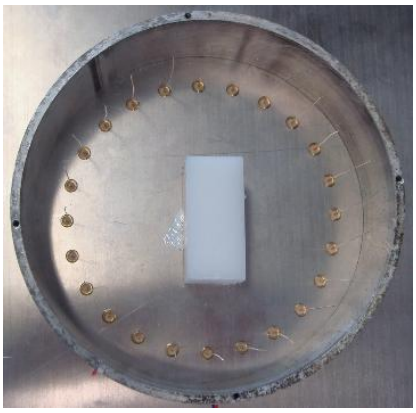

(a)

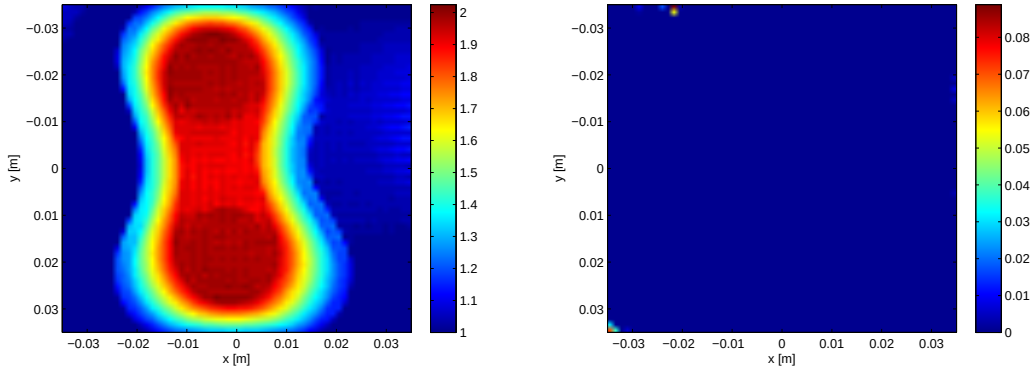

(b) (c)

Fig. 7.23: Experimental Inversion of enclosed MWT data with the FEM-DBIM code. (a) shows the physical scatterer, (b) shows $Re(\epsilon_r)$, and (c) shows $-Im(\epsilon_r)$. The object edges are blurred, but the overall shape is clear. The measured permittivity of the target at 2.7 GHz was $\epsilon_r = 2.6 - j0.12$.

(a)

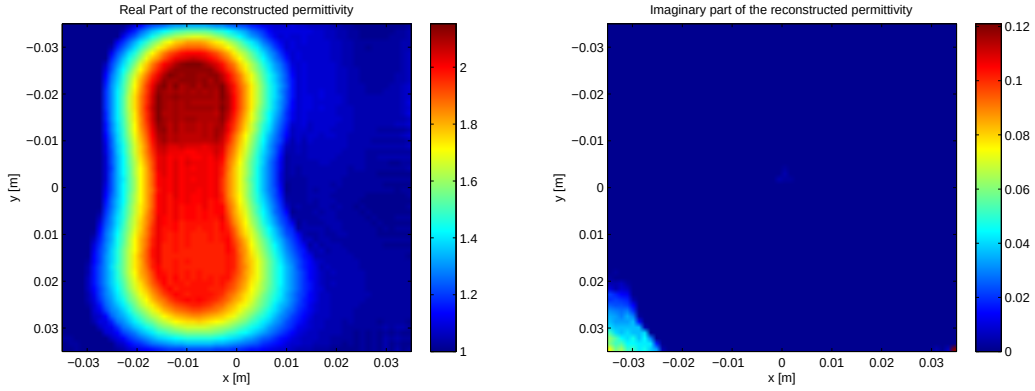

(b) (c)

Fig. 7.24: Experimental Inversion of enclosed MWT data with a shifted scatterer. (a) shows the physical scatterer, (b) shows $Re(\epsilon_r)$, and (c) shows $Im(\epsilon_r)$. The measured permittivity of the target at 2.7 GHz was $\epsilon_r = 2.6 - j0.12$.

area of error is in the center of the scatterer (i.e., the hour-glass shape).

In order to ensure that the inversion is capable of 'following' the object around the enclosure, we have performed two other experimental inversions with the same scattering object. For the first test, shown in Fig. 7.24, we moved the object away from the center of enclosure. In this case, the inversion is very similar, however the permittivity of the object is closer to the measured value (≈ 2.2), and the edges

more straight. Interestingly, the edge farther away from the center of the chamber is straighter than the edge tangential to the center of the chamber.

The third experimental test involved rotating the dielectric phantom at approximately a 45° angle from the first measurement, while keeping the dielectric object centered. These results are shown in Fig. 7.25. The real part of the reconstruction shows a value for the dielectric constant which is quite close to the actual value (2.4). However, there is an artifact which significantly overshoots the measured value of the dielectric constant for the imaginary part of the reconstruction (peak value -0.4 instead of -0.12). This error is located entirely in the center of the domain.

Due to the errors near the center of the domain for this phantom, we speculate that at this frequency and for this particular scatterer, there exists a null in the total fields at the center of the domain. When there are no fields present in a particular part of a scatterer, then the contrast χ may take on any value without affecting the scattered fields on the measurement surface S. This speculation is based on the fact that when the scatterer is in the center of the domain (Figs. 7.23 and 7.25), there is a strong 'hour-glass' shape, which is reduced when the object is not in the center of the inversion domain (Fig. 7.24). Further evidence comes from the lossy artifact found in Fig. 7.25. The possible existence of field nulls such as this emphasizes that inversions inside of conducting enclosures should be done at multiple frequencies.

(a)

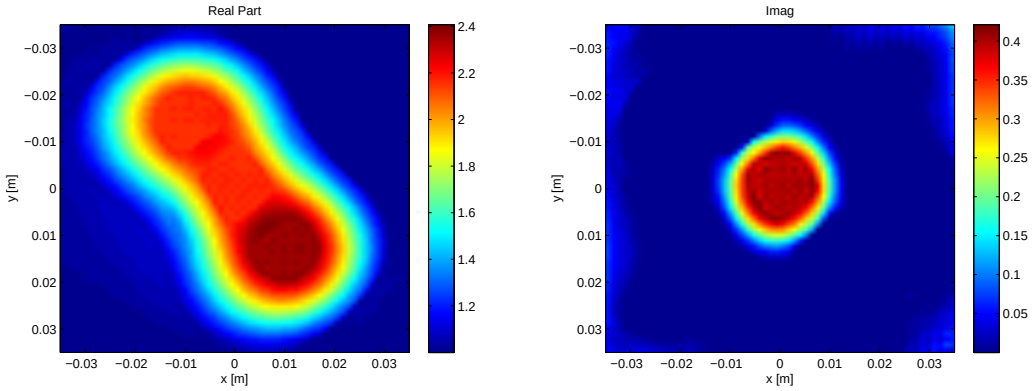

(b) (c)

Fig. 7.25: Experimental Inversion of enclosed MWT data with a rotated scatterer. (a) shows the physical scatterer, (b) shows $Re(\epsilon_r)$, and (c) shows $Im(\epsilon_r)$. The measured permittivity of the target at 2.7 GHz was $\epsilon_r = 2.6 - j0.12$.

7.4 Experimental MWT Conclusions

Through the construction of an ultra-wideband open-region MWT prototype, we have shown quantitative inversions from a multi-antenna system with a free-space background. The results show that (a) the collection of invertible multi-frequency data in multi-antenna environment is possible with a simple calibration procedure, as long as certain frequencies are avoided, and that (b) inversion images are improved by the use of this multi-frequency data. Furthermore, we have devised a simple method, based on S_{ii} measurements, of avoiding the frequencies where the antenna coupling is too large for effective imaging, and utilized this method successfully in a complicated multi-antenna environment.

For experimental MWT inside of a conducting enclosure with a free-space background, we have shown that experimental quantitative inversion is possible only by taking into account the actual field distribution in the inversion algorithm. In particular, for reasonable results, we have found that (i) the effects of the active and non-active antennas must be taken into account in the Green's function, and cannot be removed via a simple calibration procedure, and (ii) even with a simple antenna model, only certain frequencies may be utilized for 2D inversion. These can be found via comparison of 2D modes with full-wave solutions of the fields inside the enclosure.

8. CONCLUSIONS AND FUTURE WORK

True education means fostering the ability to be interested in something.
Sumio Iijima

In this work, we have described research involved in the understanding, implementation and improvements to quantitative MWT. Further, we have presented preliminary results from both open-region and conductor-enclosed microwave tomography systems. From these results, we have drawn the following conclusions:

- The imaging algorithms for the inverse scattering problem with the scalar Helmholtz equation are reasonably mature, with two classes of optimization based inversion techniques dominating: Gauss Newton/DBIM based techniques, and the CSI method. In particular, these two methods provide similar inversion results with similar computational resources. However, the use of the physical regularizer in the CSI method avoid the process of regularization parameters selection that complicates the use of the DBIM method.

- The use of a differential implementation of the integral equation formulation of the inverse problem, rather than an integral implementation based method is

recommended, for two main reasons: (i) when *a-priori* information about the scatterer is known, its use as an inhomogeneous background (i.e., computational reduction of contrast) may improve the inversion result over the use of this information as an initial guess to the inversion. The incorporation of this information as an inhomogeneous background is much easier with a differential based solver. (ii) Modeling static inhomogeneities in the inversion region, such as antenna elements, is much easier with a differential based solver.

- The MWT problem may be formulated with an enclosed conducting boundary, and imaging within such an enclosure is possible [34]. The enclosed-type system has many possible advantages, e.g., will increase signal-to-noise ratio, and will also induce significant changes in the Green's function of the problem. Experimental experience has shown that for the enclosed problem it is much more difficult to use simple calibration techniques and better system models and/or calibration methods are required for effective imaging. Effort put into this problem is worthwhile, as this sensitivity should be advantageous once the enclosed MWT system is properly modeled and calibrated.

- The use of multi-frequency data can significantly improve MWT imaging results, and ultra-wideband open-region systems utilizing simple calibration procedures can provide satisfactory inversion results, provided certain frequencies are avoided.

- Further improvements to MWT, for both open-region and conductor-enclosed type systems, will require the modeling of MWT system features inside of the inverse solver.

We do note that at the end of this work, we are still not able to definitively answer the ultimate question with regards to biomedical MWT: can it compete with and/or outperform existing medical imaging modalities? The research outlined in this dissertation shows that there is still much room for improvement in the MWT technology, and we remain optimistic that MWT will become a widely-used clinical imaging modality.

8.1 Future Work

The main challenge remaining to make MWT a competitive biomedical imaging modality is the lower resolution of current MWT systems as compared to MRI, ultrasound, and x-ray CT (in this context, we define resolution as the minimum size of tumor which may be detected). The lower resolution of MWT is directly linked to the relatively large wavelength of the microwaves utilized. There is, however, no known theoretical limit to the spatial resolution obtainable from MWT; image resolution as low as $\lambda/4$ has been obtained for near-field imaging systems and it has been suggested that the true resolution limit is governed by the achievable signal-to-noise ratio of the measurements, and not the wavelength (see, e.g., low-frequency impedance tomography systems). Super-resolution, i.e., resolution of targets smaller

than $\lambda/2$, has been claimed for non-linear electromagnetic inverse problems, and relies on the availability of near-field measurements of the evanescent vector-fields [111, 112]. Further gains in resolution will thus depend on the measurement of low-noise, near-field radiation, probably of full-vector fields. We again emphasize that noise in an MWT system anything that does not match the assumed model: errors with regards to the 2D scalar assumption, errors with regards to other antennas present, reflections from matching field boundaries or other equipment in room, etc.

The elimination of these system modeling errors, the improvement of the signal-to-noise ratio, and accurate methods of near-field measurement are closely tied together; they will ultimately require good models of the MWT system under use. The research presented in this dissertation will go some way towards solving this: the use of differential solvers will allow the MWT system to be better modeled, thus improving the signal-to-noise ratio, and the computational reduction of the contrast has been shown to improve imaging when accurate *a-priori* information is available (although we recognize that the question of possible resolution enhancement with this method has not been answered, we are optimistic that this will occur). Further, through the use of conductor-enclosed MWT systems, we should be able to detect evanescent fields more easily than open-region systems, improve the ultimately achievable signal-to-noise ratio, eliminate the modeling errors of the finite-matching fluid, and eliminate exterior sources of noise. Even if conductor-enclosed MWT is ultimately shown not to have any of the other theoretical advantages over open-region systems suggested in chapter

6, the improvements listed here justify further research efforts.

In particular, in order to improve the art of MWT, effort is warranted in the following areas:

- First, the resolution for MWT systems should be properly defined (the definition will depend on the desired application), so that we may have an objective standard to improve upon.

- Better antenna modeling inside of the inverse solver should be investigated for both open-region and conductor-enclosed systems, including the possibility of fully modeling the antennas in the inverse solver.

- In order to gain from the experience of others in near-field measurement, the literature on near-field scanning systems used in electromagnetic compatability (EMC) studies should be investigated, and results from this area applied to multi-antenna near-field MWT data collection.

- The use of *a-priori* information as a computational background should be investigated and tested to determine if its use may improve resolution in experimental MWT systems.

- To eliminate the modeling errors associated with the 2D scalar assumption, full-vector 3D inversion with a differential solver should be implemented.

- Potential advantages of enclosed-chamber imaging should continue to be in-

vestigated, and if possible, a detailed analysis of the convergence of inversion algorithms inside this type of system should be completed.

- Experimental MWT must continue to be investigated at all steps of research, as many critical system issues simply cannot be dealt with by simulation alone.

Appendices

Appendix A

LINEAR INVERSE SCATTING AND FOURIER IMAGING

As discussed in Chapter 3, a common way of solving the inverse scattering problem is to linearize it by making some assumptions, then solving the resultant linear ill-posed problem by manipulating/making further assumptions about the equations into the form of a Fourier Transform. We discuss one of these techniques here.

A.1 Linearized Solutions to the Inverse Scattering Problem

The Born Approximation [132] provides the simplest and fastest way to solve the inverse scattering problem. With careful implementation, real-time imaging is possible. However, the Born approximation is a very restrictive approximation to make, in that the vast majority of interesting inverse scattering problems do not satisfy the approximation.

Explicitly, the Born approximation assumes that the solution to the domain equation (2.37) is:

$$u(\mathbf{r},\omega) \approx u^{\text{inc}}(\mathbf{r},\omega) \qquad \mathbf{r} \in D. \tag{A.1}$$

Simply put, the total field inside the imaging domain is approximated by the incident field. The Born approximation, by solving for one of the two unknowns, linearizes the inverse scattering problem. The data equation then becomes

$$\tilde{u}^{\text{sct}}(\mathbf{r},\omega) = -\int_D k_b^2 G(\mathbf{r}_{rx},\mathbf{r}';\omega)\chi u^{\text{inc}} d\mathbf{r}' \qquad \mathbf{r}_{rx} \notin D \tag{A.2}$$

where χ is now the only unknown. In this case, the solution of (A.2) is now the solution of a linear first-kind Fredholm integral equation, with a kernel given by $k_b^2 G u^{\text{inc}}$, and we may employ all of the theory associated with problems of these type (see [41] and [47]). Despite the fact that the problem is now linear, it is important to realize that it still remains ill-posed (in the sense that there exists an infinite number of solutions and the output is not a continuous function of the input).

A.1.1 Fourier Imaging Techniques

One method of solving the linearized inverse scattering problem is through Fourier-based imaging techniques. In a process similar to that of x-ray CT [133], the equations are manipulated until they are in the form of a Fourier Transform, then the inversion is carried out by an inverse Fourier Transform. For MWT, these techniques are only useful if the measurement set-up allows for wide-band multiple-frequency experiments. Effectively, the extra data are needed to fill 'k-space' to an adequate level to perform the inverse Fourier Transform. We outline one such possibility for Fourier imaging

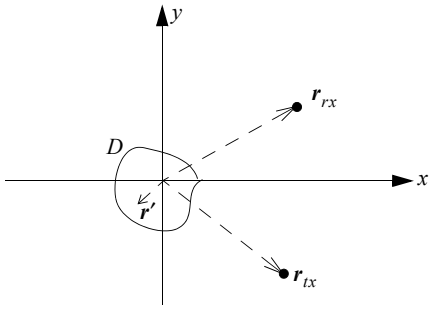

Fig. A.1: Fourier Imaging schematic. A point source is located at $\mathbf{r}_{tx}$ radiates an incident field to the scatterer located within D. The scattered fields are measured at the position $\mathbf{r}_{rx}$.

here, although with slightly different assumptions, slightly different Fourier imaging algorithms may be derived (see, e.g., [134]).

The diagram associated with this Fourier inversion algorithm is shown in Fig. A.1. If we assume that the material properties vary in 2 dimensions, while the fields radiate in 3 dimensions (which is known as the 2.5D model), and maintain the $e^{j\omega t}$ time dependency, then the Green's function is given by

$$G(\mathbf{r}, \mathbf{r}') = \frac{e^{-jk_b|\mathbf{r}-\mathbf{r}'|}}{4\pi\,|\mathbf{r}-\mathbf{r}'|}, \tag{A.3}$$

where k_b is the background wave-number. For the purposes of Fourier imaging techniques, we assume that the background is lossless and k_b is constant. We further assume that the material parameters are also lossless (i.e. $Im(\chi) = 0$). Let the source be a point source, located at the position $\mathbf{r}_{tx}$, in which case the incident field is the Green's function. Additionally, let the scattered field be measured at position $\mathbf{r}_{rx}$.

Under the Born approximation, the data equation becomes

$$\tilde{u}^{\mathrm{sct}}(\mathbf{r},\omega) = \frac{k_b^2}{4\pi}\int_D \frac{e^{-jk_b|\mathbf{r}_{rx}-\mathbf{r}'|}}{|\mathbf{r}_{rx}-\mathbf{r}'|}\frac{e^{-jk_b|\mathbf{r}_{tx}-\mathbf{r}'|}}{|\mathbf{r}_{tx}-\mathbf{r}'|}\chi(\mathbf{r}')d\mathbf{r}' \tag{A.4}$$

Making the standard far-field approximation, when $|\mathbf{r}| >> |\mathbf{r}'|$: $|\mathbf{r}-\mathbf{r}'| = |\mathbf{r}| + \hat{\mathbf{r}}\cdot\mathbf{r}'$ in the numerator, and $|\mathbf{r}-\mathbf{r}'| = |\mathbf{r}|$ in the denominator, we may write

$$\tilde{u}^{\mathrm{sct}}(\mathbf{r},\omega) = \frac{k_b^2 e^{-jk_b|\mathbf{r}_{rx}|}e^{-jk_b|\mathbf{r}_{tx}|}}{(4\pi)^2\,|\mathbf{r}_{rx}|\,|\mathbf{r}_{tx}|}\int_D e^{-jk_b\hat{\mathbf{r}}_{rx}\cdot\mathbf{r}'}e^{-jk_b\hat{\mathbf{r}}_{tx}\cdot\mathbf{r}'}\chi(\mathbf{r}')d\mathbf{r}'. \tag{A.5}$$

With a little manipulation, we arrive at

$$\frac{(4\pi)^2\,|\mathbf{r}_{rx}|\,|\mathbf{r}_{tx}|\,\tilde{u}^{\mathrm{sct}}(\mathbf{r}_{rx},\omega)e^{jk_b|\mathbf{r}_{rx}|}e^{jk_b|\mathbf{r}_{tx}|}}{k_b^2} = \int_D e^{-jk_b\left[-((\hat{\mathbf{r}})_{rx}+\hat{\mathbf{r}}_{tx})\cdot\mathbf{r}'\right]}\chi(\mathbf{r}')d\mathbf{r}'. \tag{A.6}$$

If we denote the 2-D Spatial Fourier Transform of the contrast χ as $\tilde{\chi}$, with spatial Fourier coordinates $\mathbf{k} = (k_x, k_y)$ then we may write

$$\tilde{\chi}\left(\mathbf{k} = k_b(\hat{\mathbf{r}}_{rx}+\hat{\mathbf{r}}_{tx})\right) = \frac{(4\pi)^2\,|\mathbf{r}_{rx}|\,|\mathbf{r}_{tx}|\,\tilde{u}^{\mathrm{sct}}(\mathbf{r}_{rx},\omega)e^{jk_b|\mathbf{r}_{rx}|}e^{jk_b|\mathbf{r}_{tx}|}}{k_b^2}. \tag{A.7}$$

Equation (A.7) gives a method of determining the values of the Fourier transform of χ (in the k-space domain) by varying the frequency, receiver position, and transmitter position. If enough values of the contrast are determined the k-space, then an inverse Fourier transform may be taken to determine the contrast χ (up to some maximum spatial frequency). To generate enough values of $\tilde{\chi}$ in k-space, many combinations of

receiver/transmitter pairs, often combined with a large number of frequencies must be utilized. In addition, the data collection will rarely provide evenly spaced data in k-space, and the data must be interpolated to an even grid before the FFT may be utilized [135].

For a further discussion how radar techniques and seismic migration algorithms, while appearing to not utilize the full inverse problem, actually make use of the Born approximation and then proceed to solve the inverse scattering problem, see [136].

Appendix B

FURTHER DETAILS ON CONTRAST SOURCE INVERSION

B.1 Fréchet Derivatives

In this brief section, we give the definition of the Fréchet derivative (see [137]). The Fréchet derivative measures the variation of the functional $F(a)$ with respect to a small variation ϵ along a direction $b(\mathbf{r})$ with respect to the function $a(\mathbf{r})$.

Let $F(a)$ be some functional depending on a scalar function $a(\mathbf{r})$ which can be written as a continuous norm $\| \cdot \|$ generated by a continuous inner product $< \cdot, \cdot >$. Then the Fréchet derivative is written as:

$$\frac{\partial F(a)}{\partial a} = \lim_{\epsilon \to 0} \frac{F(a + \epsilon b) - f(a)}{\epsilon} = < c, b >, \quad \epsilon \in \Re, \tag{B.1}$$

where we may identify $c(\mathbf{r})$ with the gradient of F with respect to the function $a(\mathbf{r})$, i.e.,

$$\nabla_a F = c(\mathbf{r}). \tag{B.2}$$

We may do this as the gradient provides the direction in which the variation of a

functional is maximal. This method allows for the calculation of the gradients required for the Contrast Source Inversion method.

B.2 Initialization of CSI Method

The initialization expression for the contrast sources of the CSI method is derived here. We may solve (3.26), repeated here:

$$F^{\text{data}}(w_j) = \left\| \tilde{u}_j^{\text{sct}} - \mathcal{G}_{\mathcal{S}} \left\{ w_j \right\} \right\|_S^2 \tag{B.3}$$

in the least-squares sense by solving

$$\mathcal{G}_{\mathcal{S}}^* \mathcal{G}_{\mathcal{S}}(w_j) = \mathcal{G}_{\mathcal{S}S}^* \tilde{u}_j^{\text{sct}}, \tag{B.4}$$

Furthermore, the mathematical problem of solving (B.4) is ill-posed. Thus, we apply Tikhonov regularization:

$$\left[\mathcal{G}_{\mathcal{S}}^* \mathcal{G}_{\mathcal{S}} + \upsilon^2 I \right] w_j = \mathcal{G}_{\mathcal{S}}^* \mathcal{G}_{\mathcal{S}} \tilde{u}_j^{\text{sct}}, \tag{B.5}$$

where I is the identity matrix. The basic back-propagation guess may be arrived at by letting $\upsilon \to \infty$ [41]. Thus, the back-propagated solution is

$$w_j^{bp_{init}} = \frac{1}{\upsilon^2} \mathcal{G}_{\mathcal{S}}^* \tilde{u}_j^{\text{sct}}. \tag{B.6}$$

Since the $\frac{1}{v^2}$ is a constant, it is dropped [41], and we arrive at

$$w_j^{\mathrm{bp}_{init}} = \mathcal{G}_{\mathcal{S}}^* \tilde{u}_j^{\mathrm{sct}}. \tag{B.7}$$

which is the the over-regularized, or back-propagated solution.

The initial back-propagation estimate is now taken as a search direction, and we aim to find the α which minimizes the functional

$$F^{\mathrm{data}}(\alpha) = \left\| \tilde{u}_j^{\mathrm{sct}} - \alpha \mathcal{G}_{\mathcal{S}} w_j^{bp_{init}} \right\|_S^2 = \left\| \tilde{u}^{\mathrm{sct}} - \alpha \mathcal{G}_{\mathcal{S}} \mathcal{G}_{\mathcal{S}}^* \tilde{u}_j^{\mathrm{sct}} \right\|_S^2. \tag{B.8}$$

F^{data} is equal to

$$F^{\mathrm{data}}(\alpha) = \left\| \tilde{u}_j^{\mathrm{sct}} \right\|_S^2 - 2\alpha Re \left\langle \tilde{u}_j^{\mathrm{sct}}, \mathcal{G}_{\mathcal{S}} \mathcal{G}_{\mathcal{S}}^* \tilde{u}_j^{\mathrm{sct}} \right\rangle_S + \alpha^2 \left\| \mathcal{G}_{\mathcal{S}} \mathcal{G}_{\mathcal{S}}^* \tilde{u}_j^{\mathrm{sct}} \right\|_S^2. \tag{B.9}$$

To find the minimum of this, we find

$$\frac{\partial F}{\partial \alpha} = 0 \tag{B.10}$$

which results in

$$\alpha = \frac{Re \left\langle \tilde{u}_j^{\mathrm{sct}}, G_S G_S^* \tilde{u}_j^{\mathrm{sct}} \right\rangle_S}{\left\| G_S G_S^* \tilde{u}_j^{\mathrm{sct}} \right\|_S^2}. \tag{B.11}$$

By using the definition of the adjoint operator, we arrive at

$$\alpha = \frac{\left\|\mathcal{G}_{\mathcal{S}}^{*}\tilde{u}_{j}^{\mathrm{sct}}\right\|_{S}^{2}}{\left\|\mathcal{G}_{\mathcal{S}}\mathcal{G}_{\mathcal{S}}^{*}\tilde{u}_{j}^{\mathrm{sct}}\right\|_{S}^{2}}, \tag{B.12}$$

and thus

$$w_{j}^{\mathrm{bp}} = \frac{\left\|\mathcal{G}_{\mathcal{S}}^{*}\tilde{u}_{j}^{\mathrm{sct}}\right\|_{D}^{2}}{\left\|\mathcal{G}_{\mathcal{S}}\mathcal{G}_{\mathcal{S}}^{*}\tilde{u}_{j}^{\mathrm{sct}}\right\|_{S}^{2}}\mathcal{G}_{\mathcal{S}}^{*}\tilde{u}_{j}^{\mathrm{sct}}, \tag{B.13}$$

which is the solution given in [64] and [58]. Note that because we have performed a minimization over α this solution is at the least a local minimum of the data equation.

Appendix C

DERIVATION OF ENCLOSED GREEN'S FUNCTION

Herein, we derive the solution for the coefficients of the p function utilized in the enclosed Green's function section of the thesis (chapter 6). We are concerned with solving the 2D differential equation

$$\begin{aligned} \nabla^2 p(\mathbf{r},\mathbf{r}') + k^2 p(\mathbf{r},\mathbf{r}') &= 0 \qquad \mathbf{r} \in T \\ p(\mathbf{r},\mathbf{r}') &= -g_{fs}(\mathbf{r},\mathbf{r}') \qquad \mathbf{r} \in \Omega \end{aligned} \tag{C.1}$$

where Ω is a circle of radius a. We first introduce the cylindrical coordinates $\mathbf{r} = (r, \theta)$, and write the Helmholtz equation in these cylindrical coordinates,

$$\begin{aligned} \frac{\partial^2 p}{\partial r^2} + \frac{1}{r}\frac{\partial p}{\partial r} + \frac{1}{r^2}\frac{\partial^2 p}{\partial \theta^2} + k^2 p = 0 \qquad & 0 < r < a,\ -\pi < \theta < \pi \\ p(a,\theta,\mathbf{r}') = -g_{fs}(a,\theta,\mathbf{r}'). & \end{aligned} \tag{C.2}$$

Assuming that p may be written as

$$p(r,\theta) = R(r)H(\theta), \tag{C.3}$$

we note that

$$\frac{R''}{R} + \frac{1}{r}\frac{R'}{R} + \frac{1}{r^2}\frac{H''}{H} + k^2 = 0, \tag{C.4}$$

where prime and double prime denote first and second derivatives respectively. Due to the fact that R and H are independent, we note

$$r^2\frac{R''}{R} + r\frac{R'}{R} + r^2k^2 = -\frac{H''}{H} = \alpha = \text{constant}, \tag{C.5}$$

which results in two separated ordinary differential equations (ODE), solvable through the application of the boundary and periodicity conditions. The first ODE is given by

$$H'' + \alpha H = 0, \tag{C.6}$$

and the periodicity requirement gives the conditions

$$\begin{aligned} H(-\pi) &= H(\pi) \\ H'(-\pi) &= H'(\pi). \end{aligned} \tag{C.7}$$

Equations (C.6) and (C.7) constitute a Sturm-Louiville system [118] with eigenvalues

$$\alpha = n^2 \tag{C.8}$$

where n is a non-negative integer, with corresponding orthonormal eigenfunctions

$$\begin{aligned} &\frac{1}{\sqrt{2\pi}} && n = 0 \\ &\frac{1}{\sqrt{\pi}} cos(n\theta) + \frac{1}{\sqrt{\pi}} \sin(n\theta) && n > 0. \end{aligned} \tag{C.9}$$

The remaining differential equation is

$$r^2 R'' + rR' + \left(r^2 k^2 - n^2\right) R = 0. \tag{C.10}$$

Equation (C.10) is Bessel's equation of order n. We know that the solution to this equation must be a summation of the Bessel functions of the form:

$$J_n(kr), Y_n(kr), H_n^{(1)}(kr), H_n^{(2)}(kr). \tag{C.11}$$

where $J_n(kr)$ is the n^{th} order Bessel function of the first kind, $Y_n(kr)$ is the n^{th} order Bessel function of the second kind, and $H_n^{(1)}(kr)$ and $H_n^{(2)}(kr)$ are the n^{th} order Hankel functions of the first and second kind, respectively. However, since we know the

solution p is non-singular inside the PEC region, solutions to must be of the form:

$$R_n(r) = J_n(kr), \tag{C.12}$$

as $J_n(kr)$ is the only solution of Bessel's equation which is non-singular.

Thus, general solutions of the form $p(a, \theta; \mathbf{r}') = R(r)H(\theta)$ may be now written as

$$p(a, \theta, \mathbf{r}') = \frac{A_0}{\sqrt{2\pi}} J_0(kr) + \sum_{n=1}^{\infty} \left(A_n J_n(kr) \frac{\cos(n\theta)}{\sqrt{\pi}} + B_n J_n(kr) \frac{\sin(n\theta)}{\sqrt{\pi}} \right), \tag{C.13}$$

where the coefficients, A_0, A_n, and B_n are chosen to satisfy the boundary conditions, namely

$$p(a, \theta, \mathbf{r}') = -g_{fs}(a, \theta, \mathbf{r}'), \tag{C.14}$$

or

$$p(a, \theta, \mathbf{r}') = \frac{A_0}{\sqrt{2\pi}} J_0(ka) + \sum_{n=1}^{\infty} \left(A_n J_n(ka) \frac{\cos(n\theta)}{\sqrt{\pi}} + B_n J_n(ka) \frac{\sin(n\theta)}{\sqrt{\pi}} \right). \tag{C.15}$$

Making use of the orthonormal nature of the eigenfunctions of $H(\theta)$, we multiply both sides of (C.15) by $1/\sqrt{2\pi}$, and integrate from $\theta = -\pi$ to $\theta = \pi$, and arrive at

$$A_0 = \frac{-1}{\sqrt{2\pi} J_0(ka)} \int_{-\pi}^{\pi} g_{fs}(a, \theta, \mathbf{r}') d\theta. \tag{C.16}$$

To determine A_n, we multiply both sides of (C.15) by $\cos(m\theta)/\sqrt{\pi}$ and integrate over

θ, which results in

$$A_n = \frac{-1}{\sqrt{\pi} J_0(ka)} \int_{-\pi}^{\pi} g_{fs}(a, \theta, \mathbf{r}') \cos(n\theta) d\theta. \tag{C.17}$$

And by similar argument:

$$B_n = \frac{-1}{\sqrt{\pi} J_0(ka)} \int_{-\pi}^{\pi} g_{fs}(a, \theta, \mathbf{r}') \sin(n\theta) d\theta. \tag{C.18}$$

These two integrals may be derived in closed form by considering the identity ([120], section 11.4.2)

$$\begin{aligned} H_0^{(2)}(k\,|\mathbf{r} - \mathbf{r}'|) \;\; = \;\; & \sum_{m=-\infty}^{m=\infty} J_m(kr) H_m^{(2)}(kr') e^{jm(\theta-\theta')} \qquad r \le r' \\ & \sum_{m=-\infty}^{m=\infty} J_m(kr') H_m^{(2)}(kr) e^{jm(\theta-\theta')} \qquad r \ge r', \end{aligned} \tag{C.19}$$

where r, r', and θ, θ' are the cylindrical coordinates for $\mathbf{r}$ and $\mathbf{r}'$ respectively. For the integrals in (C.17) and (C.18), $r > r'$, and we may write

$$A_n = \frac{-1}{4j\sqrt{\pi} J_n(ka)} \int_{-\pi}^{\pi} \left(\sum_{m=-\infty}^{m=\infty} J J_m(kr') H_m^{(2)}(kr) e^{jm(\theta-\theta')} \right) \cos(n\theta) d\theta, \tag{C.20}$$

which equals

$$A_n = \frac{-1}{4j\sqrt{\pi} J_n(ka)} \left(\sum_{m=-\infty}^{m=\infty} J_m(kr') H_m^{(2)}(kr) e^{-jm\theta'} \right) \int_{-\pi}^{\pi} e^{jm\theta} \cos(n\theta) d\theta, \tag{C.21}$$

and since

$$\int_{-\pi}^{\pi} e^{jm\theta} \cos(n\theta) d\theta = \pi \qquad \text{if } |n| = m \tag{C.22}$$

and is 0 otherwise, A_n is equal to the expression given in (34). The derivation for B_n proceeds in an analogous manner.

REFERENCES

[1] A. Abubakar, T. Habashy, V. Druskin, L. Knizhnerman, and D. Alumbaugh, "2.5D forward and inverse modeling for interpreting low-frequency electromagnetic measurements," *Geophysics*, vol. 73, no. 4, 2008.

[2] E. Marengo, R. Hernandez, and H. Lev-Ari, "Intensity-only signal subspace-based imaging," *Journal of the Optical Society of America A*, vol. 24, pp. 3619–3635, 2007.

[3] P. Meaney, M. Fanning, D. Li, S. Poplack, and K. Paulsen, "A clinical prototype for active microwave imaging of the breast," *IEEE Transactions on Microwave Theory and Techniques*, vol. 48, no. 11, pp. 1841–1853, Nov 2000.

[4] R. Lencrerot, A. Litman, H. Tortel, and J.-M. Geffrin, "Imposing zernike representation for imaging two-dimensional targets," *Inverse Problems*, vol. 25, p. 035012 (18pp), 2009.

[5] A. Fhager, P. Hashemzadeh, and M. Persson, "Reconstruction quality and spectral content of an electromagnetic time-domain inversion algorithm," *IEEE Transactions on Biomedical Engineering*, vol. 53, no. 8, pp. 1594–1604, Aug. 2006.

[6] C. Gilmore, P. Mojabi, A. Zakaria, M. Ostadrahimi, C. Kaye, S. Noghanian, L. Shafai, S. Pistorius, and J. LoVetri, "A wideband microwave tomography system with a novel frequency selection procedure," *(In Press) IEEE Transactions on Biomedical Engineering*, 2009.

[7] S. Semenov, A. Bulyshev, A. Abubakar, V. Posukh, Y. Sizov, A. Souvorov, P. van den Berg, and T. Williams, "Microwave-tomographic imaging of the high dielectric-contrast objects using different image-reconstruction approaches," *IEEE Transactions on Microwave Theory and Techniques*, vol. 53, no. 7, pp. 2284–2294, July 2005.

[8] American Cancer Society, *Cancer facts and figures 2007.* Atlanta, GA: American Cancer Society, 2007.

[9] E. Bond, X. Li, S. C. Hagness, and B. D. van Veen, "Microwave imaging via space-time beamforming for early detection of breast cancer," *IEEE Transactions on Antennas and Propagation*, vol. 51, no. 8, pp. 1690–1705, August 2003.

[10] S. Chaudhary, R. Mishra, A. Swarup, and et al., "Dielectric properties of normal and malignant human breast tissues at radiowave and microwave frequencies," *Ind Journal Biochemical Biophysics*, pp. 2176–2179, 1984.

[11] W. Joines, Y. Zhang, C. Li, and et al., "The measured electrical properties of normal and malignant human tissues from 50 to 900 mhz," *Medical Physics*, vol. 21, pp. 547–550, 1994.

[12] E. Fear, P. Meaney, and M. Stuchly, "Microwaves for breast cancer detection?" *IEEE Potentials*, vol. 22, no. 1, pp. 12–18, Feb/Mar 2003.

[13] P. Kosmas and C. M. Rappaport, "FDTD-based time reversal for microwave breast cancer detection–localization in three dimensions," *IEEE Transactions on Microwave Theory and Techniques*, vol. 54, no. 4, pp. 1921–1927, June 2006.

[14] E. C. Fear, X. Li, S. C. Hagness, and M. Stuchly, "Confocal microwave imaging for breast cancer detection: localization of tumors in three dimensions," *IEEE Transactions on Biomedical Engineering*, vol. 49, no. 8, pp. 812–822, Aug 2002.

[15] J. M. Sill and E. C. Fear, "Tissue sensing adaptive radar for breast cancer detection–experimental investigation of simple tumor models," *IEEE Transactions on Microwave Theory and Techniques*, vol. 53, no. 11, pp. 3312–3319, November 2005.

[16] X. Li and S. C. Hagness, "A confocal microwave imaging algorithm for breast cancer detection," *IEEE Microwave Wireless Comp. Letters*, vol. 11, no. 3, pp. 130–132, March 2001.

[17] J. D. Shea, P. Kosmas, S. C. Hagness, and B. D. van Veen, "Three-dimensional microwave breast imaging: a bounded, multi-frequency inverse scattering solution on a uniform voxel mesh," in *Proc. XXIX General Assembly of International Union of Radio Science*, Chicago, USA, August 2008.

[18] P. Kosmas, J. Shea, B. V. Veen, and S. Hagness, "Three-dimensional microwave imaging of realistic breast phantoms via an inexact gauss-newton algorithm," in *IEEE Antennas and Propagation Symposium*, San Diego, USA, 2008.

[19] T. Rubæk, P. M. Meaney, P. Meincke, and K. D. Paulsen, "Nonlinear microwave imaging for breast-cancer screening using Gauss-Newton's method and the CGLS inversion algorithm," *IEEE Transactions on Antennas and Propagation*, vol. 55, no. 8, pp. 2320–2331, Aug 2007.

[20] A. Bulyshev, S. Semenov, A. Souvorov, R. Svenson, A. Nazarov, Y. Sizov, and G. Tatsis, "Computational modeling of three-dimensional microwave tomography of breast cancer," *IEEE Transactions on Biomedical Engineering*, vol. 48, no. 9, pp. 1053–1056, Sept. 2001.

[21] R. Nilavalan, A. Gbedemah, I. Craddock, X. Li, and S. Hagness, "Numerical investigation of breast tumour detection using," *Electronics Letters*, vol. 39, no. 25, pp. 1787–1789, Dec. 2003.

[22] T. Williams, E. Fear, and D. Westwick, "Tissue sensing adaptive radar for breast cancer detection-investigations of an improved skin-sensing method," *IEEE Transactions on Microwave Theory and Techniques*, vol. 54, no. 4, pp. 1308–1314, June 2006.

[23] M. Lazebnik, D. Popovic, L. McCartney, C. B. Watkins, M. J. Lindstrom, J. Harter, S. Sewall, T. Ogilvie, A. Magliocco, T. M. Breslin, W. Temple, D. Mew, J. H. Booske, M. Okoniewski, , and S. C. Hagness, "A large-scale study of the ultrawideband microwave dielectric properties of normal, benign, and malignant breast tissues obtained from cancer surgeries," *Physics in Medicine and Biology*, vol. 52, pp. 6093–6115, 2007.

[24] M. Lazebnik, L. McCartney, D. Popovic, C. B. Watkins, M. J. Lindstrom, J. Harter, S. Sewall, A. Magliocco, J. H. Booske, M. Okoniewski, and S. C. Hagness, "A large-scale study of the ultrawideband microwave dielectric properties of normal breast tissue obtained from reduction surgeries," *Physics in Medicine and Biology*, vol. 52, pp. 2637–2657, 2007.

[25] R. J. Halter, T. Zhou, P. M. Meaney, A. Hartov, R. J. Barth Jr, K. M. Rosenkranz, W. A. Wells, C. A. Kogel, A. Borsic, E. J. Rizzo, and K. D. Paulsen, "The correlation of in vivo and ex vivo tissue dielectric properties to validate electromagnetic breast imaging: initial clinical experience," *Physiological Measurement*, vol. 30, p. S121S136, 2009, doi:10.1088/0967-3334/30/6/S08.

[26] S. Poplack, S. P. Poplack, T. D. Tosteson, W. A. Wells, B. W. Pogue, P. M. Meaney, A. Hartov, C. A. Kogel, S. K. Soho, J. J. Gibson, and K. D. Paulsen, "Electromagnetic breast imaging results of a pilot study in women with abnormal mammograms," *Radiology*, vol. 243, pp. 350–359, 2007.

[27] P. M. Meaney, M. W. Fanning, T. Raynolds, C. J. Fox, Q. Fang, C. A. Kogel, S. P. Poplack, and K. D. Paulsen, "Initial clinical experience with microwave breast imaging in women with normal mammography," *Academic Radiology*, vol. 14, pp. 207–218, 2007.

[28] Unviersity of Bristol Research News, "How do you solve a problem like MARIA?" http://bristol.ac.uk/news/2009/6169.html, February 2009, accessed May 23, 2009.

[29] M. Klemm, I. Craddock, J. Leendertz, A. Preece, and R. Benjamin, "Experimental and clinical results of breast cancer detection using UWB microwave radar," in *Antennas and Propagation Society International Symposium, 2008. AP-S 2008. IEEE*, July 2008, pp. 1–4.

[30] P.-H. Zahl, J. Mæhlen, and G. Welch, "The natural history of invasive breast cancers detected by screening mammography," *Archives of Internal Medicine*, vol. 168, no. 21, pp. 2311–2316, Nov. 2008.

[31] A. Abubakar, P. M. van den Berg, and J. J. Mallorqui, "Imaging of biomedical data using a multiplicative regularized contrast source inversion method," *IEEE Transactions on Microwave Theory and Techniques*, vol. 50, no. 7, pp. 1761–1777, July 2002.

[32] S. Y. Semenov, R. H. Svenson, V. G. Posukh, A. G. Nazarov, Y. E. Sizov, A. E. Bulyshev, A. E. Souvorov, W. Chen, J. Kasell, and G. P. Tastis, "Dielectrical spectroscopy of canine myocardium during acute ischemia and hypoxia at frequency spectrum from 100 KHz to 6 GHz," *IEEE Transactions on Medical Imaging*, vol. 21, no. 6, pp. 703–707, June 2002.

[33] C. Gilmore, P. Mojabi, and J. LoVetri, "Comparison of an enhanced distorted born iterative method and the multiplicative-regularized contrast source inversion method," *IEEE Transactions on Antennas and Propagation*, vol. 57, no. 8, pp. 2341 – 2351, August 2009.

[34] C. Gilmore and J. LoVetri, "Enhancement of microwave tomography through the use of electrically conducting enclosures," *Inverse Problems*, vol. 24, p. 035008 (21pp), 2008.

[35] ——, "Corrections and comments on 'enhancement of microwave tomography through the use of electrically conducting enclosures'," *Inverse Problems*, 2009, (submitted).

[36] C. Gilmore, A. Abubakar, W. Hu, T. Habashy, and P. van den Berg, "Microwave biomedical data inversion using the finite-difference contrast source inversion method," *IEEE Transactions on Antennas and Propagation*, vol. 57, no. 5, pp. 1528–1538, May 2009.

[37] P. Mojabi, C. Gilmore, A. Zakaria, C. Kaye, and J. LoVetri, "On microwave tomography in enclosures: abitrary enclosure shapes and further results," *Inverse Problems*, 2009, (to be submitted).

[38] R. Harrington, *Time-Harmonic Electromagnetic Fields*. New York: IEEE Press, 2001.

[39] M. Born and E. Wolf, *Principles of Optics, 7th edition*. Cambridge University Press, 1999.

[40] J.-M. Geffrin, P. Sabouroux, and C. Eyraud, "Free space experimental scattering database continuation: experimental set-up and measurement precision," *Inverse Problems*, vol. 21, pp. S117–S130, 2005.

[41] M. Oristaglio and H. Blok, *Wavefield imaging and inversion in electromagnetics and acoustics*. Course Notes TU Delft, 1995.

[42] E. A. Margengo and R. W. Ziolkowski, "On the radiating and nonradiating components of scalar, electromagnetic and weak gravitational sources," *Physical Review Letters*, vol. 83, no. 17, pp. 3346–3349, 1999.

[43] A. J. Devaney and E. Wolf, "Radiating and non-radiating classical current distributions and the fields they generate," *Physical Review D*, vol. 8, pp. 1044–1047, 1973.

[44] Hadamard, *Lectures on Cauchy's Problem in Linear Partial Differential Equations*. New Haven, CT: Yale University Press, 1923.

[45] D. Colton and R. Kress, *Inverse Acoustic and Electromagnetic Scattering Theory*. Berlin: Springer-Verlag, 1998.

[46] W. C. Chew, *Waves and Fields in Inhomogeneous Media*. IEEE Press, 1994.

[47] P. C. Hansen, *Rank-deficient and discrete ill-posed problems: Numerical aspects of linear inversion*. Philadelphia, PA: SIAM, 1998.

[48] J. Kaipio and E. Somersalo, *Statistical and Computational Inverse Problems*. Springer Science and Business Media, 2004.

[49] L. Crocco and A. Litman, "On embedded microwave imaging systems: retrievable information and design guidelines," *Inverse Problems*, vol. 25, p. 065001 (17pp), March 2009.

[50] V. A. Morozov, *Methods for solving incorrectly posed problems*. New York: Springer, 1984.

[51] A. N. Tikhonov, "Regularization of incorrectly posed problems," *Soviet Math Dokl.*, vol. 4, pp. 1624–1627, 1963.

[52] A. N. Tikhonov, V. Y. Aresnin, and F. John, *Solutions of Ill-posed Problems*. New York: John Wiley and Sons, 1977.

[53] W. C. Chew and Y. M. Wang, "Reconstruction of two-dimensional permittivity distribution using the distorted born iterative method," *IEEE Transactions on Medical Imaging*, vol. 9, no. 2, pp. 218–225, 1990.

[54] N. Joachimowicz, C. Pichot, and J. P. Hugonin, "Inverse scattering: An iterative numerical method for electromagnetic imaging," *IEEE Transactions on Antennas and Propagation*, vol. 39, no. 12, pp. 1742–1752, Dec 1991.

[55] A. Franchois and C. Pichot, "Microwave imaging–complex permittivity reconstruction with a Levenberg-Marquardt method," *IEEE Transactions on Antennas and Propagation*, vol. 45, no. 2, pp. 203–215, Feb 1997.

[56] P. Mojabi and J. LoVetri, "Preliminary investigation of the NCP parameter choice method for inverse scattering problems using BIM: 2-D TM case," *Applied Computational Electromagnetics Society Journal*, vol. 23, no. 3, pp. 207–214, September 2008.

[57] ——, "Adapting the normalized cumulative periodogram parameter-choice method to the tikhonov regularization of 2-D TM electromagnetic inverse scattering using born iterative method," *Progress in Electromagnetic Research M*, pp. 111–138, 2008.

[58] P. M. van den Berg, A. L. van Broekhoven, and A. Abubakar, "Extended contrast source inversion," *Inverse Problems*, vol. 15, pp. 1325–1344, 1999.

[59] P. C. H. D. Calvetti and L. Reichel, "L-curve curvature bounds via Lanczos bi-diagonalization," *SIAM Journal of Scientific computing*, vol. 14, pp. 20–25, 2002.

[60] P. C. Hansen and D. P. O'Leary, "The use of the L-curve in the regularization of discrete ill-posed problems," *SIAM Journal of Scientific computing*, vol. 14, pp. 1487–1503, 1993.

[61] G. H. Golub, M. Heath, and G. Wahba, "Generalized cross validation as a method for choosing a good ridge parameter," *Technometrics*, vol. 21, pp. 215–224, 1979.

[62] M. Hanke, *Conjugate Gradient-Type Methods for Ill-posed Problems*. Longman, 1995.

[63] P. Mojabi and J. LoVetri, "Enhancement of the krylov subspace regularization for microwave biomedical imaging," *(in press) IEEE Transactions on Medical Imaging*, 2009.

[64] P. M. van den Berg and R. E. Kleinman, "A contrast source inversion method," *Inverse Problems*, vol. 13, pp. 1607–1620, 1997.

[65] P. van den Berg and A. Abubakar, "Contrast source inversion method: State of art," *Progress in Electromagnetics Research*, vol. 34, pp. 189–218, 2001.

[66] R. E. Kleinman and P. M. van den Berg, "A modified gradient method for two-dimensional problem in tomography," *Journal of Computed Applied Mathematics*, vol. 42, no. 1, pp. 17–35, 1992.

[67] M. Klemm, I. J. Craddock, J. A. Leendertz, A. Preece, and R. Benjamin, "Radar-based breast cancer detection using a hemispherical antenna array- Experimental results," *IEEE Transactions on Antennas and Propagation*, vol. 57, no. 6, pp. 1692–1704, June 2009.

[68] S. M. Salvador and G. Vecchi, "Experimental tests of microwave breast cancer detection on phantoms," *IEEE Transactions on Antennas and Propagation*, vol. 57, no. 6, pp. 1705–1712, June 2009.

[69] C. Gilmore and J. LoVetri, "On fourier imaging techniques for biomedical imaging," in *IEEE Antennas and Propagation Society International Symposium 2006*, July 2006, pp. 279–282.

[70] J. D. Zaeytijd, A. Franchois, C. Eyraud, and J. Geffrin, "Full-wave three-dimensional microwave imaging with a regularized Gauss-Newton method–theory and experiment," *IEEE Transactions on Antennas and Propagation*, vol. 55, no. 11, pp. 3279–3292, Nov 2007.

[71] S. Caorsi, A. Massa, and M. A. Pastorino, "A computational technique based on a real-coded genetic algorithm for microwave imaging purposes," *IEEE Transactions on Geoscience and Remote Sensing*, vol. 38, no. 4, pp. 1697–1708, 2000.

[72] A. Abubakar, T. M. Habashy, V. L. Druskin, L. Knizhnerman, and D. Alumbaugh, "2.5D forward and inverse modeling for interpreting low-frequency electromagnetic measurements," *Geophysics*, vol. 73, no. 4, pp. F165–F177, July–Aug 2008.

[73] A. Abubakar and P. M. van den Berg, "Iterative forward and inverse algorithms based on domain integral equations for three–dimensional electric and magnetic objects," *Journal of Computational Physics*, vol. 195, pp. 236–262, 2004.

[74] A. Abubakar, W. Hu, P. van den Berg, and T. Habashy, "A finite-difference contrast source inversion method," *Inverse Problems*, vol. 24, p. 065004 (17pp), 2008.

[75] E. Chong and S. Zak, *An Introduction to Optimization.* New York: Wiley Interscience, 2001.

[76] E. Polak and G. Ribiere, "Note sur la convergence de directions conjugees," *Revue Francaise Informant Recherch Operationelle*, 1969.

[77] A. Abubakar, P. M. van den Berg, T. M. Habashy, and H. Braunisch, "A multiplicative regularization approach for deblurring problems," *IEEE Transactions on Image Processing*, vol. 13, no. 11, pp. 1524–1532, Nov 2004.

[78] P. van den Berg, A. Abubakar, and J. Fokkema, "Multiplicative regularization for contrast profile inversion," *Radio Science*, vol. 38, pp. 23.1–23.10, 2003.

[79] L. P. Song, C. Yu, and Q. H. Liu, "Through-wall imaging (TWI) by radar: 2-D tomographic results and analyses," *IEEE Transactions on Geoscience and Remote Sensing*, vol. 43, no. 12, pp. 2793–2798, Dec 2005.

[80] K. van Dongen and W. D. Wright, "A full vectorial contrast source inversion scheme for 3d acoustic imaging of both compressibility and density profiles," *Journal of the Acoustical Society of America*, vol. 121, pp. 1538–49, 2007.

[81] L. Rudin, S. Osher, and C. Fatemi, "Nonlinear total variation based on noise removal algorithm," *Physica D*, vol. 30, pp. 259–68, 1992.

[82] J. Richmond, "Scattering by a dielectric cylinder of arbitrary cross section shape," *IEEE Transactions on Antennas and Propagation*, vol. 13, pp. 334–341, May 1965.

[83] P. Zwamborn and P. van den Berg, "The three dimensional weak form of the conjugate gradient fft method for solving scattering problems," *IEEE Transactions on Microwave Theory and Techniques*, vol. 40, no. 9, pp. 1757–1766, Sep 1992.

[84] P. van den Berg, "Iterative computational techniques in scattering based upon the integrated square error criterion," *IEEE Transactions on Antennas and Propagation*, vol. 32, no. 10, pp. 1063–1071, Oct 1984.

[85] K. Belkebir and M. Saillard, "Testing inversion algorithms against experimental data: inhomogeneous targets," *Inverse Problems*, vol. 21, pp. S1–S3, 2005.

[86] J. J. Mallorqui, N. Joachimowicz, J. C. Bolomey, , and A. P. Broquetas, "Database of 'in-vivo' measurements for quantitative microwave imaging and reconstruction algorithms available," *IEEE Antennas and Propagation Magazine*, vol. 37, no. 5, pp. 87–89, 1995.

[87] A. Broquetas, J. Romeu, J. M. Rius, A. R. ElliasFuste, A. Cardama, and L. Jofre, "Cylindrical geometry: a further step in active microwave tomography," *IEEE Transactions on Microwave Theory and Techniques*, vol. 39, pp. 836–844, May 1991.

[88] S. G. C. Gabriel and E. Corthout, "The dielectric properties of biological tissues: III. parametric models for the dielectric spectrum of tissues," *Physics in Medicine and Biology*, vol. 41, no. 11, pp. 2271–2294, 1996.

[89] A. Abubakar, P. M. van den Berg, and T. M. Habashy, "Application of the multiplicative regularized contrast source inversion method on TM- and TE-polarized experimental fresnel data," *Inverse Problems*, vol. 21, pp. S5–S13, 2005.

[90] Z. Peng and A. G. Tijhuis, "Transient scattering by a lossy dielectric cylinder: marching-on-in-frequency approach," *Journal of Electromagnetic Waves and Applications*, vol. 7, pp. 739–763, 1993.

[91] N. Joachimowicz, J. J. Mallorqui, J. C. Bolomey, and A. Broquetas, "Convergence and stability assessment of Newton–Kantorovich reconstruction algorithms for microwave tomography," *IEEE Transactions on Medical Imaging*, vol. 17, pp. 562–569, Aug 1998.

[92] S. C. Jun and U. J. Choi, "Convergence analyses of the born iterative method and the distorted born iterative method," *Numerical Functional Analysis and Optimization*, vol. 20, pp. 301–16, 1999.

[93] K. Paulsen and P. Meaney, "Nonactive antenna compensation for fixed-array microwave imaging. i. model development," *IEEE Transactions on Medical Imaging*, vol. 18, no. 6, pp. 496–507, June 1999.

[94] P. Meaney, K. Paulsen, J. Chang, M. Fanning, and A. Hartov, "Nonactive antenna compensation for fixed-array microwave imaging. ii. imaging results," *IEEE Transactions on Medical Imaging*, vol. 18, no. 6, pp. 508–518, June 1999.

[95] O. Franza, N. Joachimowicz, and J.-C. Bolomey, "Sics: a sensor interaction compensation scheme for microwave imaging," *IEEE Transactions on Antennas and Propagation*, vol. 50, no. 2, pp. 211–216, Feb 2002.

[96] T. Habashy and R. Mittra, "On some inverse problems in electromagnetics," *Journal of Electromagnetic Waves and Applications*, vol. 1, pp. 25–58, 1987.

[97] D. Colton, J. Coyle, and P. Monk, "Recent developments in inverse acoustic scattering theory," *SIAM Review*, pp. 369–414, 2000.

[98] F. L. L.P. Song, Q.H. Liu and Z. Zhang, "Reconstruction of three-dimensional objects in layered media: numerical experiments," *IEEE Transactions on Antennas and Propagation*, vol. 53, pp. 1556–61, 2005.

[99] P. Mojabi, C. Gilmore, A. Zakaria, and J. LoVetri, "Biomedical microwave inversion in conducting cylinders of arbitrary shapes," in *Antenna Technology and Applied Electromagnetics and the Canadian Radio Science Meeting, 2009. ANTEM/URSI 2009. 13th International Symposium on*, Feb. 2009, pp. 1–4.

[100] A. E. Bulyshev, A. E. Souvorov, S. Y. Semenov, R. H. Svenson, A. G. Nazarov, Y. E. Sizov, and G. P. Tastis, "Three dimensional microwave tomography. theory and computer experiments in scalar approximation," *Inverse Problems*, vol. 16, pp. 863–875, 2000.

[101] D. Winters, E. Bond, B. Van Veen, and S. Hagness, "Estimation of the frequency-dependent average dielectric properties of breast tissue using a time-domain inverse scattering technique," *IEEE Transactions on Antennas and Propagation*, vol. 54, no. 11, pp. 3517–3528, Nov. 2006.

[102] W. Hu, A. Abubakar, and T. Habashy, "Simultaneous frequency domain inversion method for full waveform seismic data," *Geophysics*, vol. 73, 2008.

[103] ——, "Application of the nearly perfectly matched layer in acoustic wave modeling," *Geophysics*, vol. 72, p. SM169, 2007.

[104] S. Semenov and D. Corfield, "Microwave tomography for brain imaging: Feasibility assessment for stroke detection," *International Journal of Antennas and Propagation*, p. 254830, 2008.

[105] Federal Communications Commision, "Dielectric properties of body tissues at rf and microwave frequencies," http://www.fcc.gov/fcc-bin/dielec.sh, accessed July 2008.

[106] E. Zastrow, S. Davis, M. Lazebnik, F. Kelcz, B. Van Veen, and S. Hagness, "Development of anatomically realistic numerical breast phantoms with accurate dielectric properties for modeling microwave interactions with the human breast," *IEEE Transactions on Biomedical Engineering*, vol. 55, no. 12, pp. 2792–2800, Dec. 2008.

[107] W. C. Chew and J. H. Lin, "A frequency–hopping approach for microwave imaging of large inhomogeneous bodies," *IEEE Microwave and Guided Wave Letters*, vol. 5, no. 12, pp. 439–441, Dec. 1995.

[108] C. Gilmore and J. LoVetri, "System and methods of improved tomography imaging," November 2007, U.S. Patent Application 61/003,891.

[109] G. Dahlquist, Åke Björck, and T. by. Ned Anderson, *Numerical Methods*. New Jersey, USA: Prentice-Hall, 1974.

[110] O. M. Bucci, L. Crocco, , and T. Isernia, "Improving the reconstruction capabilities in inverse scattering problems by exploitation of close-proximity setups," *Journal of the Optical Society of America A*, vol. 16, no. 7, pp. 1788–1798, 1999.

[111] T. J. Cui, W. C. Chew, X. X. Yin, and W. Hong, "Study of resolution and super resolution in electromagnetic imaging for half-space problems," *IEEE Transactions on Antennas and Propagation*, vol. 52, no. 6, pp. 1398–1411, June 2004.

[112] F. Chen and W. Chew, "Experimental verification of super resolution in nonlinear inverse scattering," *Applied Physics Letters*, vol. 72, no. 23, pp. 3080–3082, 1998.

[113] J.-M. Geffrin, "Imagerie microonde: etude d'un scanner a 434 mhz pour des applications biomedicales," Ph.D. dissertation, University of Paris XI, 1995.

[114] A. Franchois and A. G. Tijhuis, "A quasi-Newton reconstruction algorithm for a complex microwave imaging scanner environment," *Radio Science*, vol. 38, no. 2, 2003.

[115] P. M. van den Berg and J. T. Fokkema, "Removal of undesired wavefields related to the casing of a microwave scanner," *IEEE Transactions on Microwave Theory and Techniques*, vol. 51, pp. 187–92, 2003.

[116] R. Lencrerot, A. Litman, H. Tortel, and J. M. Geffrin, "Measurement strategies for a confined microwave circular scanner," *Inverse Problems in Science and Engineering*, p. 10.1080/17415970802577012, 2009.

[117] R. Collin, *Field Theory of Guided Waves*. IEEE Press, 1990, 2nd Edition.

[118] D. Trim, *Applied Partial Differential Equations*. PWS-Kent Publishing Company, 1990.

[119] D. Wilton, S. Rao, A. Glisson, D. Schaubert, O. Al-Bundak, and C. Butler, "Potential integrals for uniform and linear source distributions on polygonal and polyhedral domains," *IEEE Transactions on Antennas and Propagation*, vol. 32, pp. 276–281, 1984.

[120] C. Balanis, *Advanced Engineering Electromagnetics*. John Wiley and Sons, Inc., 1989.

[121] A. Abbosh, H. Kan, and M. Bialkowski, "Compact ultra-wideband planar tapered slot antenna for use in a microwave imaging system," *Microwave Optical Technology Letters*, vol. 48, pp. 2212–2216, 2006.

[122] M. Ostadrahimi, S. Noghanian, and L. Shafai, "A modified double layer tapered slot antenna with improved cross polarization," *13th International Symposium on Antenna Technology and Applied Electromagnetics (ANTEM), Banff, Alberta, Canada, February 15-18*, 2009.

[123] C. Yu, M. Yuan, J. Stang, E. Bresslour, R. George, G. Ybarra, W. Joines, and Q. H. Liu, "Active microwave imaging ii: 3-d system prototype and image reconstruction from experimental data," *IEEE Transactions on Microwave Theory and Techniques*, vol. 56, no. 4, pp. 991–1000, April 2008.

[124] A. Litman and L. Crocco, "Testing inversion algorithms against experimental data: 3d targets," *Inverse Problems*, vol. 25, 2009.

[125] D. Firsov, I. Jeffrey, V. Okhmatovski, C. Gilmore, J. LoVetri, and W. Chamma, "High-order fvtd on unstructured grids using an object-oriented computational engine," *Applied Computational Electromagentics Society Journal*, vol. 22, no. 1, pp. 71–80, 2007.

[126] D. Firsov and J. LoVetri, "Necessary stability criterion for unstructured mesh upwinding fvtd schemes for maxwell's equations," *ACES 2007, The 23rd Annual Review of Progress in Applied CEM, Verona, Italy*, 2007.

[127] J. LoVetri and D. Firsov, "The University of Manitoba finite-volume time-domain engine," Defence Research and Development Ottawa, Canada, Tech. Rep., 2007.

[128] A. Zakaria, C. Kaye, I. Jeffrey, and J. LoVetri, "Experimental validation of thin-wire FVTD models," in *Antenna Technology and Applied Electromagnetics and the Canadian Radio Science Meeting, 2009. ANTEM/URSI 2009. 13th International Symposium on*, Feb. 2009, pp. 1–4.

[129] I. Jeffrey, D. K. Firsov, C. Gilmore, V. Okhmatovski, and J. LoVetri, "Parallel high-order EM-FVTD on an unstructured mesh," *ACES 2007, The 23rd Annual Review of Progress in Applied CEM, Verona, Italy*, 2007.

[130] T. T. Wu and R. King, "The cylindrical antenna with nonreflecting resistive loading," *IEEE Transactions on Antennas and Propagation*, vol. 13, no. 3, pp. 369–373, May 1965, corrections, Vol. 13, no. 6, p. 998. Nov. 1965.

[131] A. Zakaria, *Using FEM to solve for the Transverse Magnetic (TM) Electric field inside a cylindrical PEC bounded region.*

[132] M. Born, *Z. Phys.*, vol. 38, p. 803, 1926.

[133] A. C. Kak and M. Slaney, *Principles of Computerized Tomographic Imaging.* IEEE Press, 1988.

[134] A. J. Devaney, "Nonuniqueness in the inverse scattering problem," *Journal of Mathematical Physics*, vol. 19, no. 7, pp. 1526–1531, 1978.

[135] C. Gilmore, "A comparison of imaging methods using ground penetrating radar for landmine detection and a preliminary investigation into the singularity expansion method for identification of buried objects," Master's thesis, University of Manitoba, Winnipeg, Canada, 2005.

[136] C. Gilmore, I. Jeffrey, and J. LoVetri, "Derivation and comparison of SAR and frequency-wavenumber migration within a common inverse scalar wave problem formulation," *IEEE Transactions on Geoscience and Remote Sensing*, vol. 55, no. 6, pp. 1454–1461, June 2006.

[137] L. Kantorovich and G. Akilov, *Functional Analysis*. New York, USA: Pergamon Press, 1982, translated by H.L. Silcock.